UC Berkeley
UC Berkeley Electronic Theses and Dissertations

Title

Epitaxial Stabilization of a Morphotropic Phase Boundary in Lead-Free Ferroelectric Thin Films

Permalink

https://escholarship.org/uc/item/0pz9s4r8

Author

Zeches, Robert James

Publication Date

2011

Peer reviewed|Thesis/dissertation

eScholarship.org Powered by the California Digital Library
University of California

Epitaxial Stabilization of a Morphotropic Phase Boundary in Lead-Free Ferroelectric Thin Films

by

Robert James Zeches

A dissertation submitted in partial satisfaction of the requirements for the degree of

Doctor of Philosophy

in

Engineering – Materials Science and Engineering

and the Designated Emphasis

in

Nanoscale Science and Engineering

in the

Graduate Division

of the

University of California, Berkeley

Committee in charge:

Professor Ramamoorthy Ramesh, Chair
Professor Junqiao Wu
Professor Sayeef Salahuddin

Fall 2011

Epitaxial Stabilization of a Morphotropic Phase Boundary
in Lead-Free Ferroelectric Thin Films

© 2011

by Robert James Zeches

Abstract

Epitaxial Stabilization of a Morphotropic Phase Boundary
in Lead-Free Ferroelectric Thin Films

by

Robert James Zeches

Doctor of Philosophy in Engineering – Materials Science and Engineering
and the Designated Emphasis in Nanoscale Science and Engineering

University of California, Berkeley

Professor Ramamoorthy Ramesh, Chair

This dissertation details the synthesis and characterization of compressively strained epitaxially grown bismuth ferrite thin films in an effort to improve their piezoelectric properties with the goal of finding a viable lead-free alternative to lead zirconate titanate. It is found that under compressive epitaxial strain a morphotropic phase boundary, the hallmark of high performance piezoelectrics, is stabilized in this material. The structural characterization of these films reveals complex mixed-phase morphologies whereby nearly energetically degenerate monoclinically distorted tetragonal and rhombohedral ferroelectric phases coexist with apparent crystallographically coherent interfaces. This mixed phase morphology is found to be responsive to perturbations both via mechanical indentation and an applied electric field, whereby a reversible phase transition is observed in the films. Electrical characterization of these films indicates a pronounced increase in their piezoelectric and ferroelectric properties.

Dedication

This work is dedicated to my wife Charley, who has supported me without conditions through my intellectual and academic pursuits; and to my daughters Lola, Genevieve and Devon, for whom I intend to work for the rest of my life utilizing all of my knowledge, experience, expertise and abilities to make the world a better place for them and their entire generation.

"The scientist does not study nature because it is useful; he studies it because he delights in it, and he delights in it because it is beautiful. If nature were not beautiful, it would not be worth knowing, and if nature were not worth knowing, life would not be worth living."

Jules Henri Poincaré (1854-1912)

Acknowledgements

I would like to acknowledge the assistance of the following people who collaborated with me on this work and without whom this dissertation would not be possible. First, I would like to thank Ramesh for taking on such an unconventional graduate student, bringing me into his research group, and giving me the opportunity to work in a world class lab at one of the greatest universities in the world. I would also like to thank Steven Crane and Lane Martin for going out of their way to welcome me into the research group, and Lane in particular for giving me guidance on conducting careful and thoughtful research. I would in particular like to thank Jinxing Zhang for not only showing me the finer points of scanning probe microscopy, but also for being a valuable collaborator in this research effort. His encouragement and enthusiasm provided valuable support in my development of the ideas and methodology contained in this dissertation. I would also like to thank Jan Seidel for his help with the scanning probe work and for some valuable and enlightening discussions. I would like to thank Marta Dacil Rossell and Bin Xiang for all the beautiful transmission electron microscopy images and Amit Kumar for all the SHG work. I would like to thank Alison Hatt and Guang Shen for the theoretical development using DFT and phase field modeling, respectively. Finally, I would like to thank all the members of my qualifying exam committee – Oscar Dubon, Ronald Gronsky, Junqiao Wu and Sayeef Salahuddin for their guidance in focusing this work.

Table of Contents

1 Introduction **1**
1.1 Complex Oxides **1**
1.2 Piezoelectric Materials **1**
1.3 The Problem with PZT **2**
1.4 Thin Films and Strain Engineering **2**
1.5 Goals of This Research **3**
1.6 Organization of Subsequent Sections **3**

2 Background **5**
2.1 Piezoelectricity **5**
2.2 Ferroelectricity **8**
2.2.1 The Curie Temperature 9
2.2.2 Domains and Hysteresis 10
2.3 Morphotropic Phase Boundaries **11**
2.3.1 Origins of Enhanced Properties 12
2.3.2 Tuning the Phase Boundary 14
2.4 An Alternative to PZT **15**
2.4.1 The Role of Lead 15
2.4.2 Bismuth on the A-Site 16
2.5 Bismuth Ferrite **16**
2.5.1 A-Site Driven Ferroelectricity 17
2.5.2 Evidence for a Tetragonal Phase 18
2.6 General Experimental Approach **18**

3 Growth of BFO Thin Films **19**
3.1 Thin Films and Epitaxy **19**
3.2 Substrate Selection **20**
3.3 Pulsed Laser Deposition **21**

4 Structural Characterization **24**
4.1 Structural Characterization Techniques **24**
4.1.1 X-Ray Diffraction 24
4.1.2 Atomic Force Microscopy 26
4.1.3 Transmission Electron Microscopy 27
4.1.4 Optical Second Harmonic Generation 28
4.2 Evidence for a Phase Transition **29**
4.2.1 XRD $\theta - 2\theta$ Scans 29
4.2.2 Reciprocal Space Mapping 32
4.3 Mixed Phase Films **34**
4.3.1 Surface Topography of Mixed Phase Films 34
4.3.2 X-Ray Diffraction Results on a Film Thickness Series 36
4.3.3 SHG Results from a Film Thickness Series 38
4.3.4 TEM Results From Mixed Phase Films 39
4.3.5 Nanomechanical Perturbation 45
4.3.6 Confirmation via Theoretical Models 47

5 Electrical Characterization **51**

5.1 Bottom Electrode Deposition **51**
5.2 Electrical Characterization Techniques **52**
5.2.1 Piezoresponse Force Microscopy 52
5.2.2 Ferroelectric Hysteresis Measurements 54
5.3 Electric Field Induced Phase Changes **55**
5.3.1 Ferroelectric Poling and Phase Evolution 55
5.3.2 Local Phase Response to Applied Nanoprobe Bias 58
5.4 Evidence for Enhanced Electrical Properties **59**
5.4.1 Top Electrode Deposition 59
5.4.2 Ferroelectric Polarization Measurements 61
5.4.3 Piezoelectric Hysteresis Measurements 62

6 Summary of Findings **66**

7 Recommendations for Future Work **70**
7.1 Growth on Silicon Based Heterostructures **70**
7.2 Tensile Strain and the Orthorhombic Phase **70**
7.3 The Coherent Phase Boundary **71**
7.4 Closing remarks **72**

References **73**

List of Figures

Figure 1. Schematic of a perovskite unit cell with the ABO_3 stoichiometry, where A and B are metal cations and O is an oxygen anion. The structure can generally be characterized as a BO_6 octahedron surrounded by octahedrally coordinated A cations, resulting in the stoichiometry ABO_3. 7
Figure 2. Schematic illustration of the converse piezoelectric effect in a perovskite material with a spontaneous polarization. The top row represents a 2-dimensional projection of the perovskite structure ABO_3 in response to an applied electric field. The bottom row shows the relative magnitude of the polarization, P, in response to an applied electric field. **(A)** is under no applied external field, **(B)** has an elongated structure and increased polarization under an applied electric field of the same polarity as P, and **(C)** has a compressed structure and decreased polarization under an applied electric field of opposite polarity as P. 8
Figure 3. A simple schematic showing the typical variation of the dielectric permittivity (ϵ) as a function of temperature for a normal ferroelectric near the Curie temperature. The permittivity is marked by a sharp increase near the ferroelectric-paraelectric phase transition. 9
Figure 4. Due to the presence of ferroelectric and ferroelastic domains, ferroelectric materials are characterized by a polarization-electric field (P vs. E) hysteresis loop **(A)** and a strain-electric field (ε vs. E) hysteresis loop **(B)**. A schematic of the polarization and strain effects happening on a domain level in the material shows the origin of the hysteresis **(C)**. 10
Figure 5. A simple phase diagram for PZT. The high temperature centrosymmetric cubic phase is at the top of the diagram above the compositionally dependent Curie temperature. Below the cubic phase, ferroelectric rhombohedral and tetragonal phases are found, depending on the composition. In the middle of the diagram, the morphotropic phase boundary between the rhombohedral and tetragonal phases can be seen. It is near this phase boundary that PZT has anomalously enhanced piezoelectric properties. 12
Figure 6. The structure of $BiFeO_3$ can be visualized as a distorted cubic perovskite with pseudo-cubic lattice parameters a_{pc} = 3.96 Å and α_{pc} = 89.5°. Here it is shown as two distorted perovskite cells connected along the pseudocubic <111> body diagonal, resulting in a rhombohedral unit cell. The two oxygen octahedra in this structure are alternately rotated about $<111>_{pc}$ direction by ~13.8(3)°, and the Fe cations are shifted by 0.135 Å along the same axis away from the center of the oxygen octahedra. 17
Figure 7. Schematic illustration of epitaxial thin film growth when **(A)** the substrate and film are almost perfectly lattice matched, **(B)** the interface is strained but defect-free, and **(C)** the interface is relaxed due to the formation of misfit dislocations at the interface 19
Figure 8. Schematic of a pulsed laser deposition (PLD) system showing the KrF excimer laser on the upper left, beam control optics on the upper right, and vacuum chamber on the bottom. The laser beam is shown as incident on the rotating ceramic target

within the vacuum chamber along with the resultant plume of plasma. The interaction results in the stoichiometric deposition of target material on the substrate adhered to a resistive heater. 22

Figure 9. Schematic of an atomic force microscope. The cantilever with the atomically sharp Si tip is kept at a static height above the sample surface and oscillated at its resonant frequency. Electrostatic interactions between the tip and the sample cause the cantilever to bend, which changes the location of the laser spot reflected on to a four-quadrant photodetector. The acquired signal can be converted into a topological map of the sample surface 26

Figure 10. Schematic showing the experimental setup for optical second harmonic generation (SHG). Polarized light with frequency ω is produced by a tunable pulsed laser and its polarization direction is continuously rotated through an angle ϕ via a half-wave plate. This beam is then incident on the surface of the film at an adjustable angle θ with respect to the surface normal. The intensity of the frequency doubled output signal from the film is detected within the *sp* plane as a function of the angle of incidence θ and the polarization angle ϕ of the incident light, and compared to the expected intensity expressions for the film based on an assumed symmetry. 28

Figure 11. X-ray diffration spectra from (001) oriented BFO films grown on DSO(110), STO(001), LSAT(001), LAO(001) and YAO(110). These spectra show the 002 and 220 peaks of the various substrates and the 002 peaks of the BFO films grown on them. All direction given are pseudocubic except those given for DSO and YAO, which are are orthorhombic (110) which is equivalent to pseudocubic (001). 30

Figure 12. Evolution of the structural parameters of BFO films grown on various substrates inducing increasing compressive strain, including the film *c*-axis lattice parameter **(A)**, the film *c/a* ratio assuming an unrelaxed film **(B)**, and the film unit cell volume **(C)**. There appears to be discontinuity in the change in unit cell volume between the films grown on LSAT and the films grown on LAO, suggestive of a phase transition somewhere between these two strains. 31

Figure 13. Complete XRD theta scan of a 25nm thick BFO film grown on a (001) oriented LAO substrate. The 001, 002 and 003 peaks of the BFO film are labeled. The corresponding substrate peaks are marked with *. There are no other peaks in the spectra, indicating a single phase film with no secondary phases. The inset shows 360° ϕ scans of the 011 and 111 peaks for the film and substrate, demonstrating the epitaxial relationship between the film and substrate. 32

Figure 14. **(A)** Composite reciprocal space map showing the 013 family of peaks for the LAO substrate and for the 25 nm thick BFO film grown on it. The separation of the substrate 103 and 013 peaks is due to the *a* and *b* lattice parameters having slightly different values. The BFO film shows a similar separation of the 103 and 013 peaks, as well as a separation of the -103 and 103 peaks, suggesting a monoclinically distorted unit cell with an angle $\beta < 90°$ between the c and a lattice vectors. **(B)** Schematic of the proposed unit cell structure for this film based on the reciprocal space map shown in **(A)**... 33

Figure 15. **(A)** a 9 nm thick BFO film on LAO, showing a smooth topography with unit cell step heights. **(B)** a 120 nm this BFO film on LAO, showing a dark (lower height) stripe-like morphology in a lighter colored (higher) field. 35
Figure 16. **(A)** Close-up AFM scan of one of the striped domains from a ~80 nm thick BFO film grown on LAO with a horizontal line indicating where the line profile in **(B)** was measured. The relative height differences between the dark and light areas can be seen to have a peak-to-valley height difference of 1-2 nm. The spacing of the stripes is measured to be approximately 40-50 nm. 35
Figure 17. AFM scans of a thickness series of BFO films grown on (001) oriented LAO substrates. The films get progressively thicker from **(A)** through **(F)**, with the thicknesses indicated. The stripe-like morphology evolves with increasing thickness, indicating that the stripes are energetically more favorable in the reduced strain state of the thicker films, consistent with the hypothesis that the darker (lower) stripes are a separate emergent phase from the lighter (higher) matrix phase. 36
Figure 18. XRD θ-2θ scans of a thickness series of BFO films grown on LAO substrates, showing the 002 peaks of the T-phases and R-phases in the films and the 002 peaks of the substrate. The film thicknesses are, from bottom to top, 9 nm, 33 nm, 40 nm, 83 nm, 120 nm and 160 nm. The Kiesseg fringes can be clearly seen surrounding the film peak in the three thinnest films. The variation in quality of the substrates with respect to twinning in LAO can be seen in the substrate peaks, and are also reflected in the asymmetry of the film peaks. 37
Figure 19. SHG signal obtained in tilted (top plots, $\theta = 45°$) and normal (bottom plots, $\theta = 0°$) incidence configurations for three thicknesses of BFO/LAO films (17 nm, 33 nm and 160 nm), with the output analyzer along *S* (green) and *P* (red) polarizations, and along 45° (red) and -45° (green) relative to the pseudocubic axes, respectively. The 17 nm films are dominated by SHG signal from the T-phase ($\theta = 45°$) while in thicker films the SHG signal from the R-phase ($\theta = 0°$) increases with thickness, consistent with AFM and XRD results. Solid black lines are theory fits for T-phase and R-phase, accounting for different domain variants in the R-phase. 38
Figure 20. Bright field TEM image of a cross-sectional of area of mixed a phase region in a ~80 nm thick BFO film grown on LAO. The T-phase appears bright in this image and the R-phase appears dark. Note the wedge shapes of the two phases within the cross-section of the film, consistent with the decreasing compressive strain up through the volume of the film, favoring the T-phase near the substrate and the R-phase near the film surface 40
Figure 21. Selected area diffraction patterns taken from the striped domain shown in the bright field image of **Figure 20**. Each shows a superposition of patterns from the substrate and film, with the unit cells from each outlined and labeled. The zone axis for each is 100, and the 001 and 010 diffraction spots are indexed. **(A)** is taken from the lighter colored region of **Figure 20** corresponding to the T-phase. Measurements from this pattern give an out-of-plane lattice parameter of ~4.65 Å, an in-plane lattice parameter of ~3.7 Å, and an angle of ~89° between the two axes. **(B)** is taken from the darker colored region of **Figure 20** corresponding to the R-phase. Measurements from this pattern give an out of plane lattice parameter of

~4.07Å, an in-plane lattice parameter of ~3.8 Å, and an angle of ~89.5° between the two axes. 40
Figure 22. Close up HAADF-STEM images of T-phase region flanked by two R-phase regions. The columns of the much heavier Bi atoms show up as brightly colored spots, while the lighter columns of Fe atoms show up as the smaller, darker spots. The interfaces between the phases appear to be coherent with smooth, defect-free transitions and no apparent stacking faults or dislocations present along the boundaries. The transition and its associated abrupt change in unit call volume appear to be accommodated purely by strain effects. 42
Figure 23. The estimations of in-plane and out-of-plane lattice parameter evolution along a linear row of unit cells through an interface between R-phase and T-phase domains. A close-up Z-contrast image of a phase boundary between a section of R-phase and T-phase is shown in **(A)** along with a line superimposed indicating where the measurements in **(B)** were taken. The *c/a* ratio appears to go from 1.07 to 1.27 in approximately ten unit cells with the *c*-axis parameter dramatically changing over this distance... 43
Figure 24. Atomic resolution Z-contrast images of the R-phase **(A)** and T-phase **(B)**. Insets are simplified unit cell projections with measured lattice parameters from the z-contrast images (top), and averaged structure images derived from an area containing 150 unit cells (bottom). The periodic spots of heavy Bi columns are brighter than the lighter FeO columns. The much lighter O columns are difficult to image directly in this orientation compared to the background intensity of the heavier atoms, however some O columns are evident in the T-phase average image, just below the top row of Bi atomic columns, suggesting a 5-fold coordination for the Fe cations. 44
Figure 25. A schematic of the *in situ* nanoindenter in contact with a mixed phase BFO film, with an electron transparent window between two trenches milled via focused ion beam. In this geometry, the beam passes through a mixed phase area of film that is subject to an applied stress normal to the film surface. 45
Figure 26 Bright-field TEM images (top) and corresponding selected area diffraction patterns (bottom) before **(A)**, during **(B)** and after **(C)** application of a mechanical force by a nanoindenter. In **(A)** the striped morphology of the mixed phase film is evident in the bright field image, and the corresponding SAD pattern shows 002 diffraction spots for both the R-phase and the T-phase. In **(B)** a ~30 mN mechanical force is applied by the nanoindenter, resulting in the striped morphology changing from a mixed phase to a single phase beneath the nanoindenter tip. The corresponding SAD pattern shows only the 002 diffraction spot for the R-phase. In **(C)** the nanoindenter has been retracted and the bright field image again shows a striped morphology indicating a mixed phase beneath the tip and the SAD pattern again shows 002 diffraction spots corresponding to both T-phase and R-phase...... 46
Figure 27. Density functional theory calculation results showing free energy *E* (top) and *c/a* ratio (bottom) for BFO under compressive epitaxial strain. The results suggest a volumetric increase associated with an isosymmetric phase transition between two phases with *Cc* symmetry. Predicted unit cell models are shown as inserts........... 48
Figure 28. Phase-field modeling and thermodynamic calculations for strained BFO. The thermodynamic analysis is indicated by solid lines and the phase-field analysis is

indicated by scattered symbols. The mixed-phase region consists of tetragonal, distorted rhombohedral and monoclinic phases. The results suggest that the tetragonal to rhombohedral phase boundary is near the strain value imposed by LAO at ~4.3% compressive strain at room temperature. This is consistent with DFT analysis and the experimental results........ 49

Figure 29. A schematic of the BFO/LSCO/LAO layered structure used in this study for electrical characterization of BFO films. The LSCO bottom electrode is < ~15 nm thick and completely strained, preserving the epitaxial constraint imposed on the BFO film by the underlying substrate........ 51

Figure 30. A schematic illustration of piezoforce domain imaging with PFM. In **(A),** when the applied E-field is parallel to the spontaneous polarization of the sample, the alternating potential of the field and the piezoelectric signal are in phase. As a result, the sample expands vertically and the cantilever is pushed up. In **(B),** when the applied E-field is antiparallel to the spontaneous polarization of the sample, the alternating potential of the field and the piezoresponse signal are out of phase by 180°. As a result, the sample contracts vertically and the cantilever is lowered. In **(C)** and **(D),** the in-plane spontaneous polarization direction of the sample can be determined by the shear piezoelectric coefficient (d_{15}). The applied E-field causes a shear deformation of the sample, which causes a torsional movement of the cantilever via friction........ 53

Figure 31. Schematic of how a standard PUND (positive up negative down) measurement is made. Measurements are made at the positive switched pulse (P^*) and the positive unswitched pulse ($P^\wedge$), and similar measurements are made at the negative switched and unswitched pulses. $P^\wedge$ represents the volatile component of the polarization, such as leakage effects and parasitic capacitance........ 55

Figure 32. Piezoforce microscopy images of a ~60 nm thick mixed phase BFO film grown on a ~10 nm LSCO bottom electrode layer. For these scans a -4 V DC bias is applied with a 2 V_{pp} AC component. **(A)** Topographical scan of the film with a height range of 5 nm, showing the mixed phase morphology. The lighter (higher) regions are the T-phase and the darker (lower) regions are the R-phase. **(B)** Out-of-plane piezoresponse showing contrast consistent with the mixed phase topography. The as grown polarization is down towards the substrate, thus with the applied E-field pointing up out of the film the T-phase contrast is darker than the R-phase. **(C)** In-plane piezoresponse consistent with the mixed-phase morphology of monoclinically distorted T-phase an R-phase........ 56

Figure 33. In **(A)** through **(F)**, the top images are the topographical scans, the middle images are the out-of-plane piezoresponse scans, and the bottom images are simplified schematics of the phase morphology and polarization orientations of the poled area in the center of the visible area of the film. Blue polarization arrows indicate the T-phase and red polarization arrows indicate the R-phase. The images in **(A)** show the as-grown film in its ground state, with T-phase and R-phase domains coexisting and a spontaneous polarization down into the film towards the substrate. As a scanned poling field is applied to a square area of the film, varying in value and alternating in polarity in **(B)** through **(F)**, the phase morphology changes from mixed-phase to nearly all T-phase and back again in a repeatable manner........ 57

Figure 34. Bright field TEM images (top) and selected area diffraction (SAD) patterns (bottom) of an area in a mixed phase film. The figures in **(A)** show the film prior to applying the bias, where the striped morphology of the mixed phase is evident in the bright field image and 011 diffraction spots corresponding to both phases appear in the SAD pattern. In **(B)** a +20 V bias is applied to the nanoprobe, resulting in the striped morphology changing from a mixed phase to a single phase beneath the nanoprobe tip. The SAD pattern now shows only the 011 diffraction spot corresponding to the T-phase. In **(C)** the bias has been removed and the bright field image again shows a striped morphology indicating a mixed phase. The corresponding SAD pattern in **(C)** again shows the 011 diffraction spots corresponding to both the T-phase and the R-phase. 59
Figure 35. Schematic of the process used to create Pt/LSCO microcapacitors on BFO films for electrical characterization. **(A)** A BFO film is grown *in situ* on a bottom electrode layer of LSCO. **(B)** Another layer of LSCO is grown *in situ* on top of the BFO film. **(C)** Photoresist is spin coated on to the surface and cured. **(D)** A patterned chrome mask is placed on the surface and the sample is exposed to UV light. **(E)** The exposed regions are removed when the sample is immersed in developer solution. **(F)** A thin layer of platinum is sputter coated on to the surface. **(G)** An acetone immersion lifts off the remaining photoresist and the platinum on top of it, leaving only the circular platinum contacts. **(H)** A hydrofluoric acid immersion preferentially etches the exposed LSCO that is not protected by the platinum contacts. **(I)** What remains is a stack consisting of the LAO substrate, a bottom electrode layer of LSCO, the BFO film and a series of ~24μm diameter Pt/LSCO top electrodes 60
Figure 36. Quasistatic (slow) ferroelectric measurements of mixed phase and predominantly R-phase BFO films on LAO. Mixed phase films show a polarization of ~125 $\mu C/cm^2$. This is higher than that measured for the mostly R-phase films, which show a polarization of ~60 $\mu C/cm^2$, consistent with measurements on rhombohedral BFO films. 61
Figure 37. Pulsed polarization measurements (PUND) with a pulse width of 5 μs. The mixed phase sample shows a switched polarization of ~220 $\mu C/cm^2$, which is consistent with the quasistatic measurements. In contrast, the R-phase sample above shows a switched polarization of ~110 $\mu C/cm^2$, also consistent with the quasistatic measurements as well as previous reports on rhombohedral BFO films. Note that in the measurements above the R-phase film was only characterized in one polarization direction. 62
Figure 38. Representative plots of d^*_{33} vs. applied bias for predominantly T-phase, mixed phase, and predominantly R-phase BFO films (blue, black and red lines, respectively) grown on a LSCO bottom electrode with 24 μm diameter Pt/LSCO top electrode contacts. The BFO film thicknesses are approximately 15 nm, 80 nm and 250 nm respectively. The thin predominantly T-phase film shows the lowest out-of-plane piezoresponse of ~30-35 pm/V, while the mixed-phase film shows the highest at ~115-120 pm/V. The predominantly R-phase sample has a measured piezoresponse of ~50-60 pm/V, which is consistent with widely reported results on rhombohedral BFO films. The apparent asymmetry for positive and negative

applied potential is primarily a consequence of the asymmetric mechanical boundary conditions that the piezoelectric layer is experiencing, namely the LAO substrate on one side and a free surface on the other. 63

Figure 39. Local piezoresponse measurements of mixed phase BFO compared to a known reference sample of PZT. These measurements were taken using a conductive AFM tip at the top electrode. The black curve represents the data from a mixed phase BFO/LSCO/LAO film and the blue curve represents data from a reference sample of PZT with a measured $d33*$ value of 65 pm/V. The results suggest the local $d33*$ value for mixed phase BFO is ~520 pm/V. 64

List of Tables

Table 1. List of substrates used in this study, their in-plane lattice parameters and their lattice mismatch with the theoretical epitaxially strained tetragonal BFO and the known bulk phase rhombohedral BFO. The in-plane lattice parameters listed are pseudocubic in the case of orthorhombic or rhombohedral substrates. The stoichiometry of LSAT is $(LaAlO_3)_{0.3}(Sr_2AlTaO_6)_{0.7}$. 21

Table 2. Structural data extracted from XRD data on BFO films grown on various substrates. The *c*-axis lattice parameters were measured directly and the *c*/*a* ratios and unit cell volumes were based on fully epitaxial films adopting the substrate in-plane lattice parameter. 30

Guide to Symbols and Abbreviations

°	degree (angle)
°C	degree Celsius (temperature)
$	U.S. dollar
Å	angstrom
a	lattice parameter
a_f	film in-plane lattice parameter
a_s	substrate in-plane lattice parameter
AC	alternating current
AFM	atomic force microscopy
BFO	bismuth ferrite, $BiFeO_3$
c	out-of-plane lattice parameter
C	capacitance
CBED	convergent beam electron diffraction
cm	centimeter
CVD	chemical vapor deposition
D	dielectric displacement (surface charge density)
d	distance between lattice planes
d	nonlinear optical coefficient
d	piezoelectric charge coefficient
d_{15}	shear piezoelectric charge coefficient in Voigt notation
d_{31}	transverse piezoelectric charge coefficient in Voigt notation
d_{33}	longitudinal piezoelectric charge coefficient in Voigt notation
d^*_{33}	out-of-plane piezoelectric charge coefficient
DC	direct current
DFT	density functional theory
DSO	dysprosium scandate
E	electric field
E_c	coercive field
EDS	energy dispersive spectroscopy
EELS	electron energy loss spectroscopy
eV	electron-volt
f	lattice mismatch
FIB	focused ion beam
fs	femtosecond
GPa	gigapascal (pressure)
HAADF	high-angle annular dark-field (Z-contrast)
HF	hydrofluoric acid
Hz	hertz
I	peak intensity in x-ray diffraction
IP	in-plane
J	joule
K	Fresnel coefficient function

K Kelvin (temperature)
keV kiloelectron-volt
kHz kilohertz
KNN $K_{0.5}Na_{0.5}NbO_3$
kV kilovolt
$K\alpha$ x-ray from copper K-alpha transition
l Miller index (*hkl*) for the *z*-direction
LAO lanthanum aluminate, $LaAlO_3$
LDA local density approximation
LDA+U local density approximation with Hubbard parameter
LSAT $(LaAlO_3)_{0.3}(Sr_2AlTaO_6)_{0.7}$
LSCO $La_{0.5}Sr_{0.5}CoO_3$
MBE molecular beam epitaxy
MEMS micro electro mechanical system
min minute
mm millimeter
mN millinewton
MPB morphotropic phase boundary
mTorr millitorr (pressure)
N number of diffraction peak fringes
NBT $Na_{0.5}Bi_{0.5}Ti0_3$
nm nanometer
ns nanosecond
OOP out-of-plane
P polarization
P^* remanent plus non-remanent polarization
$P^\wedge$ non-remanent polarization
$P^{2\omega}$ nonlinear polarization
pc pseudocubic
PFM piezoresponse force microscopy
PLD pulsed laser deposition
pm picometer
PMN $PbMg_{1/3}Nb_{2/3}O_3$
PMN-PT $(PbMg_{1/3}Nb_{2/3}O_3)_{1-x}(PbTiO_3)_x$
P_r remanent polarization
P_s spontaneous polarization
PUND positive up negative down
PZN $PbZn_{1/3}Nb_{2/3}O_3$
PZN-PT $(PbZn_{1/3}Nb_{2/3}O_3)_{1-x}(PbTiO_3)_x$
PZT lead zirconate titanate, $PbZr_{(1-x)}Ti_xO_3$
Q accumulated charge
Q electrostriction coefficient
Q_x, Q_y, Q_z reciprocal lattice directions
q_z Kiessig fringe factor
r radius of curvature for a PFM tip

R_A	A-site cation radius in the perovskite structure
R_B	B-site cation radius in the perovskite structure
R_O	oxygen anion radius in the perovskite structure
rh	rhombohedral
RoHS	Restriction of Hazardous Substances directive
RSM	reciprocal space map
S	elastic stiffness
SAD	selected area diffraction
SHG	second harmonic generation
STEM	scanning tunneling electron microscopy
STO	strontium titanate
t	film thickness
t	perovskite tolerance factor
t	time
T	temperature
T_c	superconducting transition temperature
T_c	Curie temperature
TDGL	time dependent Ginzburg-Landau equation
TEM	transmission electron microscopy
UV	ultraviolet light
V	applied bias
V	volt
V_{pp}	peak-to-peak voltage
WEEE	Waste Electrical and Electronic Equipment directive
XRD	x-ray diffraction
YAO	yttrium aluminate, $YAlO_3$
Z	atomic number
ZA	zone axis
α	unit cell lattice angle
β	angle of monoclinic distortion
δ_{ij}	Kronecker delta function
ΔP	change in polarization under an applied electric field
Δx	lateral displacement of a cantilever tip
Δz	vertical displacement of a cantilever tip
ϵ	dielectric permittivity
ϵ_0	dielectric permittivity of free space
ε	strain
ε_r	remanent strain
θ-2θ	theta axis angle in x-ray diffraction
λ	wavelength (light)
μC	microcoulomb
μm	micron
σ	stress
ϕ	phi axis angle in x-ray diffraction

φ	piezoresponse signal phase component
χ	dielectric susceptibility
$\chi_{\parallel}$	dielectric susceptibility parallel to the spontaneous polarization
$\chi_{\perp}$	dielectric susceptibility perpendicular to the spontaneous polarization
ω	frequency (light)
ω	omega (rocking curve) axis angle in x-ray diffraction

1 Introduction

1.1 Complex Oxides

The complex oxides are an interesting class of materials that tend to exhibit enhanced properties when energetically similar ground states are induced in the same material. This is usually done through chemical doping but, as will be demonstrated in this dissertation, it is not the only means to induce such a degeneracy. When these materials have competing energetically degenerate ground states they tend to exhibit a strong response to external perturbations such as a change in temperature, an applied external electromagnetic field, a change in pressure or an applied epitaxial strain. The competing ground states can be crystallographic in nature, and the response to perturbations can include structural phase transitions. Among the complex oxides, the perovskite family of materials exhibit a variety of different properties depending on their atomic constituents and their structural details due to the large degree of freedom there is within the perovskite structure for oxygen octahedral tilts and rotations as well as the relative movement of the cations in the lattice with respect to each other. Piezoelectric perovskite oxides are notable in that they show an anomalous increase in their material properties near a compositionally induced crystallographic phase boundary.

1.2 Piezoelectric Materials

Piezoelectric materials, which essentially convert electrical signals to mechanical signals, or vice-versa, are widely used in many areas of engineering and their use is increasing. The size of the piezoelectric market was over $10.5 billion in 2008 and is projected to nearly double to over $19.5 billion by 2012.[1] Transducer based piezoelectric materials are used for sonar, medical ultrasound imaging and fluid flow sensors. Piezoelectric devices that transform mechanical signals into electrical signals are widely used as accelerometers, such as those in seat-belt tension systems, or for pressure or vibration sensors. Piezoelectric actuators transform electrical signals into mechanical signals and are widely used in force generators such as automobile fuel injection valves or inkjet printer heads. Thin film piezoelectrics are finding useful application in the development of a diverse array micro-electromechanical system devices (MEMS), including microsensors and microactuators, nanopositioners, tiny ultrasonic motors and vibrational energy harvesting cantilevers. Thin film piezoelectrics offer an attractive means of sensing and actuation in small devices. Relative to other means of generating motion at the microscale, piezoelectricity scales well in terms of energy density as dimensions are reduced. They require comparatively low power and driving voltage to operate, they have very little inertia due to the small amount of material being used, which allows for use in high frequency devices, and they have a relatively high speed of polarization switching.

High performing piezoelectric films are generally solid solutions of perovskite oxide ferroelectrics with a rich phase diagram that includes a high-temperature cubic phase and

more than one ferroelectric phase depending on the temperature and the solid solution stoichiometry. As will be detailed in later sections, anomalously high piezoelectric responses generally occur in these materials when the composition is near one of these phase boundaries, commonly between ferroelectric rhombohedral phases and either a ferroelectric tetragonal phase or ferroelectric orthorhombic phase. These phase boundaries are called morphotropic phase boundaries, and are a central focus in the effort to find new and better performing piezoelectric thin films.

1.3 The Problem with PZT

The best and most commonly used piezoelectric materials are primarily based on solid solutions containing $PbTiO_3$. By far the most widely used are solid solutions of $PbZrO_3$ and $PbTiO_3$ called lead-zirconate-titanate, or PZT. Some of the best performing piezoelectrics (up to five times better than commercial PZT) are compounds that are solid solutions of relaxors like $PbMg_{1/3}Nb_{2/3}O_3$ (PMN) or $PbZn_{1/3}Nb_{2/3}O_3$ (PZN) and $PbTiO_3$ to form the relaxor ferroelectrics PMN-PT and PZN-PT.[2] Although PZT and related materials perform superbly as piezoelectrics, the toxic effects of lead on the physiology of living organisms are well established. The use of PZT demonstrably releases lead into the environment through the evaporation of PbO during calcination and sintering, during machining of PZT components, or after the lifetime of devices from poor compliance with waste disposal or recycling regulations. Global regulatory efforts are in effect to reduce the use of lead in devices to limit environmental exposure. The Waste Electrical and Electronic Equipment (WEEE) directive and the Restriction of Hazardous Substances (RoHS) directive were both drawn up by the European Union in 2003 and subsequently adopted in 2006. These directives restrict the use of six hazardous materials in electronic devices, including lead.[3,4] In the United States, California passed a law in 2006 restricting the sale of electronic devices that are prohibited under the RoHS, and similar statutes will likely be enacted throughout the country.[5] Although actuators and transducers containing lead are currently exempt from these regulations, owing to their huge technological importance and the lack of quality competitive lead-free alternatives, the exception made in regulatory oversight will not last forever. Given this increasing restriction on the use of lead in electronic devices and considering the expected growth in the piezoelectric market, the development of lead-free alternatives to PZT and other lead-based piezoelectrics is a major priority and is considered to be one of the pillar's in the proposed roadmap for advanced ceramics research.[6]

1.4 Thin Films and Strain Engineering

As technological developments continue to focus on micro- and nano-scale devices, thin films of piezoelectric materials are being used and studied more extensively. The additional control that epitaxial strain allows over the properties of thin film piezoelectrics and ferroelectrics has been demonstrated through many studies and reviewed extensively.[7] Biaxial strains of only a couple percent, not possible with bulk ceramics but demonstrably possible in thin film perovskite oxides, have a huge effect on the properties of ferroelectric materials. Biaxial strain can cause materials that are not

ferroelectric at any temperature can be made to be ferroelectric. It can enhance the ferroelectric Curie temperature by hundreds of degrees. The remanent polarization in ferroelectric thin films can be similarly enhanced by strain. As will be shown in this dissertation, strain can also be used to shift the morphotropic phase boundary and potentially induce one in a material that ordinarily has none under ambient conditions.

1.5 Goals of This Research

Given the increased emphasis on thin film ferroelectrics and the need for lead-free alternatives PZT, it is worthwhile to consider and research alternatives to thin film PZT. There have been several extensive reviews published about the ongoing search for high-performing lead-free ferroelectrics.[8-10] The majority of results can be summarized by classifying most of the promising candidates into two main families of materials, $K_{0.5}Na_{0.5}NbO_3$ (KNN) and $Na_{0.5}Bi_{0.5}Ti0_3$ (NBT), but to date these materials are still not considered to be exceptionally competitive with PZT on a toxicity, performance, manufacturability and/or cost basis. It would be ideal to find a material with a simple composition, low environmental toxicity, high availability and competitive performance to PZT in thin films. The possibility of using epitaxial strain to stabilize a morphotropic phase boundary in a compositionally simple lead-free material that ordinarily does not have one under ambient conditions is interesting from a scientific perspective and also from the perspective of progress in environmentally friendly technological advancement.

The general theme of the research detailed in this dissertation is based on that very consideration. The goals are twofold: First, to demonstrate that one can strain engineer thin films of a lead-free material and induce a morphotropic phase boundary at ambient conditions where no such boundary exists in the material's bulk state. Second, assuming success in the above endeavor, to determine to what extent the piezoelectric properties of that material are enhanced compared to its bulk form in consideration of it replacing PZT in some thin film applications.

1.6 Organization of Subsequent Sections

The remainder of this dissertation is divided into six main sections, plus a section with a summary of the conclusions from this work and a final section on recommendations for future research.

Section 2 first provides some theoretical background on piezoelectricity and ferroelectricity. A description is then given on how and why compositions near the morphotropic phase boundary (MPB) in the phase diagrams of high performing piezoelectrics like PZT are associated with the enhanced piezoelectric response in these materials. It is shown that MPBs can be tuned by external mechanical constraints like hydrostatic pressure or biaxial strain, and that these constraints can induce a MPB in a pure compound that does not have one under ambient conditions. In considering a replacement for lead in thin film piezoelectrics, bismuth is presented as a possible replacement cation on the A-site in the perovskite structure, and bismuth ferrite ($BiFeO_3$

or BFO) is introduced with a case made that there may be a MPB in this material that can be stabilized in thin films via epitaxial strain.

Section 3 details the growth of bismuth ferrite thin films. A short background is given on epitaxy, followed by the adopted methodology for the selection of substrates used for the growth of BFO films in this study. Section 3 concludes with a description of pulsed laser deposition, the experimental method used in this study to grow all of the films.

Section 4 is concerned with the structural characterization of the BFO films grown. It begins with an overview of all the structural characterization techniques used. Subsequent subsections include the results from x-ray diffraction and reciprocal space mapping analysis, surface topography analysis via atomic force microscopy, additional structural characterization via optical second harmonic generation (SHG), transmission electron microscopy analysis and finally nano-mechanical perturbation experiments. The results are then corroborated via theoretical models based on the experimental data collected in these studies.

Section 5 details the electrical characterization of the BFO films grown to determine to what extent the piezoelectric and ferroelectric properties have been enhanced. It begins with a discussion on bottom electrode selection and growth, and the electrical testing methods used including piezoforce microscopy (PFM) and quantitative ferroelectric polarization measurements. The results of PFM poling experiments are then presented, demonstrating that the films are ferroelectric and the polarization can be reversibly switched. These results are corroborated via electron diffraction of a BFO film poled *in situ* under TEM analysis. After a description of the method for making top electrode contacts on the films, the results from quantitative ferroelectric testing are given, along with quantitative averaged and localized piezoelectric characterization results.

Section 6 summarizes the results from each of the previous sections and Section 7 discuses some open questions that remain as a result of this study and offers some suggestions for future research.

2 Background

What follows is a simple overview of piezoelectricity and ferroelectricity as it pertains to the work in this study, and an examination of the origins of the enhanced piezoelectric response in the vicinity of a morphotropic phase boundary in PZT with an eye towards finding a lead-free thin film replacement. For more information on the subjects of piezoelectric and ferroelectric materials, including detailed derivations of the thermodynamic equations of state that describe the coupling between the elastic and electrical parameters of a material, the reader is referred to one of the classical textbooks on the topic listed in the references.[11,12]

2.1 Piezoelectricity

When an electric field, E_i, is applied to an insulating material it causes a net polarization in the material through the separation of positive and negative charges. This manifests macroscopically as a surface charge on the material, and can be described by a polarization vector, P_i, with units C/m^2. The linear approximation of the relation between applied field and resulting polarization is:

$$P_i = \chi_{ij} E_j \tag{1}$$

Where χ_{ij} is the dielectric susceptibility 2nd rank tensor with units F/m.

The dielectric displacement vector, D_i, with units C/m^2 is the representation of the resultant surface charge density on the material caused by the applied electric field. It includes the charges associated with the induced polarization of the material, P_i, as well as those due to the polarization of free space, $\epsilon_0 E_i$, and is represented in a linear approximation as:

$$D_i = \epsilon_0 E_i + P_i = \epsilon_0 E_i + \chi_{ij} E_j = \epsilon_0 \delta_{ij} E_j + \chi_{ij} E_j = (\epsilon_0 \delta_{ij} + \chi_{ij}) E_j = \epsilon_{ij} E_j \tag{2}$$

Where $\epsilon_{ij} = \epsilon_0 \delta_{ij} + \chi_{ij}$ is the dielectric permittivity of the material, ϵ_0 is the permittivity of free space and δ_{ij} is the Kronecker Delta function (where $\delta_{ij} = 1$ when $i = j$ and $\delta_{ij} = 0$ when $i \neq j$).

The linear approximation for the relation between an applied stress on an elastic material, σ_{kl}, which is a 2nd rank tensor with units N/m^2, and the resultant strain, ε_{ij}, which is a unitless 2nd rank tensor, is given by Hooke's law:

$$\varepsilon_{ij} = S_{ijkl} \sigma_{kl} \tag{3}$$

Where S_{ijkl} is the elastic compliance 4th rank tensor with units m^2/N.

To this point the general overview has been regarding any insulating materials. A subset of insulating materials is the piezoelectric materials, which generate an electric potential

in response to an applied mechanical stress, a phenomenon called the direct piezoelectric effect. This effect is reversible, in that these materials will also experience a strain and change their dimensions under an applied electric field – called the converse piezoelectric effect. A key figure of merit for piezoelectric materials is the piezoelectric charge coefficient, d, which is a symmetric third rank tensor with units C/N that relates the polarization generated in a piezoelectric material per unit of stress applied to it, or with units m/V that relates the amount of strain experienced by the material per unit of applied electric field. These relationships can be expressed mathematically using the following relations:

$$D_i = d_{ijk}\sigma_{jk} \quad (4)$$

$$\varepsilon_{ij} = d_{ijk}E_k \quad (5)$$

In the above relations, d_{ijk} is the piezoelectric charge coefficient, D_i is the resulting surface charge density caused by an applied stress σ_{jk}, and ε_{ij} is the induced strain by an applied electric field E_k.

Combining the general relations for insulating materials with those describing piezoelectricity results in a mathematical formalism that relates the coupling between the elastic and electrical parameters of a piezoelectric material:

$$D_i = \epsilon_{ij}^{\sigma}E_j + d_{ijk}\sigma_{jk} \quad (6)$$

$$\varepsilon_{ij} = d_{ijk}E_k + S_{ijkl}^{E}\sigma_{kl} \quad (7)$$

Where the superscripts indicate variables that are held constant (for simplicity it is also assumed that the temperature, T, is constant). For purely piezoelectric strain induced by an applied electric field when there is no applied stress, or purely piezoelectric polarization induced by an applied stress when there is no applied field, the equations for a piezoelectric material are simplified to the more familiar forms:

$$P_i = d_{ijk}\sigma_{jk} \quad (8)$$

$$\varepsilon_{ij} = d_{ijk}E_k \quad (9)$$

Where P_i is the induced polarization within the material. Because P and E are vectors, σ and ε are symmetric second rank tensors, and d is a symmetric third rank tensor, these equations can be simplified using Voigt notation:

$$P_i = d_{ij}\sigma_j \quad (10)$$

$$\varepsilon_j = d_{ji}E_i \quad (11)$$

In the above relations, i=1-3 and j=1-6, and these subscripts identify the geometries under which the properties are measured. For example, a commonly measured component of the piezoelectric charge coefficient, particularly in thin films, is the longitudinal charge coefficient d_{33} (in Voigt notation), which is the induced polarization of the material per

unit of stress applied in the same direction as the polarization or, conversely, the induced strain of the material per unit of applied electric field in the same direction as the strain.

Of all the known piezoelectric materials, the complex oxides, and more specifically those that adopt the perovskite crystal structure, generally have the largest piezoelectric coefficients.[12] The perovskite structure is described generally by the formula ABO_3, where A and B are metal cations and O is an oxygen anion. The structure can generally be characterized as a BO_6 octahedron surrounded by octahedrally coordinated A cations, resulting in a stoichiometry of ABO_3 as depicted in **Figure 1**.

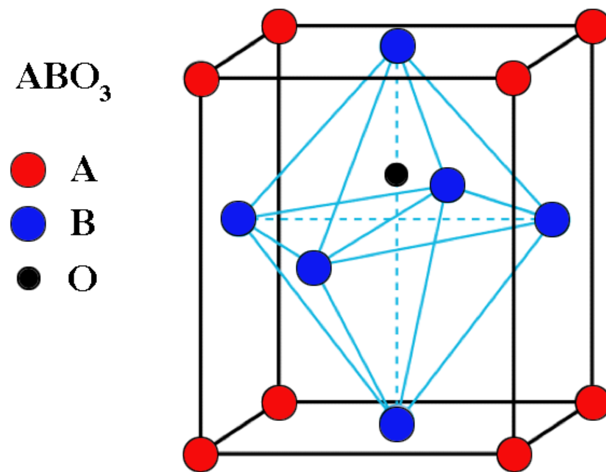

Figure 1. Schematic of a perovskite unit cell with the ABO_3 stoichiometry, where A and B are metal cations and O is an oxygen anion. The structure can generally be characterized as a BO_6 octahedron surrounded by octahedrally coordinated A cations, resulting in the stoichiometry ABO_3.

The A cation in the perovskite structure is usually a monovalent or divalent alkali metal and the B cation is a usually pentavalent or tetravalent transition metal. The perovskite structure allows for many degrees of freedom, which include octahedral tilts and rotations and relative displacements of the cations. This broadly depends on the cations present on the A-site and B-site and their relative size and bonding characteristics. This potential for variation in the structure of perovskite oxides is the reason for the extensive variety of material properties that exists in this family of materials. With regard specifically to piezoelectric perovskite oxides, a schematic of the mechanism of the converse piezoelectric effect in a perovskite unit cell under an applied bias are shown in **Figure 2**.

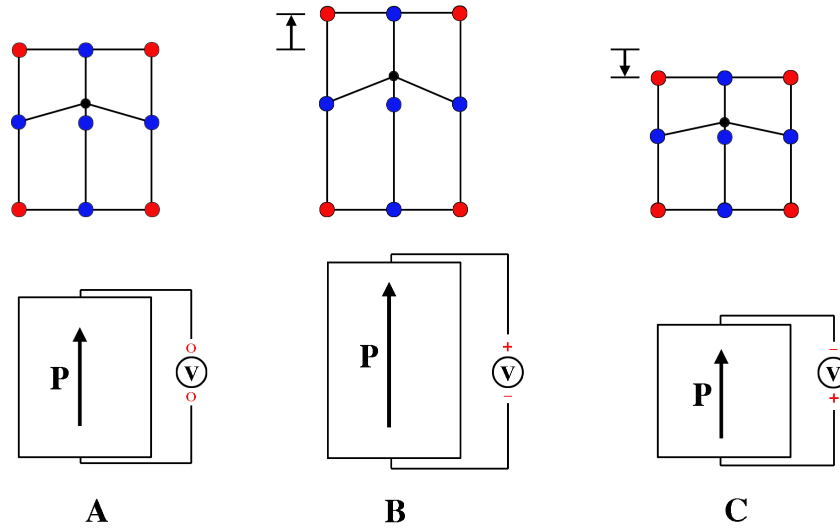

Figure 2. Schematic illustration of the converse piezoelectric effect in a perovskite material with a spontaneous polarization. The top row represents a 2-dimensional projection of the perovskite structure ABO_3 in response to an applied electric field. The bottom row shows the relative magnitude of the polarization, *P*, in response to an applied electric field. **(A)** is under no applied external field, **(B)** has an elongated structure and increased polarization under an applied electric field of the same polarity as *P*, and **(C)** has a compressed structure and decreased polarization under an applied electric field of opposite polarity as *P*.

The top row of **Figure 2** represents a 2-dimensional projection of the perovskite structure ABO_3 in response to an applied electric field. The bottom row shows the relative magnitude of the polarization, *P*, in response to an applied electric field. **Figure 2(A)** is under no applied external field, **Figure 2(B)** has an elongated structure and increased polarization under an applied electric field of the same polarity as P, and **Figure 2(C)** has a compressed structure and decreased polarization under an applied electric field of opposite polarity as *P*. In most piezoelectric perovskites, including all those discussed in this study, the piezoelectric strain can be described as a relative distortion of the B cation in relation to the oxygen octahedral structure.

2.2 Ferroelectricity

The best piezoelectrics also tend to be ferroelectric, and what follows will be an overview discussion on ferroelectricity. Of the 32 crystallographic point groups, 21 of them lack a center of symmetry and of these non-centrosymmetric point groups, 20 of them are piezoelectric.[13] Within this sub-group, only 10 have a unique polar axis and exhibit a temperature dependent spontaneous polarization (P_s). Ferroelectric materials are those with two or more polarization orientation states in the absence of an electric field that can be switched between those states when an electric field is applied. It is important to note that each polarization orientation state is crystallographically equivalent, with equal polarization values and the same amount of elastic distortion - the only difference is the direction of the polarization vector. These different polarization orientation states can be

visualized as a double-well energy potential, symmetric about the center of the unit cell. In applying a strong enough electric field, one can transition the cation over the energy barrier and into one of the other available polarization orientation states and thus change the direction of the polarization and the strain state of the system.

2.2.1 The Curie Temperature

The Curie temperature, T_c, is the temperature unique to each material above which nearly all ferroelectrics lose their spontaneous polarization. Sometimes this is the result of the thermal energy being high enough such that the polarized ion can oscillate rapidly between the two polarization orientations, effectively cancelling out the time-averaged polarization. In perovskite ferroelectrics, it is more often the result of a phase transformation to a centrosymmetric, non-polar and paraelectric cubic phase. Above the Curie temperature the structure is cubic; below the Curie temperature the structure becomes distorted, extending the cubic cell along the axis of polarization and breaking the symmetry of the paraelectric phase. Some perovskite ferroelectrics have more than one temperature dependent phase transition, and these can be different ferroelectric phases or even non-ferroelectric ones. The temperature dependent properties related to thermal, dielectric or elastic behavior often show anomalies near these phase transition temperatures due to instabilities and degenerate states. A classic example of this is the observed huge increase in dielectric permittivity near the Curie temperature as illustrated in **Figure 3**. This increase in the permittivity near the Curie temperature is indicative of a ferroelectric-paraelectric phase transition and a result of the highly polarizable state due to the structural instability and degeneracy of the two crystallographic phases.

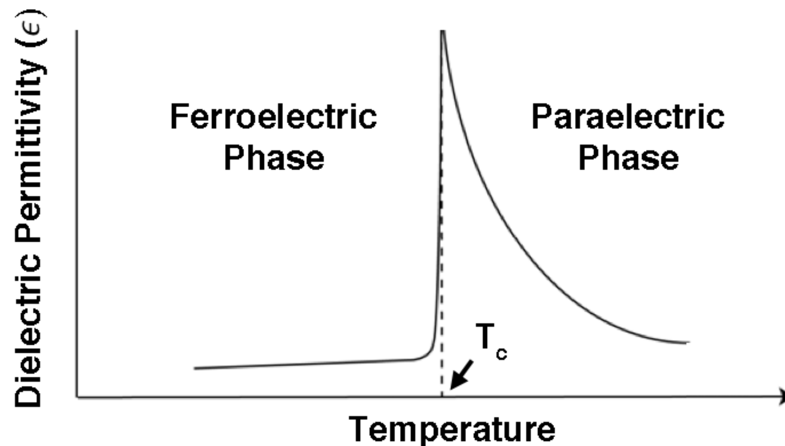

Figure 3. A simple schematic showing the typical variation of the dielectric permittivity (ϵ) as a function of temperature for a normal ferroelectric near the Curie temperature. The permittivity is marked by a sharp increase near the ferroelectric-paraelectric phase transition.

2.2.2 Domains and Hysteresis

Real ferroelectric materials contain many ferroelectric domains, or areas where a single polarization orientation variant exists. These domains point in various directions relative to each other such that the net polarization is zero. Ferroelectric domain walls separate areas with different polarization vector directions and ferroelastic domain walls separate areas with different (non-cubic) crystallographic orientations. Because of this, ferroelectric materials are characterized by a polarization-electric field (P vs. E) hysteresis loop and a strain-electric field (ε vs. E) hysteresis loop. As shown in **Figure 4(A)**, when an electric field is applied to a ferroelectric material it initially behaves like a normal dielectric, exhibiting a linear response. As the field increases, the ferroelectric domains that are aligned with the field are energetically favored over those that are not, and the domain walls move accordingly. This results in a non-linear increase in the overall polarization until domain wall motion ceases and the polarization is saturated.

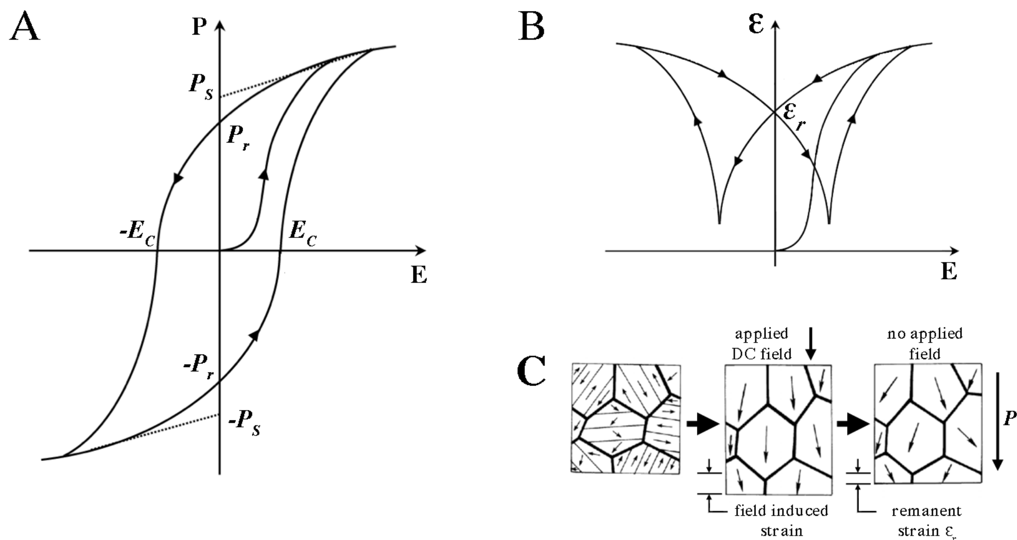

Figure 4. Due to the presence of ferroelectric and ferroelastic domains, ferroelectric materials are characterized by a polarization-electric field (P vs. E) hysteresis loop **(A)** and a strain-electric field (ε vs. E) hysteresis loop **(B)**. A schematic of the polarization and strain effects happening on a domain level in the material shows the origin of the hysteresis **(C)**.

Upon removal of the electric field, some domains remain aligned in the direction of the previously applied field, exhibiting a remanent polarization, P_r, at zero electric field. As the field is reversed, domain wall motion occurs favoring those domains aligned with the new electric field direction. The point in the loop where the net polarization is zero is called the coercive field E_c. The polarization can be saturated once again in the opposite direction upon increasing the reversed field strength further, and as the field is removed and applied again in the opposite direction the P vs. E hysteresis loop is completed. Similarly, the strain-electric field (ε vs. E) plot in **Figure 4(B)** shows hysteresis due to

the converse piezoelectric effect and the switching and movement of the domain walls. In **Figure 4(B)** with no applied field, the strain is zero. When the field is applied in the same direction as the spontaneous polarization in the material, the crystal expands. When the field is decreased and brought back to zero, the material maintains a remanent strain ε_r. As the field is then increased antiparallel to the spontaneous polarization, the crystal contracts until the polarization in the crystal is switched – this is point at the bottom of the curve in **Figure 4(B)** – and subsequently the strain again becomes positive. The loop is completed when the field is again reversed and the curve is traced through the remanent strain point and back to the maxima on the other side. The progression depicted in **Figure 4**(C) shows the evolution of the ferroelectric and ferroelastic domains through the application of the applied field and subsequent removal. Upon the application of the field, the spontaneous polarizations within each grain begin to align with the field, causing the domains to elongate in the direction of the field. When the field is removed, a remanent polarization and remanent strain remain in the crystal.

2.3 Morphotropic Phase Boundaries

The term "morphotropic phase boundary" (MPB) was originally used to refer generally to phase transitions due to changes in composition.[14] It is now mainly used in the scientific literature to describe the boundary that separates regions of rhombohedral symmetry with regions of tetragonal or orthorhombic symmetry in the binary phase diagrams of ferroelectric oxides. Materials with compositions near this boundary exhibit a greatly enhanced piezoelectric response relative to compositions far from the boundary. The quintessential example of a ferroelectric with a MPB in its phase diagram is the most commonly used piezoelectric – lead zirconate titanate ($PbZr_{(1-x)}Ti_xO_3$) or PZT, which is a solid solution of $PbZrO_3$ and $PbTiO_3$, and which has an ambient pressure morphotropic phase boundary composition of $PbZr_{0.52}Ti_{0.48}O_3$. A simple binary phase diagram for PZT is shown in **Figure 5**. In the phase diagram, the high temperature centrosymmetric cubic phase is at the top of the diagram above the compositionally dependent Curie temperature. Below the cubic phase, ferroelectric rhombohedral and tetragonal phases are energetically favorable depending on the composition. In the middle of the diagram, the morphotropic phase boundary (MPB) between the rhombohedral and tetragonal phases can be seen. It is near this phase boundary that PZT has anomalously enhanced piezoelectric properties.

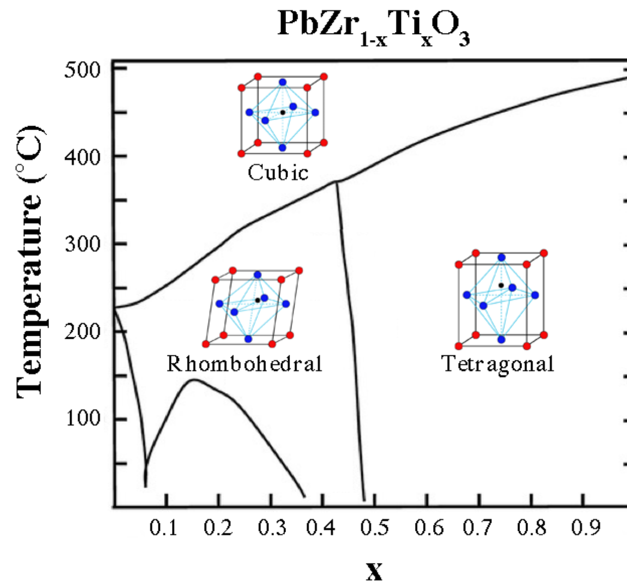

Figure 5. A simple phase diagram for PZT. The high temperature centrosymmetric cubic phase is at the top of the diagram above the compositionally dependent Curie temperature. Below the cubic phase, ferroelectric rhombohedral and tetragonal phases are found, depending on the composition. In the middle of the diagram, the morphotropic phase boundary between the rhombohedral and tetragonal phases can be seen. It is near this phase boundary that PZT has anomalously enhanced piezoelectric properties.

2.3.1 Origins of Enhanced Properties

The origins of the enhanced piezoelectric response in ferroelectric materials with compositions near the morphotropic phase boundary has most commonly been described using a polarization rotation model, which requires the presence of a monoclinic phase (or phases) in the material's phase diagram between the rhombohedral and tetragonal or orthorhombic phases. In this model the monoclinic phase (or phases) is nearly energetically degenerate with the phases on either side of the MPB and forms a structural bridge between the them. The ferroelectric polarization then lies within a mirror plane in the monoclinic phase, allowing unrestricted polarization rotation resulting in the observed large electromechanical response.[15-21] This model has been challenged by some research groups on the grounds that the appearance of the monoclinic structure observed in x-ray diffraction data is the result of a nanodomain structure of tetragonal and rhombohedral phases, whereby the resulting nanotwin superlattices mimic the diffraction peaks of monoclinic phases.[22-25] These disagreements about the structures of specific materials at their phase boundaries will be settled in time, but neither theory cuts to the fundamental nature of the issue. It has been demonstrated that polarization rotation is only one mechanism for this kind of enhanced response; there are examples of materials that exhibit enhanced piezoelectric response without the presence of any monoclinic phases or nanodomains mimicking such phases in diffraction spectra; and there are examples of monoclinic ferroelectric crystals with unremarkable piezoelectric properties.[26-31]

A more elegant model, first proposed nearly 40 years ago and now gaining more general acceptance, is that the free energy instability or "flat energy surface" near a structural phase boundary is the origin of the enhanced piezoelectric response in these materials.[32] Experimental and theoretical evidence suggests that the highest piezoelectric response in these materials is observed not in the monoclinic phases themselves, but at the boundary between the phases where the polarization either emerges from a non-polar state or changes direction across the phase boundary. The monoclinic phases are just commonly (but not exclusively) found as structural bridges between other polar phases, so it can be easily misconstrued that they are the necessary factor. Near the phase boundaries in these materials, there is a pronounced increase in the dielectric susceptibility perpendicular to the spontaneous polarization (χ_{11} or $\chi_{\perp}$), which results in an increase in the longitudinal piezoelectric coefficient along the non-polar axis.

This can be demonstrated using tensor analysis. For simplicity, the following analysis is focused on a tetragonal crystal belonging to the *4mm* point group but can be extended to other symmetries. In crystals with the *4mm* symmetry, the spontaneous polarization P_s points along the <001> pseudocubic direction. Letting a field $E = (E_1, E_2, E_3)$ be applied to the crystal, the polarization becomes

$$\begin{pmatrix} P_1 \\ P_2 \\ P_3 \end{pmatrix} = \begin{pmatrix} 0 \\ 0 \\ P_S \end{pmatrix} + \varepsilon_0 \begin{pmatrix} \chi_{11} & 0 & 0 \\ 0 & \chi_{11} & 0 \\ 0 & 0 & \chi_{33} \end{pmatrix} \begin{pmatrix} E_1 \\ E_2 \\ E_3 \end{pmatrix} \tag{12}$$

or

$$P = P_S + \varepsilon_0 \chi E = P_S + \Delta P \tag{13}$$

where P_S is the spontaneous polarization vector, ε_0 is the permittivity of the vacuum and χ_{ij} is the dielectric susceptibility tensor. If one lets $E_1 = E_2$ for simplicity, the resulting polarization will then lie in the (110) pseudocubic plane. The angle between the original spontaneous polarization and the field-induced polarization directions is

$$\tan\alpha = \frac{\sqrt{\Delta P_1^2 + \Delta P_2^2}}{P_S + \Delta P_3} = \frac{\sqrt{2}\varepsilon_0 \chi_{11} E_1}{P_S + \varepsilon_0 \chi_{33} E_3} \tag{14}$$

Thus, the extent of the angle of polarization rotation will depend on the magnitude of the applied field perpendicular to the spontaneous polarization and on the anisotropy of the dielectric susceptibility of the material (χ_{11}/χ_{33}). The manner in which dielectric susceptibility and polarization rotation are related to the large piezoelectric responses easily follows. The longitudinal, transverse and shear piezoelectric coefficients for a tetragonal crystal with *4mm* symmetry can be written respectively as:

$$d_{33} = 2\varepsilon_0 \chi_{33} Q_{11} P_3 \tag{15}$$
$$d_{31} = 2\varepsilon_0 \chi_{33} Q_{12} P_3 \tag{16}$$
$$d_{15} = 2\varepsilon_0 \chi_{11} Q_{44} P_3 \tag{17}$$

where $P_3 = P_S$ and Q_{ij} are the electrostriction coefficients. For an arbitrary direction not parallel to the spontaneous polarization direction, the longitudinal piezoelectric coefficient is:[13,33]

$$d_{33}^{*}(\theta) = \cos\theta\,[(d_{15} + d_{31})\sin^{2}\theta + d_{33}\cos\theta] \quad (18)$$

where θ is the angle of rotation away from the polar axis that the coefficient is being measured. In most ferroelectrics, the transverse coefficient d_{31} is negative and smaller in value than d_{33} and d_{15}. Thus, when $\theta \neq 0$ (away from the polar axis), $d_{33}^{*}(\theta)$ is large if the shear coefficient d_{15} is large, i.e when χ_{11} is large. A similar, albeit slightly more involved, analysis can be made for rhombohedral and orthorhombic crystal symmetries.[26, 34] Analyses on the same topic have also been made using Landau-Devonshire analysis and *ab inito* methods, with similar conclusions.[32-40]

2.3.2 Tuning the Phase Boundary

The fact that the piezoelectric properties of ferroelectric perovskite oxides are greatly enhanced in the vicinity of morphotropic phase boundaries is the basis for a lot of materials science research focused on finding new materials with such boundaries in their phase diagrams. This has predominantly been done via chemically alloying a ferroelectric material to make a solid solution that has a MPB at some specific stoichiometry, such as the cases of PZT, PMN-PT and PZN-PT. However, as will be shown in the next subsections, it has ben demonstrated theoretically and experimentally that MPBs can be induced in pure phase ferroelectric materials as well.

2.3.2.1 Hydrostatic Pressure

At ambient temperature and pressure, $PbTiO_3$ has no morphotropic phase boundary in its phase diagram. Recent first principle *ab initio* calculations show that under increasing hydrostatic pressures in excess of 9 GPa there exists a tetragonal-to-monoclinic-to-rhombohedral-to-cubic phase transition in this material.[41,42] In conjunction with this pressure-induced phase boundary, the results show very large dielectric and piezoelectric coupling constants occurring in the regions of the phase transitions. These theoretical results have since been confirmed experimentally, even indicating multiple monoclinic phases between the tetragonal and rhombohedral phases with increasing pressure.[43] It is interesting in the context of these high hydrostatic pressure studies to consider the creation of PZT by alloying $PbTiO_3$ with $PbZrO_3$ as effectively applying a "chemical pressure" to $PbTiO_3$ which lowers the energy of the rhombohedral phase under ambient pressure. It is a remarkable result that allows one to consider that complex compositions and microstructures like those of PZT, PZN-PT and PMN-PT may not be necessary for high performing piezoelectrics.

2.3.2.2 Biaxial Strain

Thermodynamic calculations for pure lead titanate suggest that a tetragonal-rhombohedral phase boundary can also be induced in this material under a relatively large tensile biaxial strain.[44] Similar to the hydrostatic pressure effects above, the biaxial tension preferentially lowers the energy of the rhombohedral phase. Biaxial strain affects the MPB in PZT as well. Thermodynamic calculations and phase field modeling for PZT thin films suggest the morphotropic phase boundary composition can be shifted by the epitaxial strain induced by an underlying substrate. This has been corroborated experimentally by growing thin films of PZT on MgO(001) substrates, applying an in-plane compressive strain. PZT films with compositions in the Zr-rich region of the phase diagram, which would be rhombohedral in the bulk, were found to show a two-phase coexistence of rhombohedral and tetragonal phases, and in the case of very thin films under high compressive strain they were entirely tetragonal.[45,46] The results of these investigations are consistent with the idea that pressure – in this case of a biaxial nature – can be used to shift the morphotropic phase boundary in ferroelectric perovskite oxides.[47-48] In summary, epitaxial strain can be a useful tool in manipulating the MPB in ferroelectric perovskite oxides, either by inducing one in a pure material, or by changing the MPB composition for one in a solid solution. In either case, the difference in energy between the stable and metastable phases is reduced to the point where the phases become nearly degenerate.

2.4 An Alternative to PZT

As stated previously, PZT is the most widely used piezoelectric material. In setting out to find a suitable replacement material in which to strain engineer an MPB, it is useful to consider the structural characteristics of PZT on either side of the phase boundary and use those as a starting point. The material should be a good ferroelectric with a rhombohedral or tetragonal ground state at room temperature and it should have a relatively high Curie temperature. A simple material without the need for complex solid solutions would be ideal. It should be easy to grown in thin film form via epitaxy and some evidence for monoclinic distortions of the unit cell would be of benefit as it has already been established that they are often a bridge phase at the MPB. Also, because the goal of this research is to strain engineer an MPB in a lead-free material, it is useful to consider the specific role of Pb in the properties of $PbTiO_3$ and by extension PZT.

2.4.1 The Role of Lead

In an ideal cubic perovskite structure, each cation is the perfect size to be in contact with an oxygen atom, and the radii of the ions can be related by:

$$R_A + R_O = \sqrt{2}(R_B + R_O) \tag{19}$$

where R_A, R_B and R_O are the ionic radii of the A site cation, B site cation and oxygen anion respectively. Very few materials adopt a perfect perovskite structure because the A-site and B-site cations are often different sizes, resulting in distortions to the perfect

cubic perovskite structure. A constant, t, called the tolerance factor can be included in the relation to account for this, such that:

$$R_A + R_O = t\sqrt{2}(R_B + R_O) \tag{20}$$

The tolerance factor can be used as a measure of the degree of distortion from an ideal cubic perovskite structure.[49,50] When $t > 1$, as in perovskites like $BaTiO_3$, the material is said to be B-site driven in that the B-site cation is nominally too small for its site. This energetically favors displacements that bring the B-site cation away from the center of the oxygen octahedron, which usually results in a ground state rhombohedral structure and ferroelectricity if t is sufficiently large Conversely, when $t < 1$, as in perovskites like $GdFeO_3$, the material is considered to be A-site driven. When the A-site cation is too small to stay in contact with the oxygen anions in the cubic perovskite structure, it energetically favors tilt and rotational displacements of the BO_6 octahedra. These materials are generally not ferroelectric, but the common notable exceptions are perovskites with Pb^{2+} as the A-site cations, where A-site driven ferroelectricity generally occurs along with enhanced piezoelectricity near a morphotropic phase boundary.[51] The role Pb plays in this can be understood in terms of the electronic structure of the Pb^{2+} cation, which has a relatively high and extended occupied 6s orbital and a relatively low and extended unoccupied 6p orbital. In the perovskite structure this is often discussed in terms of the "polarizable lone electron pair" but is more accurately described as hybridization between occupied O 2p states and unoccupied Pb 6p states across the bandgap, similar to the cross-gap hybridization between B-site cations and oxygen ions in B-site driven ferroelectrics.[52]

2.4.2 Bismuth on the A-Site

Elements from the bottom of Group 13, Group 14 and Group 15 in the periodic table – thallium (Tl), lead (Pb), and bismuth (Bi) respectively – all contain similar asymmetric electron densities. Thallium and its compounds are extremely toxic and are not considered as a viable alternative to lead.[53,54] Studies show that bismuth, however, is the least toxic of all the heavy metals and has almost no harmful effects on living organisms.[55-57] It is also relatively inexpensive compared to other elements commonly considered for lead-free piezoelectrics.[58] Bismuth, like lead, has a sterically active lone electron pair, and for this reason bismuth based perovskites have often been alloyed with $PbTiO_3$ in an effort to create high performing piezoelectrics with nominally less lead in their composition compared to PZT.[59-62] In considering a simple perovskite oxide with Bi on the A-site, $BiFeO_3$ was selected for this study because it has a rhombohedral ground state with monoclinic distortions when in thin films, a high Curie temperature, and a plentiful and environmentally friendly B-site cation in iron.

2.5 Bismuth Ferrite

$BiFeO_3$ (bismuth ferrite, or BFO) is a complex oxide that in its bulk single crystal form is rhombohedral (space group: *R3c*, point group: *3m*) with lattice parameters a_{rh} = 5.63 Å

and α_{rh} = 59.3°.[63-65] It can more easily be visualized as a distorted cubic perovskite with pseudo-cubic lattice parameters a_{pc} = 3.96 Å and α_{pc} = 89.5°. (The pseudocubic Miller indices will be used throughout this text unless otherwise noted). The structure of BFO is succinctly described as two distorted perovskite cells connected along the pseudocubic <111> body diagonal, resulting in a rhombohedral unit cell as depicted in **Figure 6**.

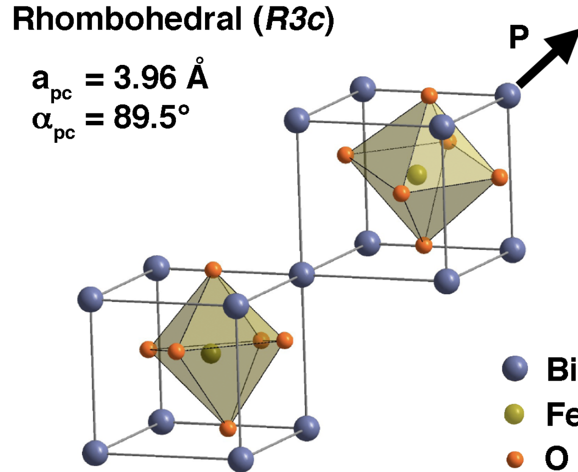

Figure 6. The structure of $BiFeO_3$ can be visualized as a distorted cubic perovskite with pseudo-cubic lattice parameters a_{pc} = 3.96 Å and α_{pc} = 89.5°. Here it is shown as two distorted perovskite cells connected along the pseudocubic <111> body diagonal, resulting in a rhombohedral unit cell. The two oxygen octahedra in this structure are alternately rotated about $<111>_{pc}$ direction by ~13.8(3)°, and the Fe cations are shifted by 0.135 Å along the same axis away from the center of the oxygen octahedra.

The two oxygen octahedra in this structure are alternately rotated about $<111>_{pc}$ direction by ~13.8(3)°, and the Fe cations are shifted by 0.135 Å along the same axis away from the center of the oxygen octahedra.[65,66]

2.5.1 A-Site Driven Ferroelectricity

BFO is ferroelectric, with a notably high Curie temperature of T_c ~ 1103 K. In a similar manner to $PbTiO_3$, the ferroelectric state in BFO is A-site driven and marked by a displacement of the Bi cations relative to the FeO_6 octahedra.[65,66] The spontaneous polarization of BFO is oriented along the pseudocubic <111> direction and was historically measured to be 6.1 μC/cm, considered to be comparatively quite low for a material with such a high Curie temperature.[67] However, more recent studies on single crystal thin films of BFO showed a dramatic enhancement of the spontaneous polarization up to ~90 μC/cm^2 at room temperature.[68-70] These experimental results were later corroborated via theoretical studies finding predicted spontaneous polarization values of 90-100 μC/cm^2.[71] Careful structural characterization experiments using synchrotron x-ray diffraction demonstrated a change in phase stability from the bulk

rhombohedral phase to a modified monoclinically distorted rhombohedral phase in epitaxial thin films.[72] In addition, the longitudinal converse piezoelectric coefficient (d_{33}) in these films has been measured to be 60-70 pm/V.[66,68,73,74]

2.5.2 Evidence for a Tetragonal Phase

Several theoretical reports suggest the possible existence of a tetragonal phase of BFO with a high *c/a* ratio and large spontaneous ferroelectric polarization. Using first principles calculations on the effect of epitaxial strain on BFO, a theoretical variant of BFO with *P4mm* symmetry was predicted with lattice constants a = 3.665 Å and c = 4.655 Å, a *c/a* ratio of 1.27, and a spontaneous ferroelectric polarization of ~150 $\mu C/cm^2$.[75] Similar results soon corroborated this initial study with lattice constants of a = 3.67 Å and c = 4.64 Å, a *c/a* ratio of 1.26, and similar polarization values predicted.[76] In line with these investigations, theoretical studies on the hydrostatic pressure effects on the structure of BFO was conducted and a variant of BFO with *P4mm* symmetry was predicted with lattice constants a = 3.786 Å and c = 4.853 Å, and a *c/a* ratio of 1.28.[77] If correct, this phase of BFO would be among the perovskite oxides with the highest *c/a* ratios comparable to $PbVO_3$ (*c/a* = 1.23),[78,79] $BiCoO_3$ (*c/a* = 1.27),[80] $BiScO_3$ (*c/a* = 1.28),[81] $BiGaO_3$ (*c/a* = 1.30),[82] and $BiYO_3$ (*c/a* = 1.37).[81]

2.6 General Experimental Approach

Considering the aforementioned evidence for a tetragonal phase in BFO, and the fact that its ground state in thin films is a monoclinically distorted rhombohedral phase, it is a reasonable assumption that a morphotropic phase boundary exists in this material and that it may be possible to stabilize it using epitaxial constraints. The remainder of this dissertation will detail the growth of BFO thin films under compressive epitaxial strain in an effort to stabilize such a boundary, and the subsequent characterization of these films to verify their structure and their piezoelectric and ferroelectric properties.

3 Growth of BFO Thin Films

The first half of the research objectives laid out in Section 1 is to epitaxially stabilize a MPB in a lead-free material. $BiFeO_3$ (BFO) has been selected as the candidate material for the effort. The first step will be to attempt to grow the theoretical tetragonal phase of BFO on substrates that epitaxially apply a compressive in-plane strain. If a tetragonal phase BFO film can be grown and its structure verified, it will verify the overall experimental approach in using epitaxial strain to preferentially energetically favor a metastable phase over a stable bulk-like phase in this material. Subsequent efforts will be focused on tuning the strain state of the film such that the induced energetic favorability is reduced until the two phases become nearly degenerate at the phase boundary.

3.1 Thin Films and Epitaxy

Epitaxial growth is the deposition of a single-crystal film on top of a crystalline substrate. The smooth crystalline surface of the substrate effectively provides an atomic-scale template for the growing film. Homoepitaxy refers to the growth of a thin film material on a substrate that is made of the same material. A common example is the growth of doped silicon on an undoped silicon substrate, a process that lies at the core of the entire semiconductor processing industry. The resultant film, if processed in a clean-room environment under controlled conditions, can be effectively free of defects and have a different functionality from the underlying substrate as a result of the selective doping of the deposited material. By contrast, heteroepitaxy refers to the growth of a thin film material on a substrate that is made of a different material than the one being deposited, but which has a similar structure that in turn affects the structure of the deposited film.[83-85] A schematic illustrating how epitaxy involves lattice matching the film to the substrate is shown in **Figure 7**.

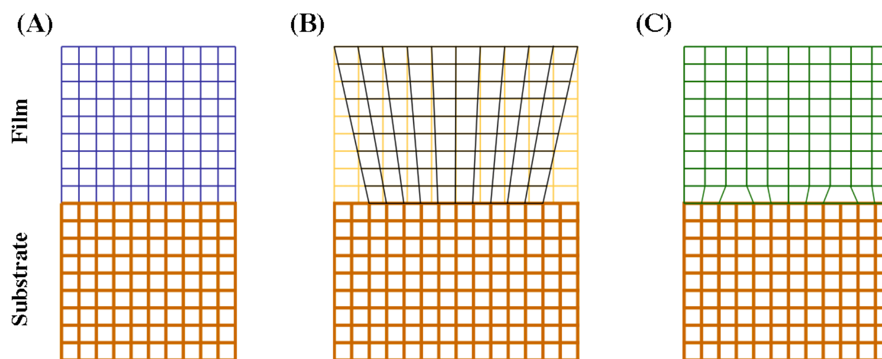

Figure 7. Schematic illustration of epitaxial thin film growth when **(A)** the substrate and film are almost perfectly lattice matched, **(B)** the interface is strained but defect-free, and **(C)** the interface is relaxed due to the formation of misfit dislocations at the interface.

If the film and substrate are the same material, as they are in homoepitaxy, or if they are different materials but have the same or almost the same lattice parameter, an interface with little to no structural disruption like that depicted in **Figure 7(A)** will result. If the film and substrate have dissimilar lattice parameters the resulting interface will look like that in **Figure 7(B)** or **Figure 7(C)**. In **Figure 7(B)**, the interface is strained but defect-free and the film adopts a distorted structure from its bulk form and relaxes through the thickness of the film. This is the type of interface that is typically formed for very thin films when the substrate and film have the same crystal structure and a small lattice mismatch. In **Figure 7(C)** the interface is relaxed due to the formation of defects near the interface, typically misfit dislocations or stacking faults, which allow the film material to adopt its bulk-like structure. This type of interface results when the lattice mismatch between the two materials is relatively large or they have different crystal structures. The lattice mismatch, f, between film and substrate can be calculated using the following relation:

$$f = \frac{2(a_f - a_s)}{a_f + a_s} \sim \frac{a_f - a_s}{a_s} \sim \frac{a_s - a_f}{a_f} \quad (21)$$

In this relation, a_f and a_s are the in-plane lattice parameters of the film and substrate, respectively. As a general rule, the lattice mismatch f must typically be less than 0.1 for epitaxial growth. If the mismatch is any larger, not enough atoms on the bottom surface of the film line up with the atoms on the top surface of the substrate to reduce the interfacial energy and grow the film epitaxially.[83-85]

3.2 Substrate Selection

In attempting to stabilize a theoretical metastable tetragonal phase of bismuth ferrite via epitaxy, one of the most important criteria is the selection of an appropriate substrate.[7] The first criteria in substrate selection are that it must be the same structure as the desired film, be of a specified crystallographic orientation to control the film orientation, and be highly polished to ensure an epitaxial relationship with the film. For this reason, only single-crystal perovskite oxide substrates with a high directional tolerance were used in this work (1 mm thick substrates, < 0.5° of specified orientation). Because the goal is to stabilize a MPB between a tetragonal phase and a rhombohedral phase, the selected substrate should be close to cubic in-plane. BFO has a ground state rhombohedral structure and thus the selected substrate should impose a compressive epitaxial strain to preferentially lower the energy of the tetragonal phase to that of the rhombohedral phase. Thus, the pseudocubic in-plane lattice parameter of a perovskite oxide substrate is a primary parameter to consider. Given the above considerations, and working within the subset of high quality commercially available substrates, the substrates chosen for exploring the phase space of bismuth ferrite under epitaxial compression are detailed in **Table 1**.

Substrate	Substrate *a* (Å)	BFO_T Mismatch (%)	BFO_R Mismatch (%)
$YAlO_3$(110)	3.681	0.436	-7.30
$LaAlO_3$(001)	3.793	3.43	-4.31
LSAT(001)	3.869	5.42	-2.33
$SrTiO_3$(001)	3.905	6.34	-1.40
$DyScO_3$(110)	3.951	7.51	-0.228

Table 1. List of substrates used in this study, their in-plane lattice parameters and their lattice mismatch with the theoretical epitaxially strained tetragonal BFO and the known bulk phase rhombohedral BFO. The in-plane lattice parameters listed are pseudocubic in the case of orthorhombic or rhombohedral substrates. The stoichiometry of LSAT is $(LaAlO_3)_{0.3}(Sr_2AlTaO_6)_{0.7}$.

The substrates are listed in **Table 1** with their cubic or pseudocubic in-plane lattice parameters, lattice mismatch with the tetragonal phase (a ~ 3.665 Å) and lattice mismatch with the rhombohedral phase (a ~ 3.96 Å) of BFO. From **Table 1**, the best substrates for stabilizing the tetragonal phase of BFO are likely to be $YAlO_3$ (YAO), with a lattice mismatch of just 0.436%, and $LAlO_3$ (LAO), with a lattice mismatch of 3.43%. In comparing the lattice mismatch values of the substrates with both phases of BFO, the substrate with the best in-plane lattice parameter for finding and stabilizing a phase boundary between the two phases is LAO. Thus, if the morphotropic phase boundary in BFO exists and can be stabilized via epitaxy, LAO appears to be a good choice of substrate for the purpose.

3.3 Pulsed Laser Deposition

There are a variety of deposition methods that allow for the efficient synthesis of thin films including sputtering, chemical vapor deposition (CVD), and various physical vapor deposition techniques like evaporation, molecular beam epitaxy (MBE) and pulsed laser deposition (PLD).[83,84] CVD and evaporation are desirable methods for the production of large quantities of thin films because they are comparatively cheap and are quite scalable. However, oxide thin film deposition for the purposes of conducting research is dominated by pulsed laser deposition because of its advantages in film thickness and stoichiometry control, and by the large variability of source materials available.

In the context of growing oxide thin films, pulsed laser deposition (PLD) is a technique by which a high-energy laser beam, typically 0.5 – 1.5 Joules (J), is incident on a solid ceramic target of the material that is to be deposited epitaxially on a carefully chosen crystalline oxide substrate.[86] Excimer lasers (short for "excited dimer"), such as the KrF gas lasers used in this study, are typically used because the ultraviolet wavelength of coherent light they generate (248 nm for KrF lasers) is strongly absorbed by oxide materials. In addition, the technique is well suited to the deposition of material systems with multiple constituents, such as complex oxides, because the high energies involved allows for the congruent evaporation of all the species in the target material regardless of

their relative partial pressures. It is also a desirable technique for conducting broad research on new materials and material systems because the targets are relatively easy and cheap to create, and the method itself allows for the rapid iteration of process parameters.

The growth process happens inside a pumped down vacuum chamber, where the oxygen partial pressure can be carefully controlled, containing one or more oxide targets oriented opposite a crystalline substrate adhered to a resistive heater with a small amount of silver paint to ensure good thermal contact. A schematic of a typical PLD chamber is shown in **Figure 8**.

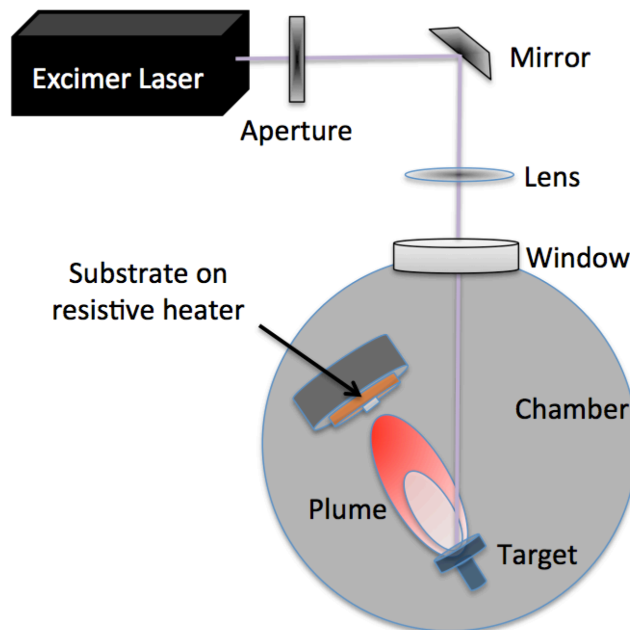

Figure 8. Schematic of a pulsed laser deposition (PLD) system showing the KrF excimer laser on the upper left, beam control optics on the upper right, and vacuum chamber on the bottom. The laser beam is shown as incident on the rotating ceramic target within the vacuum chamber along with the resultant plume of plasma. The interaction results in the stoichiometric deposition of target material on the substrate adhered to a resistive heater.

During the PLD process, the chamber is first evacuated to a base pressure of ~10^{-7} Torr and then backfilled with oxygen to the desired deposition pressure. This is necessary to reduce the effects of oxygen vacancies, which can greatly affect the properties of oxide films.[86] The substrate is then heated to the desired deposition temperature at a rate of ~20 ˚C/min, the laser is brought up to the desired energy and pulse frequency for the deposition, and the beam is brought incident to the target which generates a plasma plume of evaporated species with energies of ~1-10 eV incident on the substrate. During the deposition, the target is rotated continuously to evenly distribute its ablation. Once the desired thickness of the film is reached, another target can be rotated into the path of

the laser if more than one layer is being grown *in situ*. Once the deposition process is complete, the chamber is usually flooded with oxygen to just below ambient pressure to again minimize the formation of oxygen vacancies in the film during cooling, and the substrate is cooled to room temperature at a rate of ~5˚C/min to avoid thermal shock. The overall process of PLD is quite versatile in that growth of materials can be performed at temperatures ranging from 450 to 850 °C and pressures of 10^{-7} to 100 Torr.

Although the overall growth rate for PLD is similar to that of other deposition methods, PLD is unique in that the deposition rate is considerably faster. The laser pulses are quite short, on the order of 10-40 ns, and the target is continuously rotating during the deposition process. There is a large amount of material ablated with each pulse and there is a relatively large amount of time between pulses for diffusion to occur on the substrate. The high energy of the incident atoms and clusters on the substrate allow for high adatom mobility despite the fact that thermalization with the substrate occurs quickly. This allows for the incident atoms to diffuse for several microns on the substrate surface and form large flat grains of single-crystal material. The supersaturation of ablated material on the substrate from each pulse of the laser during PLD results in smoother films compared to MBE or sputtering.[87-90] Essentially, the degree of crystallinity in a thin film grown via PLD is the result of two competing processes. The thermodynamic ground state imposed on the growing film by the epitaxial constraint of the underlying substrate tends towards the creation of a single-crystalline film. On the other hand, the thin-film growth process, which is essentially governed by a nucleation and growth mechanism where individual nucleation sites on the substrate surface grow to meet each other, tends towards the creation of a polycrystalline film. The result of these two competing processes is a predominantly single-crystal film with some degree of polycrystallinity in the form of low-angle grain boundaries throughout the film.

There are some drawbacks to the PLD technique. The plume geometry only allows for a very narrow forward angle distribution so that the usable area of the heater is limited to about 5 cm^2, contributing to the lack of scalability for the technique. In addition, relatively large ejected particles from the target can arrive on the substrate creating micron sized "boulders" and affecting the quality and roughness of the film.[86] This can be mitigated to some degree by adjusting the energy density of the laser spot on the target, such that incongruent melting is avoided on the low end and ejected particles from a shock wave in the target is avoided on the high end.

The laser used for this work was a Lambda Physik LEXtra KrF excimer laser using 20ns pules with a pulse repetiion rate of 3-12 Hz and a laser spot energy density of 1.05-1.20 J/cm^2. The $BiFeO_3$ targets were commercially purchased ceramic disks sintered from BiO and Fe_2O_3 powders, in some cases with a slight excess of BiO powder to account for the volatility of bismuth. The substrates were heated to 600-720 ˚C and the deposition was generally performed under an oxygen partial pressure of 100 mTorr.

4 Structural Characterization

Structural characterization is an essential first step when analyzing epitaxially grown thin films. It is important to determine whether the films are crystalline or not, and if so what phases are present in the film and what their crystallographic orientations are. Often, film growth and structural characterization are conducted iteratively, with the growth parameters such as substrate temperature or laser energy density being changed between each deposition to explore the parameter space and determine the conditions necessary for the desired results.

4.1 Structural Characterization Techniques

A variety of different structural characterization methods were utilized in this research. This section will serve as an overview of each of the major techniques, and in subsequent subsections the results from each and their significance will be presented.

4.1.1 X-Ray Diffraction

X-ray diffraction (XRD) is a commonly used experimental technique for probing the structural properties of thin films. It is widely used in materials science, and many classic books on the subject have been published – for a more detailed treatment of the technique and all of its uses the reader is encouraged to consult the references on it provided.[91-93] XRD involves the use of a single energy beam of x-rays to probe the atomic structure of a thin film sample. Because the x-ray wavelength is on the same order as the lattice spacing in the film, the diffracted reflections can be used to determine the film lattice parameters, its structural quality, and its orientation with respect to the underlying substrate. The basic modes of analysis can be categorized according to the axes the instrument is moved through with respect to the specimen. XRD can be used to accurately determine the out-of-plane lattice parameters of a thin film by aligning the instrument on a strong out-of-plane substrate peak (with perovskites, the 002 peak is typically used) and scanning through the θ–2θ axis. Scanning through the ω axis to obtain so-called “rocking curves” can be used to assess the degree of crystallinity of a film, while scanning through the ϕ axis and comparing the substrate and film spectra can allow one to determine the epitaxial alignment of the film with the underlying substrate.

Scanning in the θ–2θ and ω directions simultaneously allows one to construct a map of diffraction peaks in reciprocal space and determine both the in-plane (a and b axis) and out-of-plane (c axis) lattice parameters, as well as to determine any lattice distortion or strain state in the film. This is call a Q-scan or a reciprocal space map (RSM). As with θ–2θ scans, to obtain a reciprocal space map of a thin film careful alignment must first be done on a strong substrate peak. Because this is a 2-axis measurement, alignment must be done on a substrate peak with both in-plane and out-of-plane components. The 031 peak is commonly used because it typically has a relatively large structure factor in perovskites and is easily accessed within the geometric constraints of a four-circle diffractometer.

An x-ray diffractometer can also be used to accurately determine the thickness of a thin film on a substrate. When x-rays are incident on a thin film at very low angles (less than 1˚), they penetrate the film and reflect off the substrate surface and film surface multiple times. With each reflection inside the film, some fraction of the x-rays escape the surface of the film at different angles each time due to the additional path length traveled. Observation of these low angle reflections can indicate the thickness of the film – this technique is called x-ray reflectivity. In a similar way, diffracted x-ray beams can reflect multiple times within the film, which results in peak "fringes" around the strongest diffraction peaks in an x-ray diffraction spectrum. These are called Kiessig fringes, and can also be used to determine the thickness of a film.[94,95] Kiessig fringe intensity is given by the following equation:

$$I = I_0 \frac{\sin^2(N q_z c/2)}{\sin(q_z c/2)} \tag{22}$$

Where I_0 is the diffraction peak intensity, N is the number of Kiessig fringes, c is the lattice spacing of the film material and q_z is:

$$q_z = 4\pi \frac{sin\,\theta}{\lambda} \tag{23}$$

Where θ is the diffraction angle of the fringe peak and λ is the wavelength of the incident x-rays. Because c can be determined from the θ-2θ scans, N can be found using the above two equations. With this information the film thickness, t_{film}, can be determined:

$$t_{film} = c * N \tag{24}$$

In general, films need to be high quality and have very smooth surfaces and interfaces for these techniques to provide meaningful measurements. They also generally need to be less than ~100 nm thick. In this study, the measurement of film thickness is critical for the interpretation of some of the measured material responses. When film thicknesses are given, those with thicknesses less than 40 nm thick are generally estimated by the analysis of the Kiessig fringes in the x-ray diffraction spectra, and those with thicknesses between 40 and 100 nm are generally estimated via x-ray reflectivity. In thicker films, the thicknesses are estimated from growth rates determined from measured thicknesses of thinner films grown under the same deposition parameters.

Unless otherwise noted, the instrument used for XRD in this study was a PANalytical X'Pert Pro PW3040/60 system, which is a four-circle x-ray diffractometer that uses Cu Kα_1 monochromated radiation.

4.1.2 Atomic Force Microscopy

Atomic Force Microscopy (AFM) is a form scanning probe microscopy used to determine topographical features on the surface of thin film samples. This is done by performing a raster scan on the sample surface with an atomically sharp silicon cantilever, which reflects a laser beam from its surface to a four-quadrant photodetector. A schematic illustrating the basic AFM setup is shown in **Figure 9**.

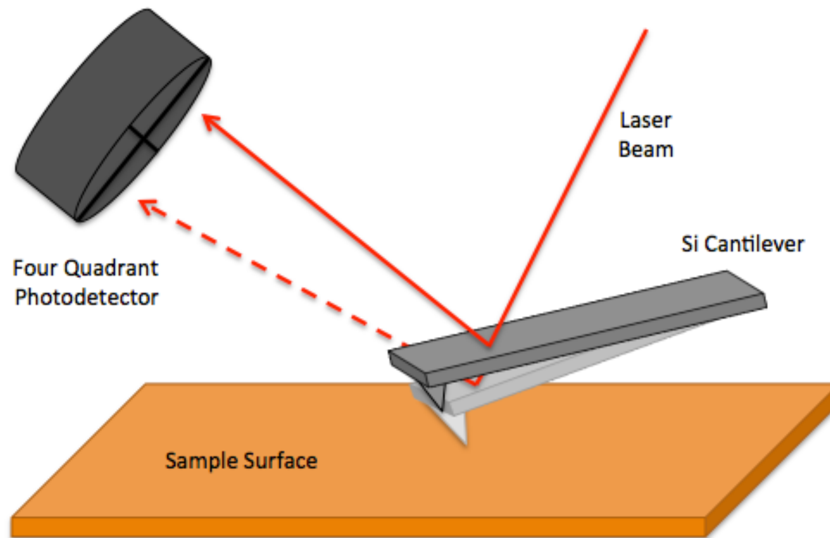

Figure 9. Schematic of an atomic force microscope. The cantilever with the atomically sharp Si tip is kept at a static height above the sample surface and oscillated at its resonant frequency. Electrostatic interactions between the tip and the sample cause the cantilever to bend, which changes the location of the laser spot reflected on to a four-quadrant photodetector. The acquired signal can be converted into a topological map of the sample surface.

In tapping mode, as used in this study, the cantilever is kept at a static height above the surface while it is oscillated at its resonant frequency (typically in the range of 200-400 kHz) via an actuator. Any electrostatic interactions between the tip and the sample surface will cause the cantilever to bend, which in turn changes the position of the laser spot on a four-quadrant photodetector. The difference in signal for each quadrant can be calibrated with a standardized step grating to provide accuracy to within one angstrom. The data gathered from this technique can then be converted into a topological map of the sample surface.

4.1.3 Transmission Electron Microscopy

Transmission electron microscopy (TEM) facilitates the transmission and interaction of a beam of electrons through a thin sample to provide information about its structure and composition. Electrons are suitable for this purpose because they are charged, which allows them to be accelerated and directed via electromagnetic fields and used to probe the chemical nature of materials. Electrons also have a small wavelength ($\lambda \sim 4$ pm at 100 keV acceleration), which allows for very high resolution. State of the art TEM can now resolve down to sub-angstroms.[96] Standard imaging in TEM is via bright-field mode, where the aperture is oriented to collect the electrons that are transmitted through the sample. This produces an image with contrast resulting directly from the intensity of the transmitted electron beam. Thus, areas within a sample that produce high electron scattering as a result of a higher density or heavier atoms tends to appear darker than areas that scatter less. Aside from bright-field imaging, other useful TEM techniques include dark-field imaging, selected area diffraction (SAD), convergent beam electron diffraction (CBED), energy-dispersive spectroscopy (EDS), electron energy loss spectroscopy (EELS), scanning transmission electron microscopy (STEM), high-resolution (or phase-contrast) imaging, and high-angle annular dark-field imaging (HAADF) which is also called Z-contrast imaging. In addition to bright field imaging used in this study, SAD is used to probe the crystal structure in localized areas of thin films. This is done by carefully placing a selected area aperture below the sample in the TEM column such that the diffraction pattern seen is only generated from the area of the sample not blocked by the aperture. HAADF is also used in scanning mode to obtain high-resolution atomic scale images of BFO thin films and crystallographic interfaces within them. These images are formed via the collection of high-angle incoherently scattered electrons from around the main beam using an annular dark field detector. The technique is very sensitive to atomic number and this is the origin of contrast in the resulting images.

The techniques available to a materials scientist using a TEM are numerous and detailed, and the field is broad and complex enough to produce dissertations solely focused on one aspect of it. For the purpose of this study, the detail given will be high level and focused on the techniques used to produce the data herein, namely SAD and HAADF. For more information about the techniques described above, classic graduate level textbook references are given.[97-99] In this study, the instruments used for low magnification bright field imaging and electron diffraction were a JEOL 200CX operating at 200keV and a JEOL 3010 operating at 300 keV. *In* situ nanoprobe experiments were conducted using a JEOL 3010 equipped with a Hysitron nanoscale electrical contact resistance (nanoECR) picoindenter system with a radius of curvature of ~150 nm. The instrument used for high-angle annular dark-field microscopy was the aberration-corrected TEAM 0.5 microscope (a modified FEI Titan 80-300) operated at 300 kV.[100] The TEAM 0.5 at the National Center for Electron Microscopy (NCEM) is one of the most powerful electron microscopes made and is capable of sub-angstrom resolution via highly stable electronics, state of the art aberration correction insertion devices and a very bright electron source.

4.1.4 Optical Second Harmonic Generation

Optical Second Harmonic Generation (SHG) is a volumetric probing technique for characterizing nonlinear media, such as ferroelectric materials. In SHG, a beam of coherent light of frequency ω is incident on the material being analyzed and is converted into an optical signal of frequency 2ω through the creation of a nonlinear polarization:

$$P_i^{2\omega} \propto d_{ijk} E_j^{\omega} E_k^{\omega} \tag{25}$$

where E^{ω} is the incident electric field and d_{ijk} is the nonlinear optical coefficient of the medium.[101,102] In using SHG to study thin films on a substrate, the experiment is typically performed in transmission mode in which a beam of polarized light is incident on the film side of the sample. As illustrated in **Figure 10**, coherent polarized light with frequency ω is produced by a tunable pulsed laser and its polarization direction is continuously rotated through an angle ϕ via a half-wave plate. This beam is then incident on the surface of the film at an adjustable angle θ with respect to the surface normal.

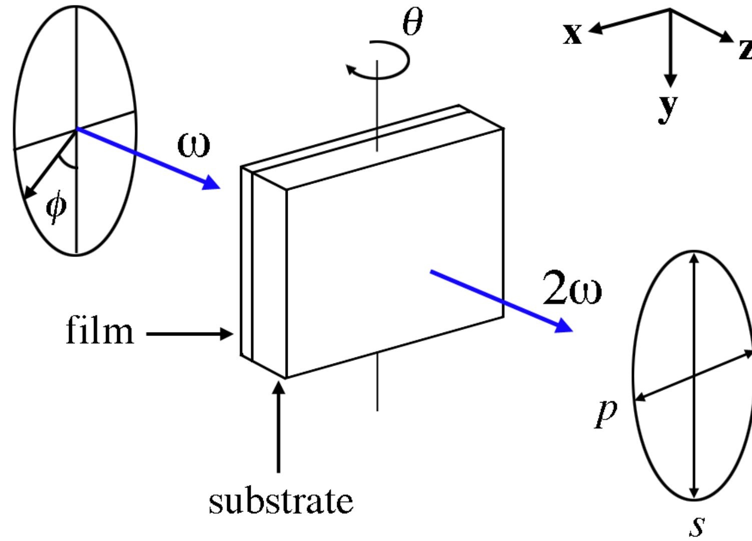

Figure 10. Schematic showing the experimental setup for optical second harmonic generation (SHG). Polarized light with frequency ω is produced by a tunable pulsed laser and its polarization direction is continuously rotated through an angle ϕ via a half-wave plate. This beam is then incident on the surface of the film at an adjustable angle θ with respect to the surface normal. The intensity of the frequency doubled output signal from the film is detected within the *sp* plane as a function of the angle of incidence θ and the polarization angle ϕ of the incident light, and compared to the expected intensity expressions for the film based on an assumed symmetry.

If a pseudocubic (001) oriented substrate is assumed, $y = s$ and $x = p$. The intensity of the output signal from the film is detected within the *sp* plane as a function of the angle of

incidence θ and the polarization angle ϕ of the incident light, and compared to the expected intensity expressions for the film based on an assumed symmetry. For example, the expressions for the SHG intensity for *s* and *p* output polarizations pertaining to a sample with *4mm* symmetry are:[103]

$$I_s^{2\omega} = K_1^2 \sin^2 2\phi \tag{26}$$

$$I_p^{2\omega} = (K_2 \cos^2 \phi + K_3 \sin^2 \phi)^2 \tag{27}$$

In these equations the coefficients K_1, K_2, and K_3 are functions of the incident intensity of the beam I_0, the nonlinear coefficients d_{ij}, the incidence angle θ, and various Fresnel coefficients for the system.[104]

In expressions for the SHG intensity for *s* and *p* output polarizations pertaining to samples with higher symmetries, such as *3m*, the equations become more complex.[103] For the purposes of this study, optical SHG is used to detect the presence of different ferroelectric phases with spontaneous polarizations in different directions relative to the incident beam and in this way distinguish between different ferroelectric phases in the same film. For a more extensive review on probing ferroelectrics using SHG, the reader is referred to reference provided.[105]

4.2 Evidence for a Phase Transition

4.2.1 XRD θ–2θ Scans

Representative θ–2θ scans from thin BFO films grown on DSO(110), STO(001), LSAT(001), LAO(001) and YAO(110) can be seen in **Figure 11**. These scans were aligned on the substrate pseudocubic 002 peaks, and the spectra include the 002 peaks for the BFO films and all the various substrates.

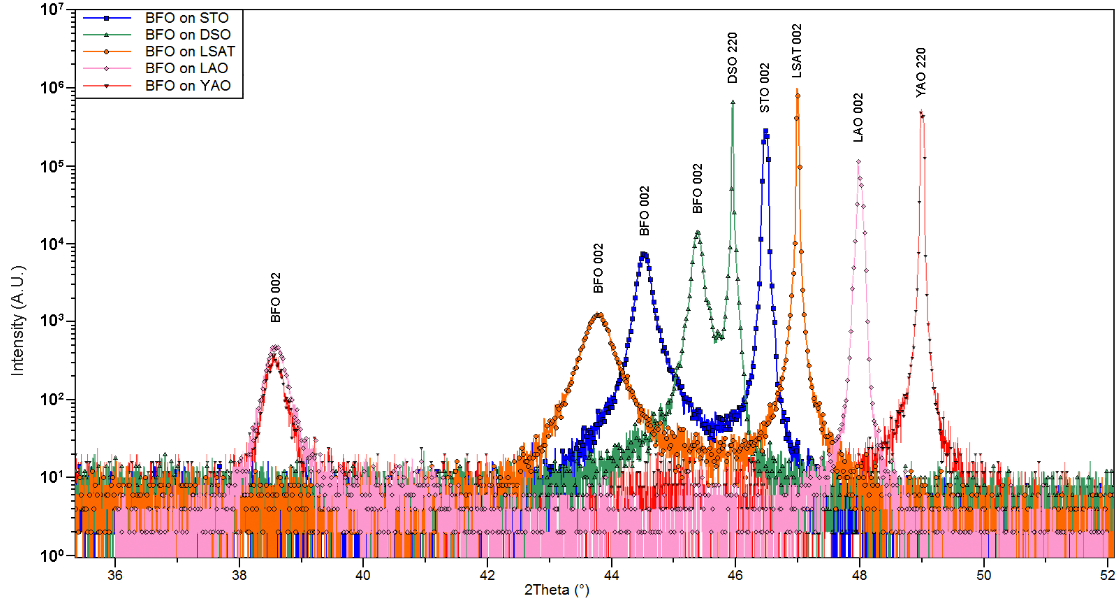

Figure 11. X-ray diffration spectra from (001) oriented BFO films grown on DSO(110), STO(001), LSAT(001), LAO(001) and YAO(110). These spectra show the 002 and 220 peaks of the various substrates and the 002 peaks of the BFO films grown on them. All direction given are pseudocubic except those given for DSO and YAO, which are are orthorhombic (110) which is equivalent to pseudocubic (001).

From these spectra, the *c*-axis (out of plane) lattice parameter for the films can be determined directly. If one further assumes that the films are epitaxial with the substrate and thin enough such that minimal relaxation of the film has occurred, then one can also estimate the film's *a*-axis (in plane) lattice parameter and subsequently estimate the *c*/*a* ratio and the unit cell volume of the film. The results from this analysis are tabulated in **Table 2** and represented graphically in **Figure 12**, which shows the evolution of the structural parameters of the films under increasing compressive strain.

Substrate	Substrate *a* (Å)	Film *c* (Å)	Film *c*/*a*	Film Unit Cell Volume (Å^3)
$YAlO_3$(110)	3.681	4.667	1.268	63.24
$LaAlO_3$(001)	3.793	4.648	1.225	66.87
LSAT(001)	3.864	4.126	1.068	61.60
$SrTiO_3$(001)	3.905	4.064	1.041	61.97
$DyScO_3$(110)	3.951	3.998	1.012	62.41

Table 2. Structural data extracted from XRD data on BFO films grown on various substrates. The *c*-axis lattice parameters were measured directly and the *c*/*a* ratios and unit cell volumes were based on fully epitaxial films adopting the substrate in-plane lattice parameter.

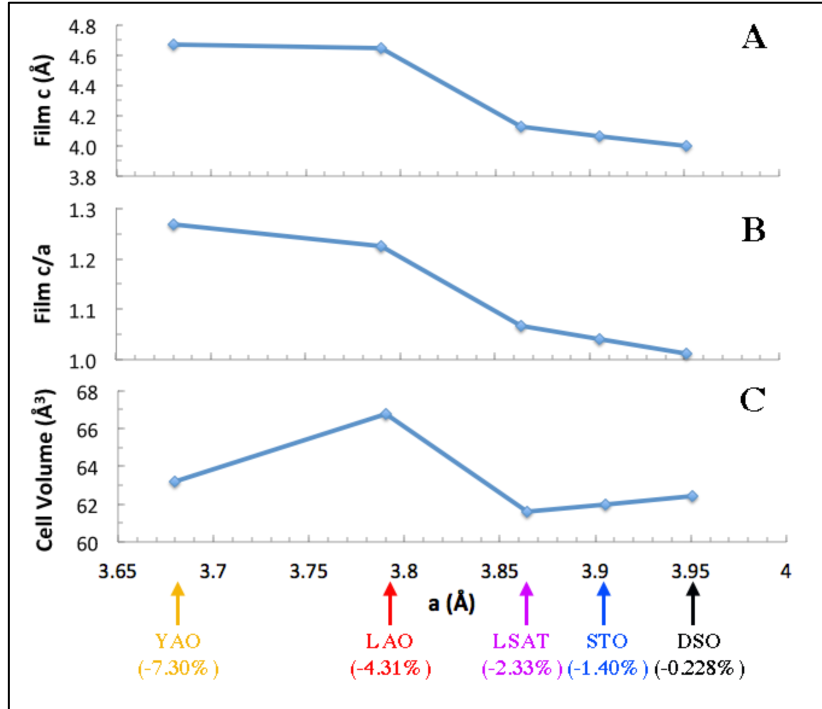

Figure 12. Evolution of the structural parameters of BFO films grown on various substrates inducing increasing compressive strain, including the film *c*-axis lattice parameter **(A)**, the film *c*/*a* ratio assuming an unrelaxed film **(B)**, and the film unit cell volume **(C)**. There appears to be discontinuity in the change in unit cell volume between the films grown on LSAT and the films grown on LAO, suggestive of a phase transition somewhere between these two strains.

There appears to be a discontinuity in the unit cell volume between the films grown on LSAT and the films grown on LAO, suggestive of a phase transition somewhere between these two strains. The in-plane data tabulated in **Table 2** and graphically shown in **Figure 12** constitute estimates, and it should be considered that the film's in-plane lattice parameter may not exactly match that of the substrate due to relaxation through the thickness of the film.

To ensure the films were single phase with no secondary phases present, complete θ–2θ scans were also recorded. Representative scans from a 25 nm thick BFO film grown on LAO(001), showing the 001, 002 and 003 peaks for the film and substrate (marked with an asterisk) can be seen in **Figure 13**.

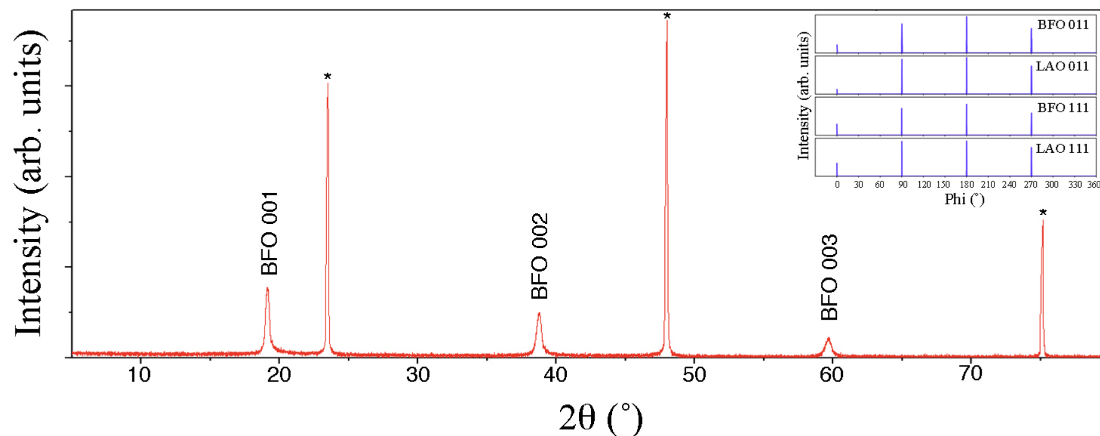

Figure 13. Complete XRD theta scan of a 25nm thick BFO film grown on a (001) oriented LAO substrate. The 001, 002 and 003 peaks of the BFO film are labeled. The corresponding substrate peaks are marked with *. There are no other peaks in the spectra, indicating a single phase film with no secondary phases. The inset shows 360° ϕ scans of the 011 and 111 peaks for the film and substrate, demonstrating the epitaxial relationship between the film and substrate.

The inset of **Figure 13** shows ϕ scans for the 011 and 111 peaks of the film and substrate, verifying the epitaxial relationship between the BFO film and the LAO substrate as $[100]_f$ // $[100]_s$ and $[010]_f$// $[010]_s$, where the subscripts *f* and *s* refer to the film and substrate, respectively.

From these diffraction results, it appears that a single phase film with an out-of-plane lattice parameter of ~4.64 Å has been stabilized on LAO(001) substrates. This is quite close to the theoretical *c*-axis lattice parameter reported for the tetragonal phase of BFO.[106,107]

4.2.2 Reciprocal Space Mapping

Reciprocal space maps taken around the 103 family of peaks for the film and substrate were made in order to better determine the film lattice parameters and the orientation of the crystal lattices with respect to each other. A representative RSM obtained from a 25 nm thick BFO film on LAO is shown in **Figure 14(A)**. This is a composite reciprocal space map image with the y axis truncated for visible clarity, as the film and substrate peaks are far from each other in reciprocal space due to the large difference between their c-axis lattice parameters. The substrate peaks are very intense with respect to the film peaks, and the film peaks in this composite image were collected over a much longer duration than the substrate.

From an analysis of the RSM in **Figure 14(A)**, the slight difference of the in-plane lattice parameters of the LAO substrate is evident from the peak splitting into separate 103 and

013 components. This same splitting is observed in the film peak, indicating that the two in-plane lattice parameters of the film are also not quite equal. In addition, the 103 component of the film peak splits along the Q_y axis into -103 and 103 components, indicating a slight monoclinic distortion of the film unit cell in the direction of the a axis. The 103 and 013 peaks for the film do not line up exactly with those of the substrate along the Q_x axis, which is an indication that the in-plane lattice parameters are slightly larger and the film is already relaxing at this thickness.

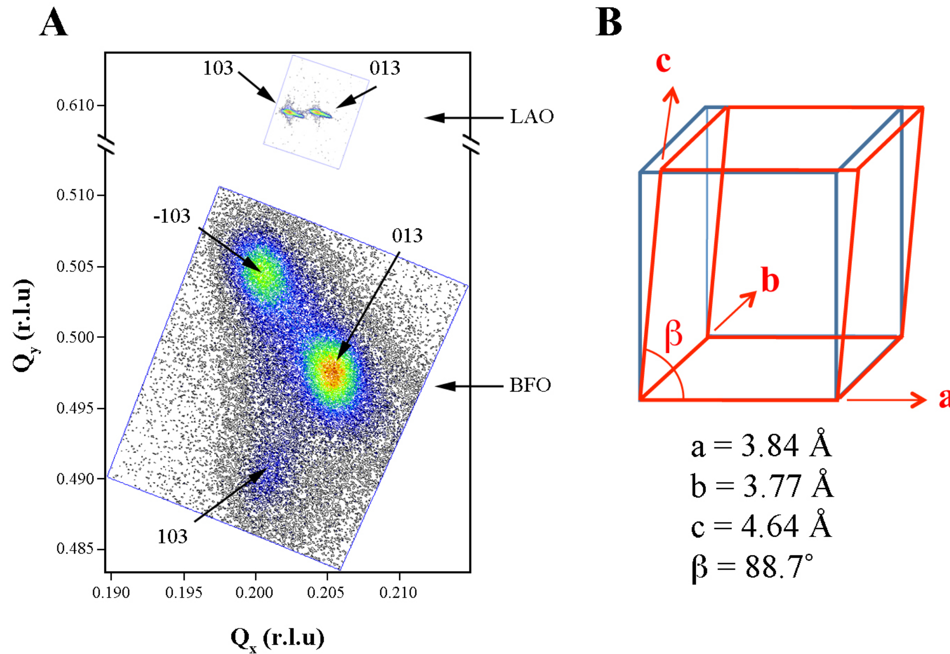

Figure 14. **(A)** Composite reciprocal space map showing the 013 family of peaks for the LAO substrate and for the 25 nm thick BFO film grown on it. The separation of the substrate 103 and 013 peaks is due to the *a* and *b* lattice parameters having slightly different values. The BFO film shows a similar separation of the 103 and 013 peaks, as well as a separation of the -103 and 103 peaks, suggesting a monoclinically distorted unit cell with an angle $\beta < 90^\circ$ between the c and a lattice vectors. **(B)** Schematic of the proposed unit cell structure for this film based on the reciprocal space map shown in **(A)**.

From the reciprocal space map obtained, it is clear this film does not have the rhombohedral symmetry associated with bulk BFO or the distorted rhombohedral symmetry associated with BFO films grown on substrates that impose less compressive strain. Instead, a monoclinically distorted tetragonal phase is suggested as a simple model to work with as shown in **Figure 14(B)**. With a c axis of ~4.64 Å and a *c*/*a* ratio of ~1.23, this is very similar to the theoretically predicted tetragonal phase detailed in Section 2.5.2. Because this phase appears to be tetragonal-like in structure but is slightly monoclinically distorted, and because the actual symmetry is not known, it will be referred to in this study as the T-phase, while monoclinically distorted rhombohedral BFO films will be referred to as the R-phase.

4.3 Mixed Phase Films

If the T-phase present in XRD spectra is an indication of a phase boundary between it and the ground state rhombohedral phase along the strain axis, it is possible that at some lower amount of induced strain this new phase will become energetically degenerate with the rhombohedral phase. As discussed previously, films under tensile or compressive strain will relax with increasing thickness. Thus, if the film is strained to be near the morphotropic phase boundary on the tetragonal side, thickness relaxation is an easy tool to explore the effects of different strain states in the films grown on LAO. To test this experimentally, a thickness series of BFO films was grown on (001) oriented LAO substrates in order to explore the effects of strain relaxation on the stability of the newly discovered T-phase. For this study, a series of films were grown between 5 nm and 200 nm thick under the same conditions detailed above, and these films were structurally characterized via atomic force microscopy (AFM), x-ray diffraction (XRD) and optical second harmonic generation spectroscopy (SHG). Furthermore, select films were characterized via electron diffraction and scanning tunneling electron microscopy.

4.3.1 Surface Topography of Mixed Phase Films

In AFM scans on the thinnest films, as shown in **Figure 15 (A)** illustrating a scan of a 9 nm thick film, the surface topography appears to be smooth with atomic level terraces and step-heights of ~4.64 Å, corresponding to single unit cell steps of the T-phase. In scans on thicker films, such as the 120 nm thick film shown in **Figure 15 (B)**, a stripe-like morphology has developed, something unseen before in BFO films but reminiscent of the morphology of PZT films with near-MPB composition having mixed tetragonal and rhombohedral phases.[108-110]

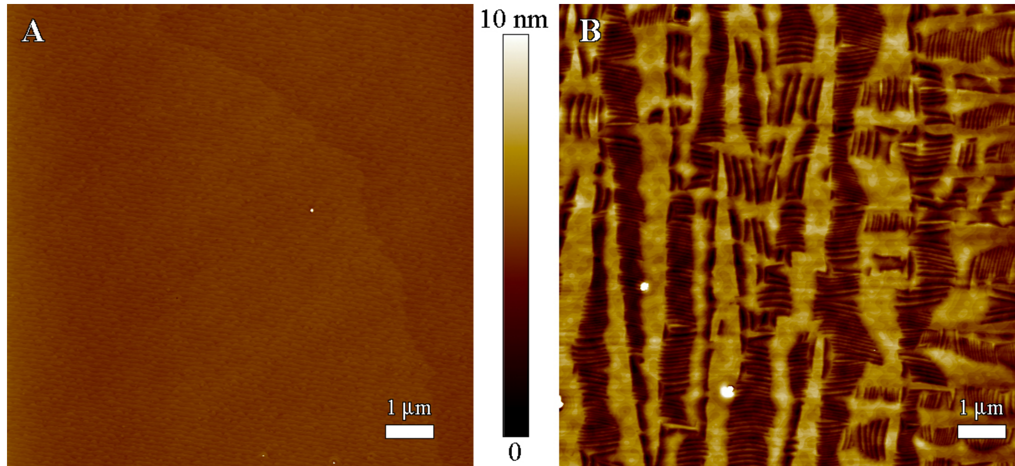

Figure 15. **(A)** a 9 nm thick BFO film on LAO, showing a smooth topography with unit cell step heights. **(B)** a 120 nm this BFO film on LAO, showing a dark (lower height) stripe-like morphology in a lighter colored (higher) field.

In **Figure 15 (B)**, the stripes appear dark in the scan, indicating a lower height than that of the surrounding lighter colored material. These dark colored (lower) stripes will later be shown to be R-phase regions emergent in a lighter colored (higher) T-phase matrix. A close up of one of the stripe-like domains from an AFM scan of a 50 nm thick film along with the results of a line-trace perpendicular to the stripes can be seen in **Figure 16**.[111]

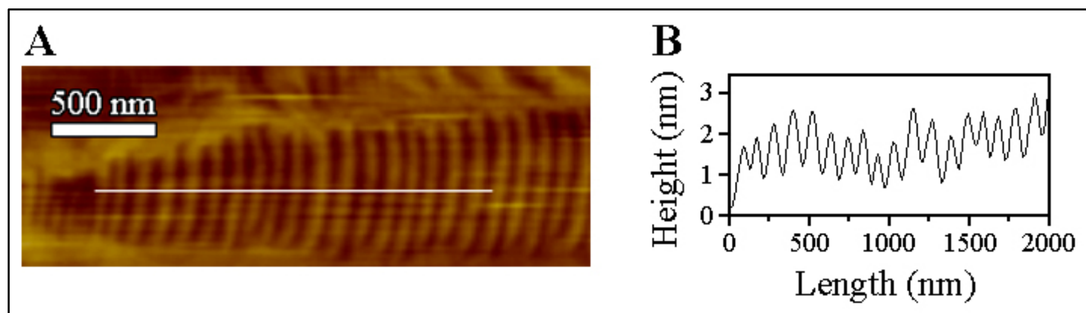

Figure 16. **(A)** Close-up AFM scan of one of the striped domains from a ~80 nm thick BFO film grown on LAO with a horizontal line indicating where the line profile in **(B)** was measured. The relative height differences between the dark and light areas can be seen to have a peak-to-valley height difference of 1-2 nm. The spacing of the stripes is measured to be approximately 40-50 nm.

The image in **Figure 16(A)** shows a close-up AFM scan of one of the striped domains from a ~80 nm thick BFO film grown on LAO, with a horizontal line indicating where the line profile in **Figure 16(B)** was measured. The relative height differences between the dark and light areas can be seen to have a peak-to-valley height difference of 1-2 nm. The spacing of the stripes is measured to be approximately 40-50 nm.

A complete set of scans for a representative thickness series of BFO films grown on LAO substrates is shown in **Figure 17**.[111] In this figure, it can be seen that the striped morphology evolves with thickness; the stripes are non-existent in the thinnest film, appear very small in the next thickest film and grow progressively larger as the films get thicker.

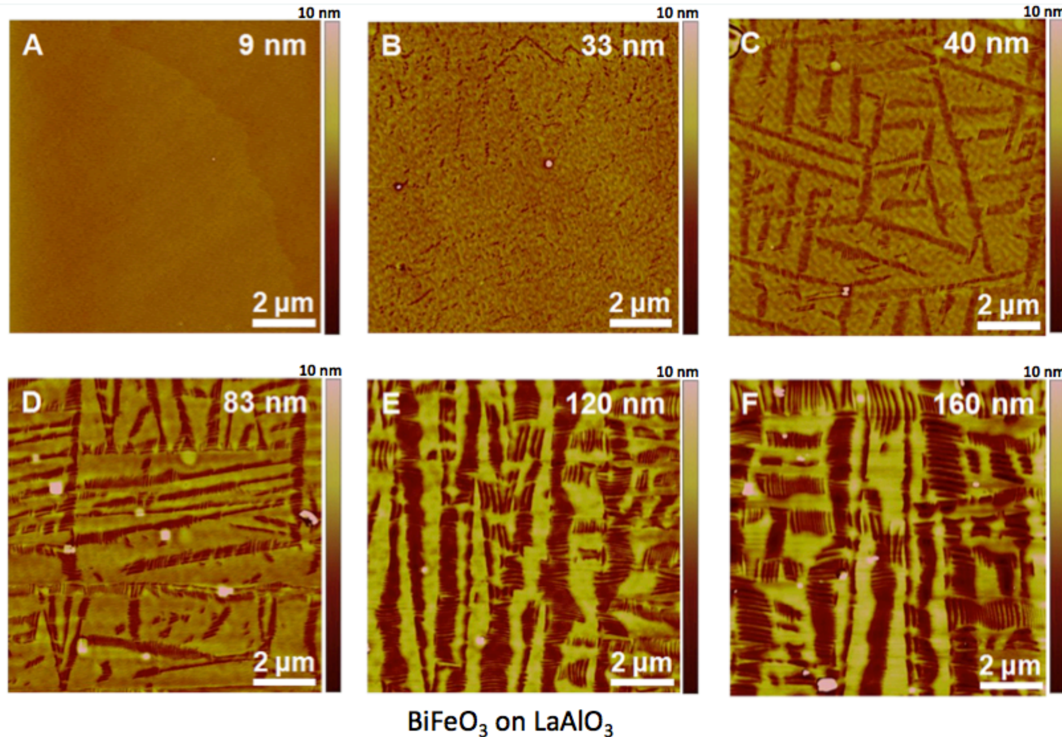

Figure 17. AFM scans of a thickness series of BFO films grown on (001) oriented LAO substrates. The films get progressively thicker from **(A)** through **(F)**, with the thicknesses indicated. The stripe-like morphology evolves with increasing thickness, indicating that the stripes are energetically more favorable in the reduced strain state of the thicker films, consistent with the hypothesis that the darker (lower) stripes are a separate emergent phase from the lighter (higher) matrix phase.

This suggests that the dark stripes in the films evolve as a function of decreased strain through the volume of the film, consistent with the hypothesis that they are a separate phase that is energetically more favorable at the lower strain states present at the surface of thicker films. This is consistent with the hypothesis that the R-phase (darker/lower) is emerging in the highly strained T-phase (lighter/higher) films as film thickness increases, i.e. as the strain state is reduced through the volume of the films.

4.3.2 X-Ray Diffraction Results on a Film Thickness Series

To compliment the AFM scans of the thickness series of films shown in **Figure 17**, XRD spectra were obtained for each of these films to demonstrate that the T-phase is dominant

in the thinnest films and the R-phase coexists with it in thicker films. The results are depicted in **Figure 18**.

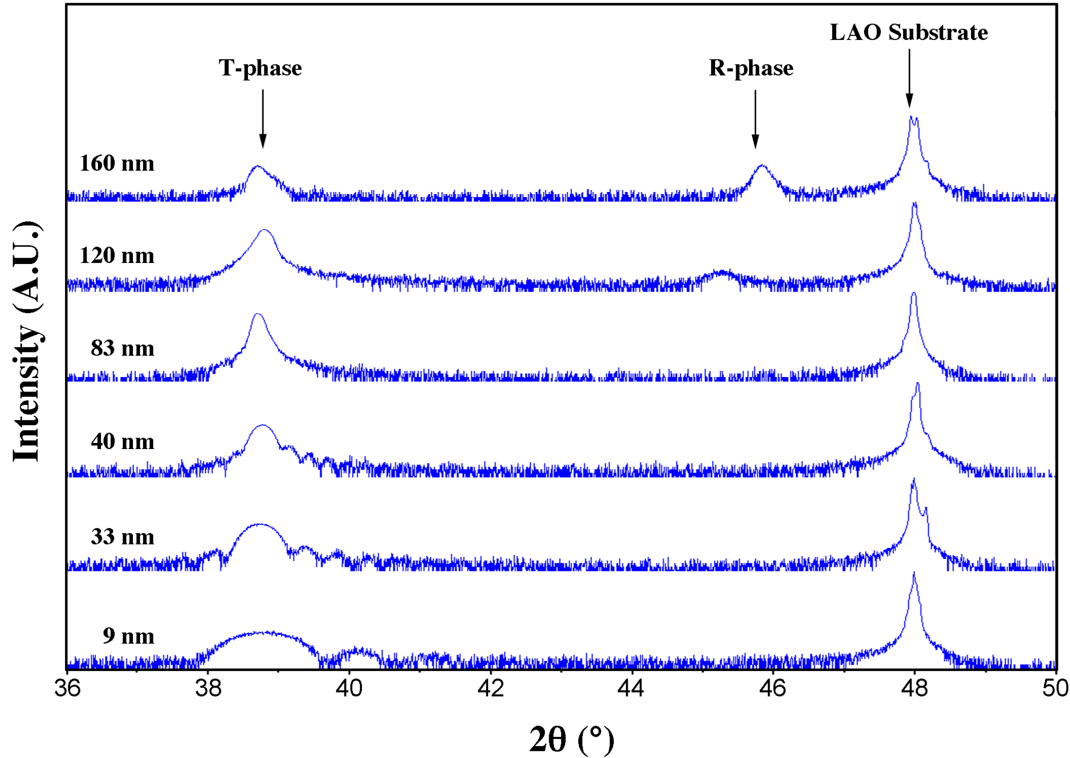

Figure 18. XRD θ-2θ scans of a thickness series of BFO films grown on LAO substrates, showing the 002 peaks of the T-phases and R-phases in the films and the 002 peaks of the substrate. The film thicknesses are, from bottom to top, 9 nm, 33 nm, 40 nm, 83 nm, 120 nm and 160 nm. The Kiesseg fringes can be clearly seen surrounding the film peak in the three thinnest films. The variation in quality of the substrates with respect to twinning in LAO can be seen in the substrate peaks, and are also reflected in the asymmetry of the film peaks.

In the series of diffraction spectra shown in **Figure 18**, showing the 002 diffraction peaks for the substrates and BFO films, the four thinner films show evidence of only the highly strained T-phase in their spectra. (The Kiesseg fringes can also be clearly seen in the three thinnest films). The peaks corresponding to the R-phase begin to appear in the spectra of the 120 nm and 160 nm thick films, consistent with the hypothesis that the strain relaxation in the thicker films gradually lowers the energy of the R-phase with respect to the T-phase until they are energetically degenerate. It is an interesting observation that the variation in quality of the LAO substrates, which form twins in their surface structure below ~530 ˚C, can be seen in some of the substrate peaks which in turn affects the asymmetry of some of the film peaks.[112]

4.3.3 SHG Results from a Film Thickness Series

Optical second harmonic generation (SHG) was used to structurally differentiate the phases in the BFO films grown on LAO.[111,113] LAO substrates are ideal for studying films with SHG because LAO is centrosymmetric, with point group $\bar{3}m$, and thus does not generate any SHG signal. A Ti-sapphire laser was employed to provide 100 fs pulses of 800 nm wavelength coherent light at a 1 kHz repetition rate for SHG studies in transmission geometry. (A schematic of the experimental setup is illustrated in **Figure 10**). For the purposes of the analysis, the T-phase was assumed to have *4mm* symmetry while the R-phase was assumed to have the *3m* symmetry of bulk-like BFO. In making these assumptions, the two symmetry components can be neatly separated from each other in the SHG experiment by changing the incidence angle of the beam and the location of the signal detectors. For the T-phase, which has a predominantly *c*-axis oriented polarization, no signal should be generated when the film normal is coincident with the incident fundamental beam ($\theta = 0°$), hence all signal in this geometry should be from the R-phase. Conversely, when $\theta = 45°$, the T-phase should dominate the generated *p*-polarized SHG signal. The results of the SHG analysis on a thickness series of three films are shown in **Figure 19**.

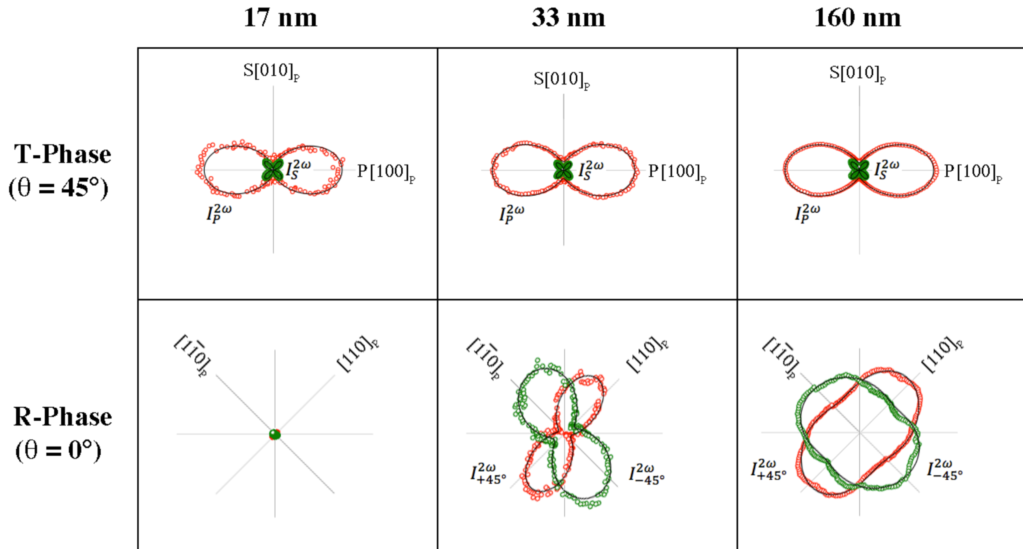

Figure 19. SHG signal obtained in tilted (top plots, $\theta = 45°$) and normal (bottom plots, $\theta = 0°$) incidence configurations for three thicknesses of BFO/LAO films (17 nm, 33 nm and 160 nm), with the output analyzer along *S* (green) and *P* (red) polarizations, and along 45° (red) and -45° (green) relative to the pseudocubic axes, respectively. The 17 nm films are dominated by SHG signal from the T-phase ($\theta = 45°$) while in thicker films the SHG signal from the R-phase ($\theta = 0°$) increases with thickness, consistent with AFM and XRD results. Solid black lines are theory fits for T-phase and R-phase, accounting for different domain variants in the R-phase.

For the thinnest of the three films (t = 17 nm), which are assumed to be almost purely T-phase, when the beam is at normal incidence ($\theta = 0°$) there is no SHG signal generated

by the film but there is signal when the beam is incident at an angle of θ = 45°, in agreement with AFM and XRD results suggesting that the thinnest films consist of predominantly T-phase and little-to-no R-phase. For thicker films, (t = 33 nm, t = 160 nm), which are assumed to be progressively more mixed phase, when the beam is at a 0° incidence, the films generate progressively more signal with thickness, which is also in agreement with AFM and XRD results suggesting a progressively increasing volume fraction of R-phase in a T-phase matrix.

4.3.4 TEM Results From Mixed Phase Films

To structurally characterize the mixed phase films with greater detail, transmission electron microscopy (TEM) was utilized to obtain low-resolution bright field images of the striped regions and to obtain selected area diffraction patterns from the individual stripes in these regions to assist in determining their crystal structure. Scanning TEM (STEM) was used to obtain z-contrast images of the striped domains and of the crystallographic interface between them.

Samples for TEM analysis were prepared in cross-sectional geometry. They were cut parallel to the (100) pseudocubic planes of the LAO substrate, and subsequently mechanically ground to a thickness of ~20 μm, followed by a liquid nitrogen-cooled ion milling process under grazing incidence until the samples were thin enough for electron transparency. Sample preparation proved to be difficult with these films as a result of the high strains imparted on the films by the substrate. Thinning the films to make them electron transparent in plan-view proved to be impossible as the samples simply curled up as the film relaxed without the underlying constraint of the substrate. As a result, only cross-sectional analysis was possible. However, even within these constraints a significant amount of useful information was obtained using these techniques.

4.3.4.1 Bright field imaging

A low magnification bright field cross-sectional image of a striped region in a ~80 nm thick BFO film on LAO is shown in **Figure 20** below. The T-phase and R-phase appear as light and dark bands due to residual coherent diffraction contrast and are labeled in the image. The scale of the striped region is consistent with the previously discussed AFM images (see **Figure 16**) with the spacing of the stripes measured to be ~40-50 nm. The wedge shape of the two different regions is consistent with the hypothesis that the R-phase is energetically favorable at lower strains, as the strain field is reduce through the thickness of the film away from the substrate as the film relaxes.

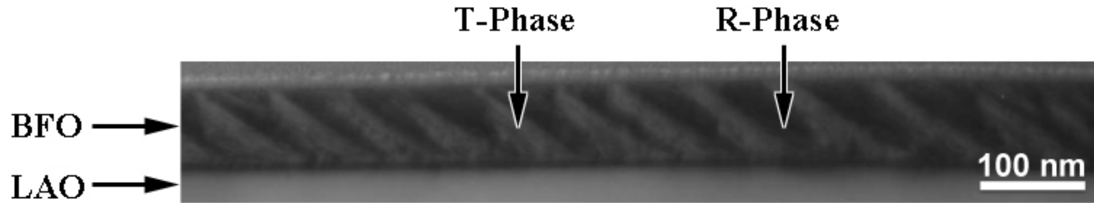

Figure 20. Bright field TEM image of a cross-sectional of area of mixed a phase region in a ~80 nm thick BFO film grown on LAO. The T-phase appears bright in this image and the R-phase appears dark. Note the wedge shapes of the two phases within the cross-section of the film, consistent with the decreasing compressive strain up through the volume of the film, favoring the T-phase near the substrate and the R-phase near the film surface.

4.3.4.2 Selected Area Electron Diffraction

Selected area electron diffraction (SAD) patterns were taken from the bright field image of a striped domain region shown in **Figure 20**, one from each kind of domain. The indexed electron diffraction patterns, with the reciprocal unit cells shown, can be seen in **Figure 21**.

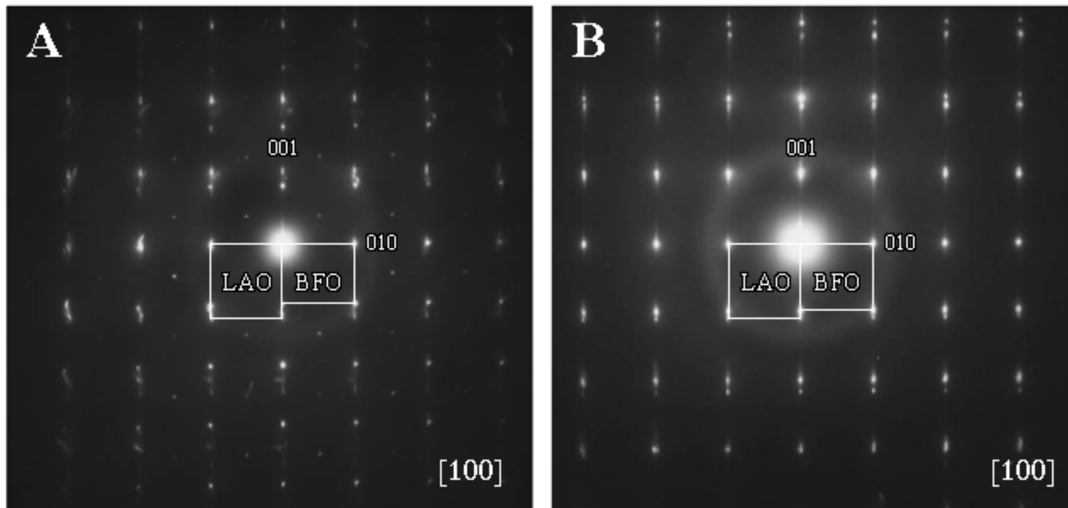

Figure 21. Selected area diffraction patterns taken from the striped domain shown in the bright field image of **Figure 20**. Each shows a superposition of patterns from the substrate and film, with the unit cells from each outlined and labeled. The zone axis for each is 100, and the 001 and 010 diffraction spots are indexed. **(A)** is taken from the lighter colored region of **Figure 20** corresponding to the T-phase. Measurements from this pattern give an out-of-plane lattice parameter of ~4.65 Å, an in-plane lattice parameter of ~3.7 Å, and an angle of ~89˚ between the two axes. **(B)** is taken from the darker colored region of **Figure 20** corresponding to the R-phase. Measurements from this pattern give an out of plane lattice parameter of ~4.07Å, an in-plane lattice parameter of ~3.8 Å, and an angle of ~89.5˚ between the two axes.

The results in **Figure 21** corroborate that the two domains are distinct structural phases with different in-plane and out-of-plane lattice parameters. Although the lattice parameters obtained with this technique should be considered approximations considering the films may be slightly relaxed due to the thinning of the sample for analysis, the results are quite consistent with those obtained via x-ray diffraction experiments. The lighter areas of the bright field image in **Figure 20** have a measured *c*-axis lattice parameter of ~4.65 Å and an in-plane lattice parameter of ~3.7 Å, which is consistent with the x-ray diffraction analysis shown in **Figure 11**, **Figure 12**, **Figure 13** and **Figure 14**. The measured in-plane lattice parameter is also consistent with an assumed epitaxial relationship with the underlying LAO substrate. The darker areas of **Figure 20** have a *c*-axis lattice parameter of ~4.07 Å, which is consistent with the x-ray diffraction analysis of the emergent R-phase shown in **Figure 18**, and an in-plane lattice parameter of ~3.8 Å, which is also consistent with an epitaxial relationship with the underlying LAO substrate. For both phases, the in-plane and out-of-plane axes are not orthogonal; an angle of ~89.5° between the two axes was measured for the R-phase and an angle of ~89° was measured for the T-phase.

4.3.4.3 Z-contrast Imaging

In order to examine more closely the structure of the mixed phase films and the phases present in the striped morphology, and to gain a better understanding of the interface between the two phases, Z-contrast images were obtained along the [010] perovskite pseudocubic direction. A typical image of an area of film containing a T-phase region interspersed between two R-phase regions is shown in **Figure 22**.

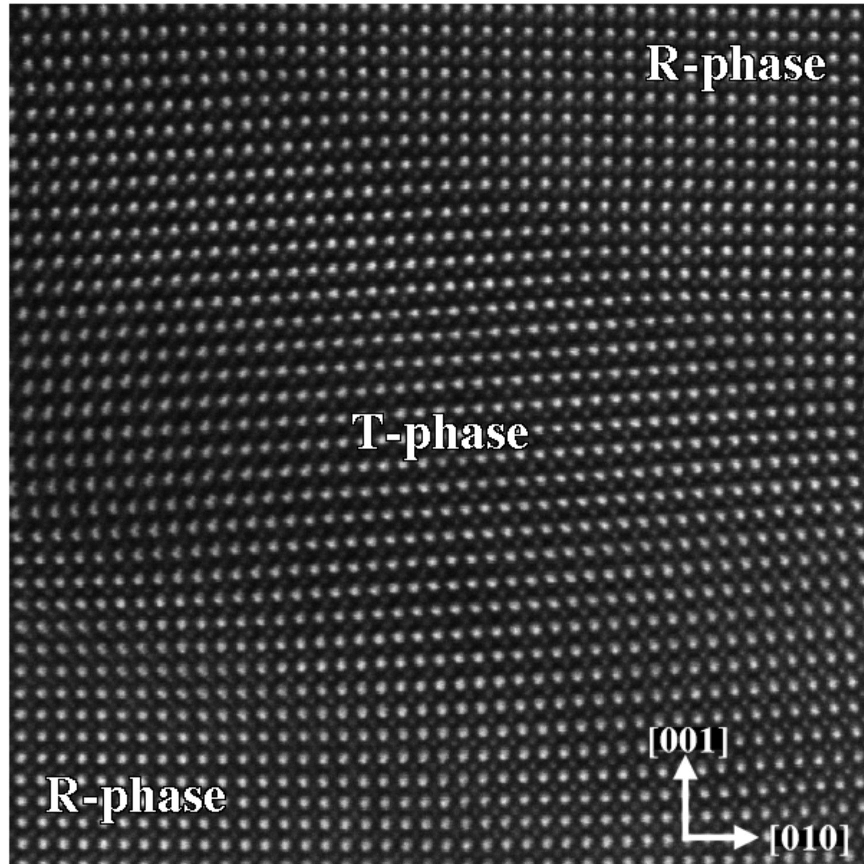

Figure 22. Close up HAADF-STEM images of T-phase region flanked by two R-phase regions. The columns of the much heavier Bi atoms show up as brightly colored spots, while the lighter columns of Fe atoms show up as the smaller, darker spots. The interfaces between the phases appear to be coherent with smooth, defect-free transitions and no apparent stacking faults or dislocations present along the boundaries. The transition and its associated abrupt change in unit call volume appear to be accommodated purely by strain effects.

In these images, the crystallographic columns have two distinct intensities: the columns of the much heavier Bi atoms show up as brightly colored spots, while the lighter columns of Fe atoms show up as the smaller, darker spots. The interfaces between the phases appear to be coherent with smooth, defect-free transitions and no apparent stacking faults or dislocations present along the grain boundaries. The transition and its associated abrupt change in unit cell volume appear be accommodated purely by strain effects.

By carefully measuring the interatomic distances between the columns of atoms in the Z-contrast image, a close analysis of the transition along two rows of atomic columns in the center of the domain wall, shown in **Figure 23**, reveals that the structure changes smoothly from the R-phase to the T-phase over a distance of ~10 unit cells.

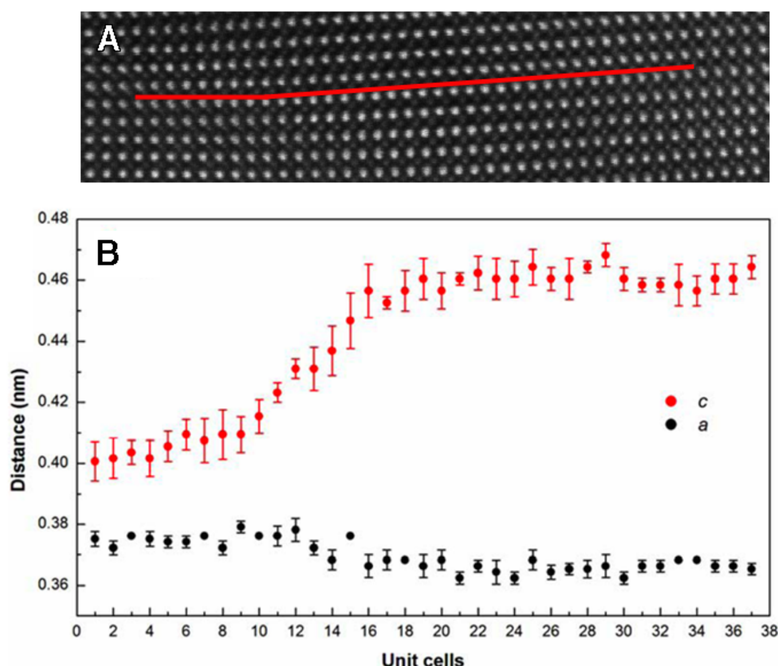

Figure 23. The estimations of in-plane and out-of-plane lattice parameter evolution along a linear row of unit cells through an interface between R-phase and T-phase domains. A close-up Z-contrast image of a phase boundary between a section of R-phase and T-phase is shown in **(A)** along with a line superimposed indicating where the measurements in **(B)** were taken. The *c*/*a* ratio appears to go from 1.07 to 1.27 in approximately ten unit cells with the *c*-axis parameter dramatically changing over this distance.

In **Figure 23(A)** a close-up of a Z-contrast image of a phase boundary between the R-phase (left) and T-phase (right) is shown along with a line superimposed indicating where the measurements in **Figure 23(B)** were taken.[111] The *c*/*a* ratio changes from 1.07 for the R-phase to 1.27 in the T-phase in just over 10 unit cells, with the out-of-plane lattice parameter changing from 4.06 Å in the R-phase to 4.65 Å in the T-phase. The in-plane lattice parameter, constrained by the substrate lattice, changes slightly from ~3.8 Å in the R-phase to ~3.7 Å in the T-phase over the same distance. This behavior was seen to vary slightly depending on the location of the analysis within the volume of the film. In some areas of the film a smoother transition was seen to take place over a distance of up to 20 unit cells, while in other areas close to the film surface the transition was seen to occur more abruptly, in some cases as little as 5 unit cells.

In order to gain detailed atomic-scale structural information from both phases present in the mixed-phase BFO films, close-up z-contrast images were obtained and averaged structures from the images were calculated from areas containing 150 unit cells. **Figure 24(A)** and **(B)** show atomic-resolution Z-contrast images of the R-phase and T-phase, respectively, from individual stripes in a mixed phase region. Insets are the measured lattice parameters from the images (top) and the averaged structures from 150 unit cells (bottom).

From **Figure 24(A)**, the in-plane and out-of-plane lattice parameters for the R-phase were again measured to be ~3.8 Å and ~4.07 Å, respectively (inset, top), and the Fe atom is estimated to be displaced from the center of the unit cell by ~8.5%. From **Figure 24(B)**, the in-plane and out-of-plane lattice parameters for the T-phase were again measured to be ~3.7 Å and ~4.65 Å, respectively (inset, top), and the Fe atom is estimated to be displaced from the center of the unit cell by ~9.5%. These measurements are consistent with the x-ray diffraction and electron diffraction data presented earlier.

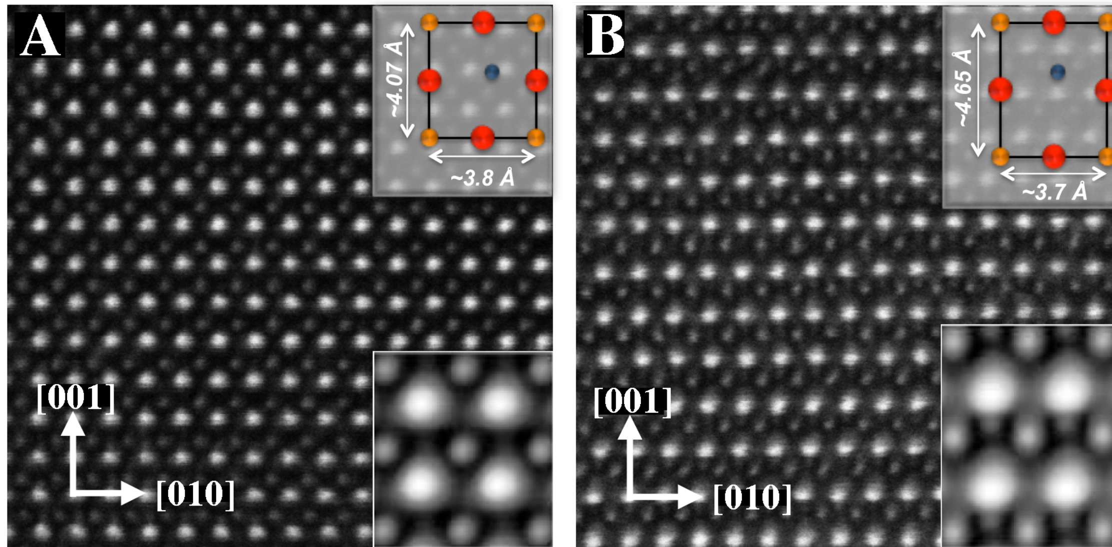

Figure 24. Atomic resolution Z-contrast images of the R-phase **(A)** and T-phase **(B)**. Insets are simplified unit cell projections with measured lattice parameters from the z-contrast images (top), and averaged structure images derived from an area containing 150 unit cells (bottom). The periodic spots of heavy Bi columns are brighter than the lighter FeO columns. The much lighter O columns are difficult to image directly in this orientation compared to the background intensity of the heavier atoms, however some O columns are evident in the T-phase average image, just below the top row of Bi atomic columns, suggesting a 5-fold coordination for the Fe cations.

The periodic spots of heavy Bi columns (Z_{Bi} = 83) are brighter than the lighter FeO columns (Z_{Fe} = 26, Z_O = 8) in the Z-contrast images of **Figure 24**. The much lighter O columns are usually difficult to image directly compared to the background intensity of the heavier atoms, because at high angles the scattering amplitude of O is quite low compared to elements like Bi and Fe. This is compounded by the tilting and rotating of the oxygen octahedra that commonly occurs in perovskite oxides, which prevents the oxygen anions from lining up in neat atomic columns along the e-beam direction, reducing their intensity. In the averaged T-phase structure of **Figure 24(B)**, however, one can see the presence of distinct intensity maxima directly below the Bi columns, which are presumed to be aligned columns of oxygen atoms. Theoretical studies, discussed later in Section 4.3.6, will show that this is consistent with the columns of O

atoms that form the basal plane of a 5-fold coordination of O anions with the Fe cations, in a similar structure to those of $PbVO_3$ and $BiCoO_3$.[78-80]

4.3.5 Nanomechanical Perturbation

To investigate how the striped mixed phase morphology in the BFO films responds to a dynamically changing strain field, the films were characterized via nano-mechanical compression experiments conducted *in situ* in a TEM.[114] For these studies, ~70 nm thick mixed phase BFO film samples were prepared for analysis using a 30 kV focused ion beam (FIB) to mill out two opposing trenches on the surface of the samples, leaving behind a thin electron transparent window ~100 nm thick. To protect the BFO films from damage due to the incident ion beam, a ~70 nm thick layer of platinum was sputter coated on top of the BFO films. A schematic of the orientation of the *in situ* nanoindenter with the electron beam and milled sample is shown in **Figure 25**.

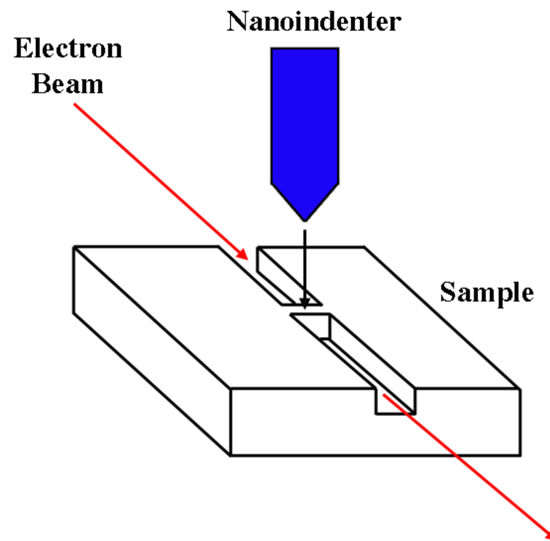

Figure 25. A schematic of the *in situ* nanoindenter in contact with a mixed phase BFO film, with an electron transparent window between two trenches milled via focused ion beam. In this geometry, the beam passes through a mixed phase area of film that is subject to an applied stress normal to the film surface.

In this schematic, the electron beam is incident on an electron transparent area of a mixed phase region of the film that is subject to an applied stress normal to the surface of the film via the nanoindenter. In this way, bright field images of a mixed phase region of the film can be observed under a dynamically changing applied stress, along with selected area diffraction patterns of the same region under the nanoindenter tip.

Representative results, including bright field images of the sample and nanoindenter tip, and corresponding selected area diffraction (SAD) patterns of the area just beneath the tip, are shown in **Figure 26**.

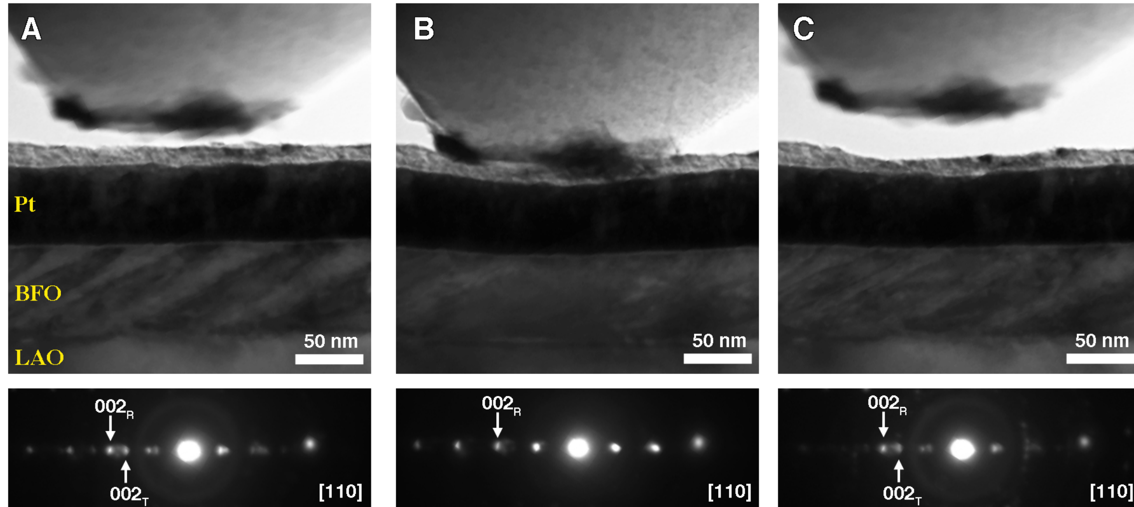

Figure 26 Bright-field TEM images (top) and corresponding selected area diffraction patterns (bottom) before **(A)**, during **(B)** and after **(C)** application of a mechanical force by a nanoindenter. In **(A)** the striped morphology of the mixed phase film is evident in the bright field image, and the corresponding SAD pattern shows 002 diffraction spots for both the R-phase and the T-phase. In **(B)** a ~30 mN mechanical force is applied by the nanoindenter, resulting in the striped morphology changing from a mixed phase to a single phase beneath the nanoindenter tip. The corresponding SAD pattern shows only the 002 diffraction spot for the R-phase. In **(C)** the nanoindenter has been retracted and the bright field image again shows a striped morphology indicating a mixed phase beneath the tip and the SAD pattern again shows 002 diffraction spots corresponding to both T-phase and R-phase.

In **Figure 26**, bright field TEM images (top) and selected area diffraction (SAD) patterns (bottom, with [110] zone axis) from an area in a mixed phase film beneath the nanoindenter are shown. The figures in **Figure 26(A)** show the film prior to applying a compressive mechanical force to the surface of the film with the nanoindenter; the striped morphology of the mixed phase is evident in the bright field image and 002 diffraction spots corresponding to both phases appear in the SAD pattern. In **Figure 26(B)**, a ~30 mN mechanical force is applied to the film with the nanoindenter. This compressive stress along the *c*-axis energetically favors the R-phase over the T-phase, and appears to cause a phase change beneath the nanoindenter, which is indicated by the striped morphology in the bright field image changing from mixed phase to single phase with no stripes. The corresponding SAD pattern in **Figure 26(B)** now shows only the 002 diffraction spot corresponding to the R-phase, also indicating a phase change from mixed phase to pure R-phase. In **Figure 26(C)** the nanoindenter has been retracted, removing the compressive force, and the bright field image again shows a striped morphology indicating a phase transformation from predominantly R-phase to a mixed phase. The corresponding SAD pattern in **Figure 26(C)** again shows the 002 diffraction spots

corresponding to both the T-phase and the R-phase, demonstrating a reversible phase transition under an applied stress.

4.3.6 Confirmation via Theoretical Models

The structural parameters obtained from the experiments in the preceding sections were used as the basis for theoretical modeling studies.[111] For detailed information on the various methods used, the reader is encouraged to consult the references given in the subsequent sections.

4.3.6.1 Density Functional Calculations

To understand the observed coexistence of the T-phase and R-phase mixed phase films, density functional calculations were performed using the structural data collected as detailed in the previous sections. Density functional theory (DFT) is a first principles ground state theory that works with charge density rather than electron wave functions, and includes the exchange interaction and electron correlation effects. The local density approximation (LDA) is used, which approximates regions of a material with a slowly varying charge density as a locally uniform electron gas. This method tends to underestimate coulomb repulsion, however, so the Hubbard parameter U is usually incorporated to correct for this (LDA+U).[115,116] For this study, a monoclinic 10-atom unit cell was used, which allows the structure to continuously change from the rhombohedral *R3c* symmetry of bulk BFO to the *P4mm* tetragonal symmetry of the theoretical tetragonal phase.[75-77] The effects of epitaxial strain were simulated by constraining the unit cell lattice vectors in the (001) pseudocubic plane and allowing the out-of-plane unit cell parameter to relax. The internal coordinates were initialized corresponding to a monoclinic *Cc* symmetry and also allowed to relax. The results of these calculations for compressive strain are shown in **Figure 27**, with energy vs. compressive strain for the two phases shown (top) as well as c/a ratio vs. compressive strain (bottom).[111] Predicted models of the T-phase and R-phase are shown as insets of **Figure 27**. The strains are given relative to the equilibrium lattice parameter a = 3.89 Å of bulk *R3c* BFO and isostrain lines are shown for all the substrates used in this study.

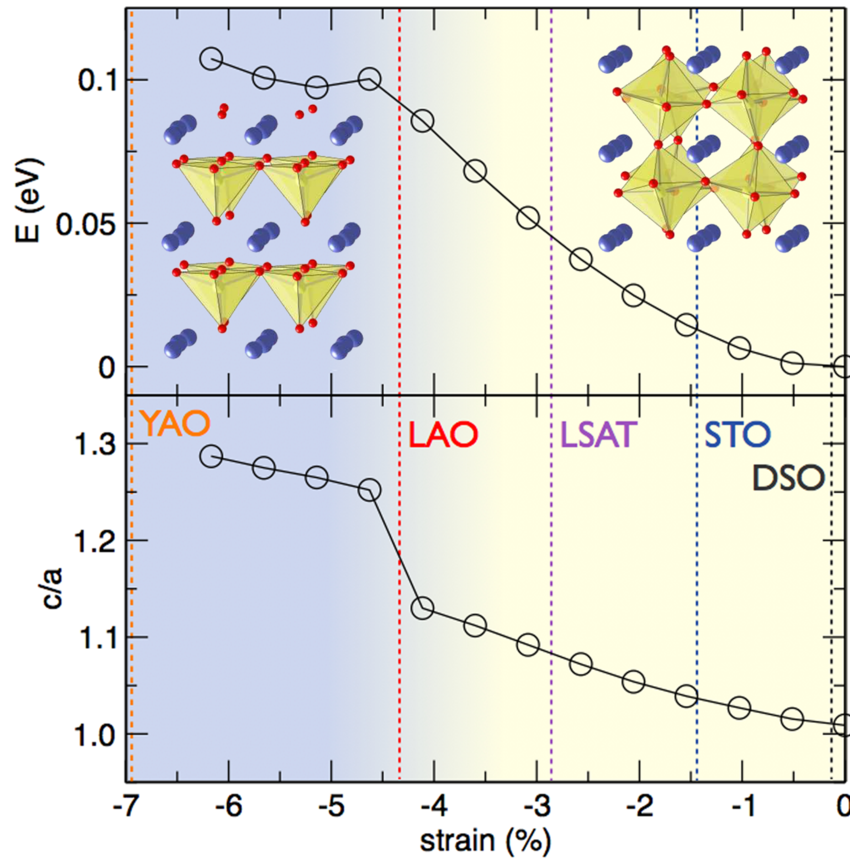

Figure 27. Density functional theory calculation results showing free energy *E* (top) and *c/a* ratio (bottom) for BFO under compressive epitaxial strain. The results suggest a volumetric increase associated with an isosymmetric phase transition between two phases with *Cc* symmetry. Predicted unit cell models are shown as inserts.

From the results shown in **Figure 27**, it can be seen that for a compressive strain of ~4.5% BFO undergoes a structural transformation that is accompanied by an abrupt increase in *c/a* ratio. From the calculations, this phase transformation is predicted to be isostructural, whereby the structures on both sides of this transition have the same *Cc* monoclinic symmetry but have dramatic differences in unit cell volume.[117,118] The unit cell models (inset in **Figure 27**) from this analysis show a distinct change in the ionic coordinates: from a distorted version of the rhombohedral bulk structure, with octahedral coordination of the Fe^{3+} cations, to a structure with a five-fold coordination of the Fe cations. This structure is similar to the observed structure for $PbVO_3$ and $BiCoO_3$, which are perovskites with high *c/a* ratios, 5-fold coordinated B-site cations, and oxygen polyhedral tilts.[78-80] These theoretical results are also consistent with the averaged Z-contrast image for the T-phase structure shown in **Figure 24(B)**, where one can clearly see the presence of distinct intensity maxima directly below the Bi columns. These are presumed to be aligned columns of oxygen atoms, corroborating the proposed 5-fold

coordination of the Fe cations with the neighboring oxygen atoms and the shift of this basal plane of oxygen atoms with respect to the Bi cations.

The energy versus strain curve in the top of **Figure 27** shows a maximum separating the two lower-energy phases at around 4.5% strain, very close to that of the LAO substrates used in these studies, suggesting that films strained to this critical value may lower their energy by spontaneously phase-separating into the T-phase and R-phase.

4.3.6.2 Phase Field Simulations

Strain-temperature phase stability diagrams were constructed for (001) oriented $BiFeO_3$ thin films using phase field modeling and thermodynamic analysis.[111] For these calculations, the spatial distribution of the polarization field is described by the time dependent Ginzburg-Landau (TDGL) equations.[119,120] For the phase-field simulation, the computational approach is described well in general reports on domain stability diagrams for ferroelectric thin films.[121] The material constants for $BiFeO_3$ used in the simulations presented here come from previously published theoretical reports using a 4th order thermodynamic potential.[122] The results from this analysis, with the predicted phase stabilities and their boundaries, are shown in **Figure 28**.

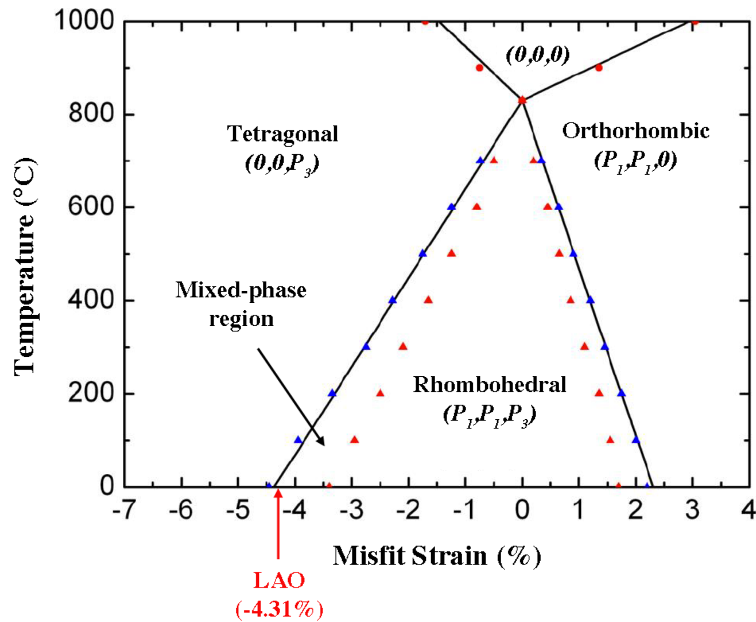

Figure 28. Phase-field modeling and thermodynamic calculations for strained BFO. The thermodynamic analysis is indicated by solid lines and the phase-field analysis is indicated by scattered symbols. The mixed-phase region consists of tetragonal, distorted rhombohedral and monoclinic phases. The results suggest that the tetragonal to rhombohedral phase boundary is near the strain value imposed by LAO at ~4.3% compressive strain at room temperature. This is consistent with DFT analysis and the experimental results.

In this figure, the thermodynamic analysis is indicated by solid lines and the phase-field analysis is indicated by scattered symbols. The different phases in the diagram are labeled cubic (0, 0, 0), rhombohedral (P_1, P_1, P_3), tetragonal (0, 0, P_3), and orthorhombic (P_1, P_1, 0). The misfit strain for BFO films grown on LAO (assuming the films are fully coherent) is -4.31% and is also indicated on the diagram. The results in **Figure 28** indicate that the tetragonal to distorted rhombohedral phase boundary is at ~4.3% compressive strain at room temperature from the thermodynamic analysis, which is very consistent with the previously detailed density function calculations and the varied experimental results, despite the uncertainty in the materials constants for BFO that were used. Taking into account domain structures, the phase-field simulations also predict a mixed-phase region of tetragonal, distorted rhombohedral, and monoclinic phases (P_1, 0, P_3) and (0, P_2, P_3) near the morphotropic boundary. It is important to note that preliminary refinements to the thermodynamic calculations above have recently been conducted using more recently derived elastic constants, new electrostrictive coefficients derived from the *c/a* ratio and polarization measurements from the experimental data in this work, and a 6th order potential.[123,124] The new potential appears to be a morphotropic phase boundary similar to that in **Figure 28**, but with more of a concave shape to the tetragonal-rhombohedral phase boundary making it nearly independent of temperature below 200 °C.

5 Electrical Characterization

From the structural characterization results presented in the previous section, it can be confidently stated that a morphotropic phase boundary exists in BFO, that the MPB can be stabilized in thin films via epitaxial constraints, and under the strain field imposed by LAO the T-phase an R-phase are sufficiently degenerate that an observable phase change occurs under nanomechanical perturbation. The next section will detail experimental efforts to determine if the electric properties of BFO have been enhanced as a result.

5.1 Bottom Electrode Deposition

For the electric testing methods used, it is necessary to establish a conductive bottom electrode between the substrate and the BFO film so that contact can be made to it and an electric field established through the film itself. The easiest way to do this is to select a conductive perovskite oxide material with an appropriate in-plane lattice parameter and grow it *in situ* via PLD on the substrate before growing the BFO film on top. The short list of conductive perovskite oxides available for this purpose includes $SrRuO_3$, $LaNiO_3$, $La_{1-x}Sr_xCoO_3$ and $La_{1-x}Sr_xMnO_3$. In this study, $La_{0.5}Sr_{0.5}CoO_3$ (LSCO) was selected because at this stoichiometry it is highly conductive and well lattice-matched (a_{pc} = 3.83 Å) with LAO substrates compared to the other available materials.[125-127] When grown very thin (~10-15 nm), LSCO is strained to adopt the lattice spacing of the underlying LAO substrates with little relaxation, preserving the epitaxial constraint imposed by the substrate on the BFO films. A schematic of the layered structure of BFO/LSCO/LAO grown *in situ* via PLD in this study is shown in **Figure 29**.

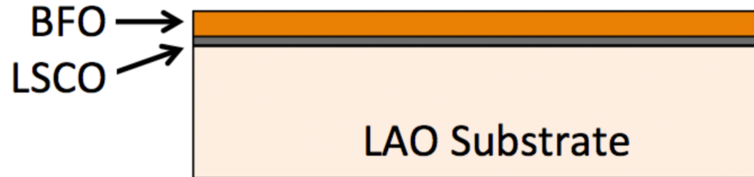

Figure 29. A schematic of the BFO/LSCO/LAO layered structure used in this study for electrical characterization of BFO films. The LSCO bottom electrode is < ~15 nm thick and completely strained, preserving the epitaxial constraint imposed on the BFO film by the underlying substrate.

To make contact with the bottom electrode for electrical characterization, the general practice is to scratch of a small corner of the film with a diamond scribe to expose the LSCO bottom electrode. Contact is then made via a small amount of silver paint.

5.2 Electrical Characterization Techniques

5.2.1 Piezoresponse Force Microscopy

Piezoresponse Force Microscopy (PFM) is one of the most widely used ferroelectric surface imaging techniques due to its relatively simple implementation, high resolution and relative insensitivity to topographical variation. It is essentially a contact mode AFM technique utilizing a metallic tip and is used to map and manipulate the local piezoelectric state of a specimen. PFM can be used for imaging the static ferroelectric domain structure in a thin film, selective ferroelectric poling of regions of a ferroelectric film surface, imaging the evolution of ferroelectric domain structures, and conducting quantitative local hysteresis measurements. For the purposes of this study, the techniques primarily used will be given a brief overview.

5.2.1.1 Ferroelectric Domain Imaging

Applying an ac electric field between a cantilever and a piezoelectric material generates a response due to the converse piezoelectric and electrostrictive effects. If one neglects capacitive, coulomb and Van der Waals forces, for a z-direction polarized and stress-free ferroelectric material, the vertical displacement (Δz) under an applied bias can be expressed as:

$$\Delta z = d_{33}V + \frac{Q_{333}}{t}V^2 \tag{28}$$

where V is the applied bias, t is the sample thickness, and d_{33} and Q_{333} are the piezoelectric and electrostrictive coefficients, respectively. The second term dependent on the electrostrictive coefficient is typically much smaller than the first for a ferroelectric material in a polarized state so it is omitted in the next equations.[14] Under an applied bias $V = V_{DC} + V_{AC}cos(\omega t)$, the piezoelectric strain causes a surface displacement:

$$\Delta z(t) = d_{33}V_{DC} + d_{33}V_{AC}cos(\omega t + \varphi) \tag{29}$$

A lock-in amplifier filters the DC component and the remaining piezoresponse signal consists of amplitude ($d_{33}V_{\omega}$) and phase (φ) components. With the phase component, the signal is dependent on the relative orientation of the polarization with the applied electric field. The lateral piezoresponse is related to the transverse component of the piezoelectric tensor, i.e. to the in-plane polarization. A schematic illustration of the piezoelectric response as measured in a PFM setup is shown in **Figure 30**.

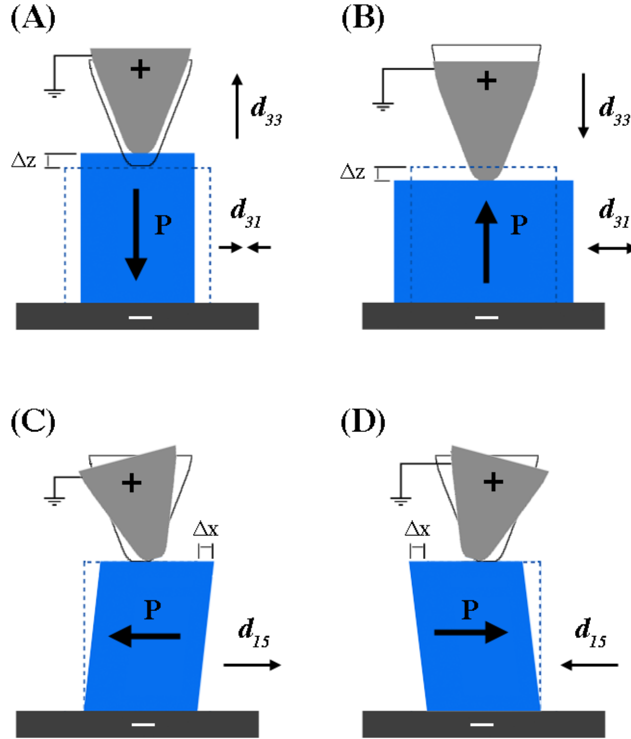

Figure 30. A schematic illustration of piezoforce domain imaging with PFM. In **(A),** when the applied E-field is parallel to the spontaneous polarization of the sample, the alternating potential of the field and the piezoelectric signal are in phase. As a result, the sample expands vertically and the cantilever is pushed up. In **(B),** when the applied E-field is antiparallel to the spontaneous polarization of the sample, the alternating potential of the field and the piezoresponse signal are out of phase by 180°. As a result, the sample contracts vertically and the cantilever is lowered. In **(C)** and **(D),** the in-plane spontaneous polarization direction of the sample can be determined by the shear piezoelectric coefficient (d_{15}). The applied E-field causes a shear deformation of the sample, which causes a torsional movement of the cantilever via friction.

In the case of applied electric field at an arbitrary angle relative to the spontaneous polarization, the detected vertical PFM signal is no longer only proportional to d_{33}, but also dependent on the d_{31} and d_{15} components:

$$\Delta z(t,\theta) = d_{33}^{*}(\theta) V_{AC} cos(\omega t + \varphi) \quad (30)$$

Where $d_{33}^{*}(\theta) = \cos\theta\,[(d_{15} + d_{31})\sin^2\theta + d_{33}\cos\theta]$ (see Section 2.3.1) and θ is the angle of rotation away from the polar axis that the measurement is being made.

5.2.1.2 Piezoelectric Hysteresis Measurements

Piezoelectric hysteresis measurements are generally performed as above, using a DC voltage source in series with an AC voltage source. The PFM tip is placed in a fixed position over either a micro-capacitor on top of the film surface (average measurement)

or the film surface itself (local measurement). The hysteresis curves are produced by sweeping the bias voltage while recording the piezoresponse signal. The procedure reported here involved superimposing a probing AC signal on the DC bias, which is varied in steps from zero to some V_{max} and then decreased down to $-V_{max}$ and again increased to zero, which effectively allows one to measure the out-of-plane piezoelectric coefficient as a function of the applied DC field. The measurements are calibrated using a standard sample with a known piezoelectric coefficient, typically quartz but standardized PZT samples are also used in this report.

5.2.2 Ferroelectric Hysteresis Measurements

When quantitatively measuring ferroelectricity one measures the capacitance of a thin film sample with top and bottom electrodes under an applied voltage that is oscillated at high frequencies by a signal generator. In general, it operates as a capacitance bridge in that it is measuring the unknown capacitance of the thin film structure by comparing the result with a known reference capacitor that is in series with the sample. With the voltage applied, a displacive charge accumulates on the electrodes of the sample structure, which can be determined using the formula $Q = C \times V$, where Q is the accumulated charge, C is the reference capacitance and V is the applied voltage. Because the capacitance of the reference capacitor is much higher than that of the sample, most of the voltage appears across the sample. This allows for a reasonably accurate estimate of the ferroelectric polarization of the sample in an oscillating electric field by plotting the surface charge vs. applied voltage. The testing equipment used is generally made with additional circuitry for reducing the effects of stray charge and parasitic measurements, allowing for a range of applied voltages (up to 100 V or more), and allowing for a range of frequencies to be used (as high as 20 kHz).[128]

The ability to use a range of frequencies is important, because artifacts in ferroelectric measurements are generally frequency dependent. To eliminate these artifacts in the measurement results, pulsed measurement techniques called “positive up negative down” or PUND can be utilized, whereby a range of positive and negative pulses are applied to the samples and the ferroelectric polarization switching characteristics can be measured. A simple schematic of how a PUND measurement is made can be seen in **Figure 31**.

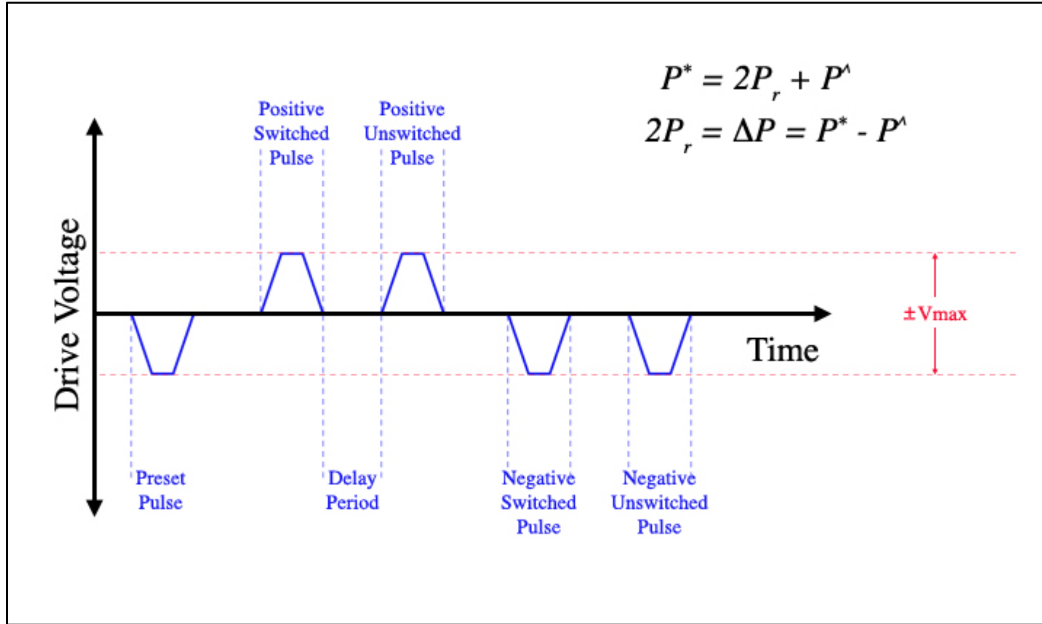

Figure 31. Schematic of how a standard PUND (positive up negative down) measurement is made. Measurements are made at the positive switched pulse (P^*) and the positive unswitched pulse ($P^\wedge$), and similar measurements are made at the negative switched and unswitched pulses. $P^\wedge$ represents the volatile component of the polarization, such as leakage effects and parasitic capacitance.

In these experiments, measurements are made at the positive switched pulse, giving a polarization P^* which includes the remnant and non-remnant polarization, and at the positive un-switched pulse, giving a polarization $P^\wedge$ which includes only the non-remanent polarization. The latter represents the volatile component of the polarization in the samples, such as leakage effects and parasitic capacitance. Similar measurements are made at the corresponding negative switched pulses as well. By conducting the measurements in this way, the remnant polarization P_r can be determined.

5.3 Electric Field Induced Phase Changes

5.3.1 Ferroelectric Poling and Phase Evolution

For ferroelectric imaging, information on topography, out-of-plane piezoresponse, and in-plane piezoresponse were simultaneously collected. The images in **Figure 32** show representative PFM measurements taken on a ~60 nm thick mixed phase BFO film grown *in situ* on a ~10 nm thick layer of LSCO as a bottom electrode on the underlying LAO substrate.

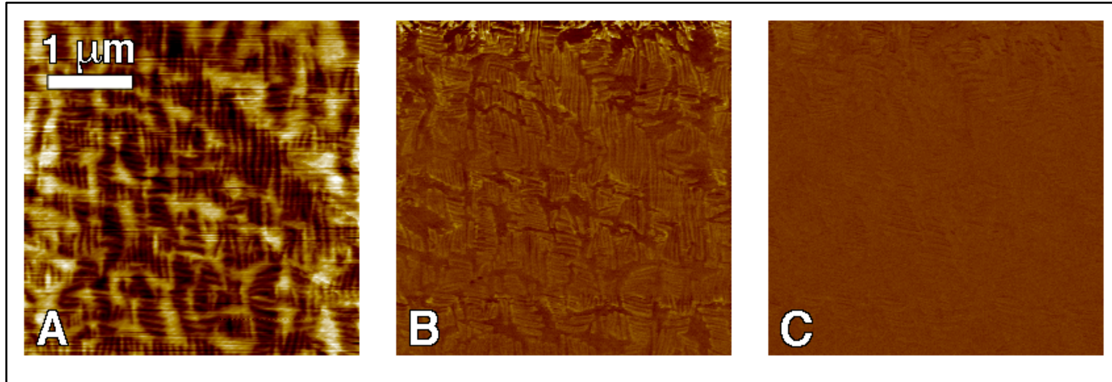

Figure 32. Piezoforce microscopy images of a ~60 nm thick mixed phase BFO film grown on a ~10 nm LSCO bottom electrode layer. For these scans a -4 V DC bias is applied with a 2 V_{pp} AC component. **(A)** Topographical scan of the film with a height range of 5 nm, showing the mixed phase morphology. The lighter (higher) regions are the T-phase and the darker (lower) regions are the R-phase. **(B)** Out-of-plane piezoresponse showing contrast consistent with the mixed phase topography. The as grown polarization is down towards the substrate, thus with the applied E-field pointing up out of the film the T-phase contrast is darker than the R-phase. **(C)** In-plane piezoresponse consistent with the mixed-phase morphology of monoclinically distorted T-phase an R-phase.

These measurements were conducted using a -4 V DC tip bias with a 2 V_{pp} AC component. The LSCO layer is clearly thin enough to preserve the epitaxial constraint imposed on the BFO films by the underlying substrate as the topographical scan in **Figure 32(A)** shows a mixed-phase morphology. The out-of-plane piezoresponse scan in **Figure 32(B)** shows contrast consistent with the topographical morphology. The ground state spontaneous polarization of the as-grown film is pointing down towards the substrate. As such, with an applied E-field pointing up out of the film and away from the substrate, the T-phase shows a darker contrast than the R-phase, as it is more anti-parallel to the applied E-field. The faint contrast in the in-plane piezoresponse scan in **Figure 32(C)** is also consistent with the mixed-phase morphology of the film, as the R-phase has more of an in-plane component to its spontaneous polarization than the monoclinically distorted T-phase.

Electrical poling was subsequently conducted on the same sample to probe the ferroelectric nature of the mixed phase BFO films and to explore the effects on film morphology and polarization under an applied DC bias in excess of the films coercive field.[111] These measurements were conducted by applying a DC bias to the scanning tip in a localized square area of the film, and subsequently performing a PFM scan using a -4 V DC tip bias with a 1 V_{pp} AC component to observe the results. To probe the ferroelectric switching characteristics of the films, alternating positive and negative DC poling fields were applied to the film in the same local square area, switching the polarization from down to up and back down again. The resulting scans of the topography and out-of-plane piezoresponse are shown in **Figure 33** along with schematic representations of the phase morphology and corresponding polarization within the poled area of the films.

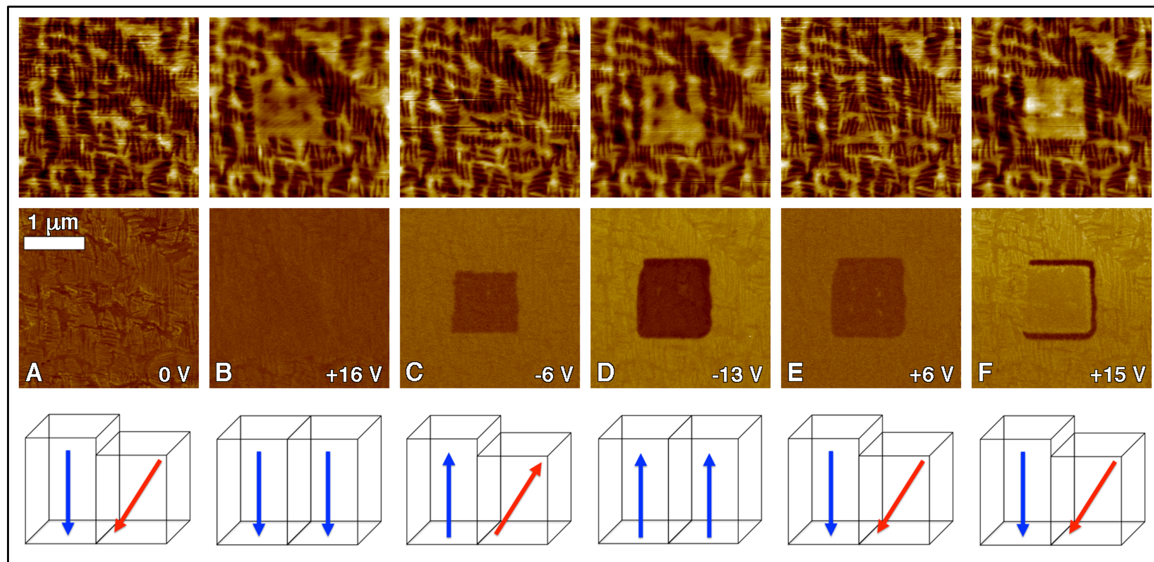

Figure 33. In **(A)** through **(F)**, the top images are the topographical scans, the middle images are the out-of-plane piezoresponse scans, and the bottom images are simplified schematics of the phase morphology and polarization orientations of the poled area in the center of the visible area of the film. Blue polarization arrows indicate the T-phase and red polarization arrows indicate the R-phase. The images in **(A)** show the as-grown film in its ground state, with T-phase and R-phase domains coexisting and a spontaneous polarization down into the film towards the substrate. As a scanned poling field is applied to a square area of the film, varying in value and alternating in polarity in **(B)** through **(F)**, the phase morphology changes from mixed-phase to nearly all T-phase and back again in a repeatable manner.

In **Figure 33**, the top images are the topographical scans, the middle images are the out-of-plane piezoresponse scans, and the bottom images are simplified schematics of the phase morphology and polarization orientations of the poled area in the center of the images. Blue polarization arrows indicate the T-phase and red polarization arrows indicate the R-phase. The images in **Figure 33(A)** show the as-grown film in its ground state, with T-phase and R-phase domains coexisting with a spontaneous polarization down into the film towards the substrate. Prior to the scans taken in **Figure 33(B)**, a square area in the center of the visible portion of the film was poled via scanning the probe tip over it with a +16 V DC tip bias, effectively applying a downward oriented electric field. The T-phase has a polarization that is nearly parallel with the applied electric field and its energy is lowered relative to the R-phase in the poled area making it energetically favorable. A field-induced phase transformation occurs in the poled area which was previously mixed phase, leaving the morphology mostly T-phase as can be seen in the topographical scan of **Figure 33(B)** where the lighter (higher) areas indicate T-phase, as does the square of darker contrast in the out-of-plane piezoresponse in the center of the figure. The corresponding schematic in **Figure 33(B)** shows only T-phase domains. Prior to the scans taken in **Figure 33(C)**, the same area of the film was poled with a -6 V DC tip bias, applying an upward oriented electric field. This exceeds the coercive field of the film and flips the polarization state so that it points up out of the film and away from the substrate, as can be seen in the out-of-plane piezoresponse scan in the

figure. This applied upward oriented E-field is not enough to preferentially favor either phase, however, and a mixed phase morphology results again in the poled area as can be seen in the topographical scan of **Figure 33(C)**. When the field is further increased in the same direction by applying an even higher -13 V DC bias to the poled area prior to the scans taken in **Figure 33(D)**, the T-phase is again energetically favored over the R-phase in the poled area. Prior to scans taken in **Figure 33(E)** the field is reversed again by applying a +6 V DC bias to the poled area. This is not enough of a field to overcome the coercive bias of the film in all but a few locations but it is enough to again see a mixed-morphology. The process is completed in **Figure 33(F)** by applying a +15 V DC bias to the poled area prior to taking the scans shown and effectively flipping the polarization in the poled area down again.

5.3.2 Local Phase Response to Applied Nanoprobe Bias

To gain further understanding of the E-field induced phase transformation in mixed phase films, *in situ* nanoprobe ferroelectric poling in the TEM was utilized to characterize a ~70 nm thick mixed phase BFO film grown on a ~10 nm thick LSCO bottom electrode layer on and LAO substrate.[114] The samples were prepared in the same way as described for the *in situ* nanoindentation experiments with the platinum top electrode removed. In place of the nanoindenter, the nanoprobe was equipped with a biasing sample stage, which allowed a bias to be applied to the sample with the bottom electrode of the film completing the circuit. This allowed for a localized electric field to be applied to the sample just below the nanoprobe tip. Selected area diffraction patterns were taken from the area just below the nanoprobe before, during and after the field was applied. Representative results from these experiments are shown in **Figure 34**.

In **Figure 34**, bright field TEM images (top) and selected area diffraction (SAD) patterns (bottom, with [100] zone axis) of an area in a mixed phase film beneath the nanoprobe are shown. The images in **Figure 34(A)** show the film prior to applying a bias to the nanoprobe. The striped morphology of the mixed phase is evident in the bright field image and $0\bar{1}1$ diffraction spots corresponding to both phases appear in the corresponding SAD pattern. In **Figure 34(B)**, a +20 V bias is actively applied to the nanoprobe, resulting in an applied E-field pointing into the film towards the substrate. This applied field makes the T-phase energetically favorable to the R-phase due to the nearly parallel alignment of its spontaneous polarization with the applied field. This causes a field induced phase change beneath the nanoprobe, which is indicated by the striped morphology beneath the nanoprobe in the bright field image changing from mixed phase to single phase. The corresponding SAD pattern in now shows only the $0\bar{1}1$ diffraction spot of the T-phase. In **Figure 34(C)** the bias had been removed and the bright field image again shows a striped morphology indicated a phase transformation from T-phase back to a mixed phase. The corresponding SAD pattern again shows the $0\bar{1}1$ diffraction spots corresponding to both the T-phase and the R-phase, demonstrating a reversible phase transition and phase morphology evolution.

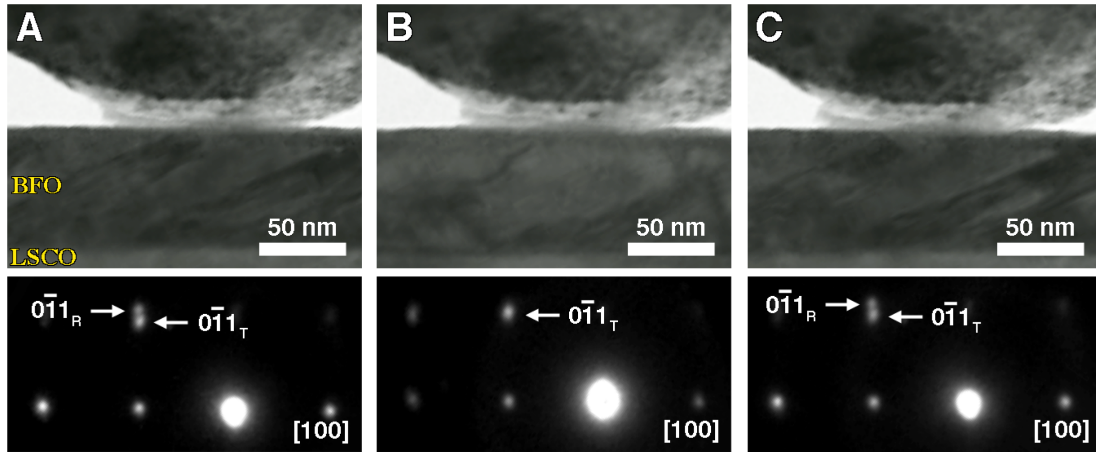

Figure 34. Bright field TEM images (top) and selected area diffraction (SAD) patterns (bottom) of an area in a mixed phase film. The figures in **(A)** show the film prior to applying the bias, where the striped morphology of the mixed phase is evident in the bright field image and $0\bar{1}1$ diffraction spots corresponding to both phases appear in the SAD pattern. In **(B)** a +20 V bias is applied to the nanoprobe, resulting in the striped morphology changing from a mixed phase to a single phase beneath the nanoprobe tip. The SAD pattern now shows only the $0\bar{1}1$ diffraction spot corresponding to the T-phase. In **(C)** the bias has been removed and the bright field image again shows a striped morphology indicating a mixed phase. The corresponding SAD pattern in **(C)** again shows the $0\bar{1}1$ diffraction spots corresponding to both the T-phase and the R-phase.

5.4 Evidence for Enhanced Electrical Properties

5.4.1 Top Electrode Deposition

To characterize the averaged ferroelectric and piezoelectric properties of the BFO thin films, top electrode contacts are required. These are generally fabricated via photolithography methods to create an array of equally sized micron-scale circular contacts. In this manner, there are many contacts available to make quality repetitive quantitative measurements. Unless otherwise noted, the top electrodes used in this study are ~24 μm in diameter and consist of a layer of platinum deposited on top of the BFO film. In some instances, a layer of LSCO is grown between the BFO films and the Pt contacts to ensure good ohmic contact with the BFO film. A schematic of the lithographic process used to create the Pt/LSCO top electrodes is shown in **Figure 35**.

The steps illustrated in **Figure 35(A-I)** are as follows: Beginning with the same BFO/LSCO/LAO layered structure grown for the ferroelectric poling experiments described previously **(A)**, a thin layer of LSCO is additionally grown *in situ* on top of the BFO film **(B)**. Then a layer of photoresist is spin-coated on and cured at 90 ˚C with a resistive heater for one minute **(C)**. A chrome mask with the electrode array pattern is then carefully placed on the sample and exposed to UV light for 90 seconds **(D)**. The exposed areas of the photoresist are removed by immersing the sample in a developer solution **(E)**. A thin layer of platinum is then sputter coated on top of the sample surface

(F). Immersing the sample in acetone lifts off the remaining photoresist and the excess platinum on top if it, leaving only the 24 μm top Pt contacts **(G)**.

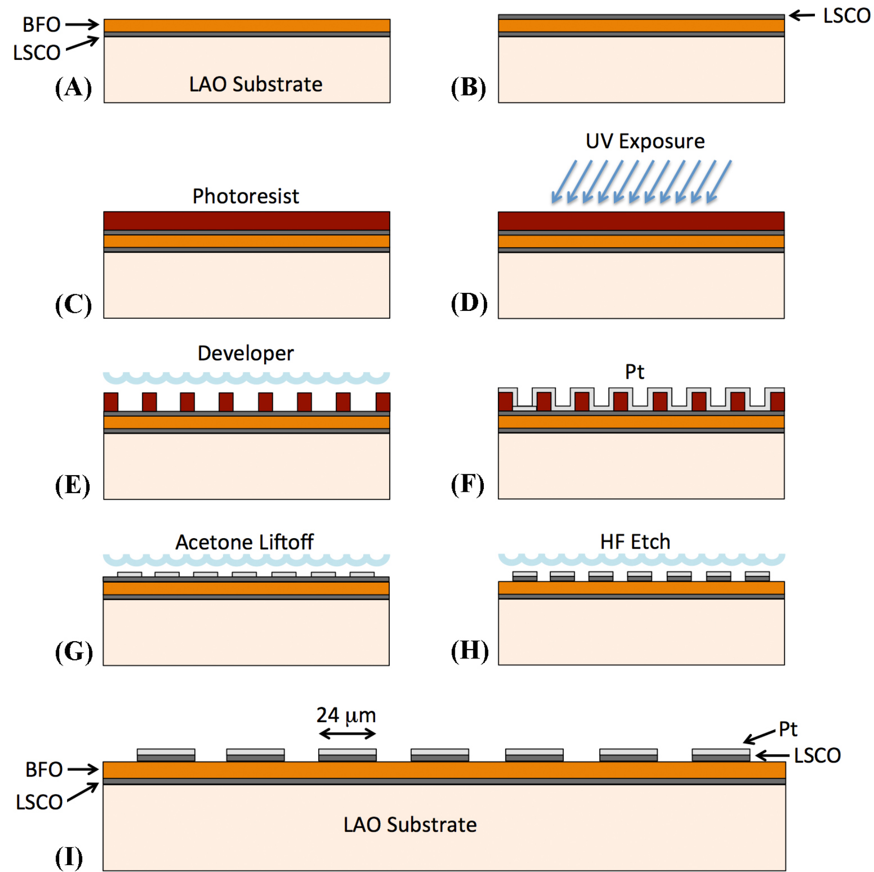

Figure 35. Schematic of the process used to create Pt/LSCO microcapacitors on BFO films for electrical characterization. **(A)** A BFO film is grown *in situ* on a bottom electrode layer of LSCO. **(B)** Another layer of LSCO is grown *in situ* on top of the BFO film. **(C)** Photoresist is spin coated on to the surface and cured. **(D)** A patterned chrome mask is placed on the surface and the sample is exposed to UV light. **(E)** The exposed regions are removed when the sample is immersed in developer solution. **(F)** A thin layer of platinum is sputter coated on to the surface. **(G)** An acetone immersion lifts off the remaining photoresist and the platinum on top of it, leaving only the circular platinum contacts. **(H)** A hydrofluoric acid immersion preferentially etches the exposed LSCO that is not protected by the platinum contacts. **(I)** What remains is a stack consisting of the LAO substrate, a bottom electrode layer of LSCO, the BFO film and a series of ~24μm diameter Pt/LSCO top electrodes.

A hydrofluoric acid immersion for ~30 seconds (depending on the LSCO thickness) preferentially etches the exposed LSCO that is not protected by the platinum contacts **(H)**. What remains is a series of ~24μm diameter Pt/LSCO top electrodes **(I)**.

5.4.2 Ferroelectric Polarization Measurements

Quasistatic ferroelectric polarization measurements at a frequency of 10 kHz were conducted on three types of samples for comparison: predominantly T-phase samples with thicknesses of < 15-20 nm, mixed phase samples with thicknesses of 50-100 nm, and predominantly R-phase samples with thicknesses in excess of ~250 nm. All samples consisted of a BFO layer grown on LAO(001) substrates with a thin LSCO bottom electrode layer. The bottom electrodes were maintained at thicknesses of ~10-15 nm to preserve the epitaxial constraint imposed on the BFO films by the underlying substrate. The 24 μm diameter top electrodes consisted of a ~15 nm thick layer of LSCO to provide ohmic contact to the BFO films and an additional ~30-40 nm thick layer of sputter coated platinum. Representative data for the results for the mixed-phase and pure R-phase films can be seen in **Figure 36**. In the case of the pure T-phase films, high-quality ferroelectric hysteresis loops were unfortunately impossible to obtain due to resistive leakage through the very thin films, which is a general problem with direct ferroelectric measurements of ultrathin films.

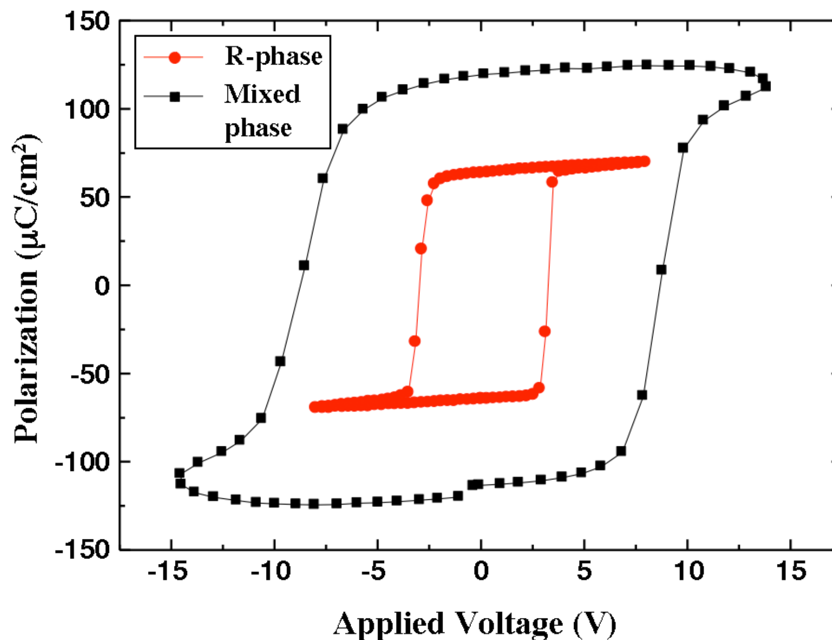

Figure 36. Quasistatic (slow) ferroelectric measurements of mixed phase and predominantly R-phase BFO films on LAO. Mixed phase films show a polarization of ~125 μC/cm^2. This is higher than that measured for the mostly R-phase films, which show a polarization of ~60 μC/cm^2, consistent with measurements on rhombohedral BFO films.

In **Figure 36**, the mostly R-phase film shows a remnant polarization of ~60 μC/cm^2, consistent with previous reports on rhombohedral BFO films. The mixed phase sample shows a significantly higher remnant polarization of ~125 μC/cm^2, a considerable enhancement compared to the R-phase films. From the rounded shape of the loop and the

small discontinuity at the origin, it is suspected that there are some small contributions from resistive leakage.

To minimize the effects of resistive leakage and other artifacts in the results, pulsed polarization measurements were conducted for comparison. The results are shown in **Figure 37**.

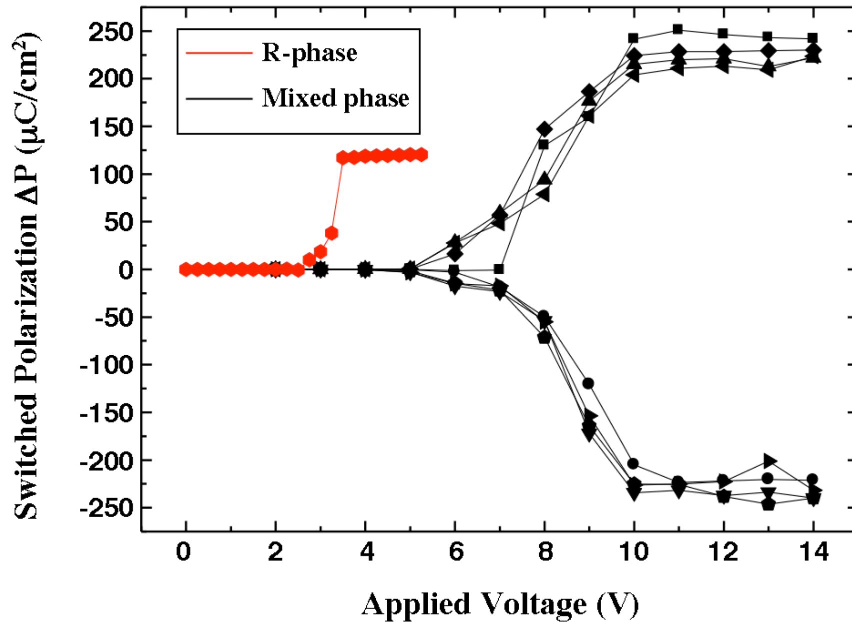

Figure 37. Pulsed polarization measurements (PUND) with a pulse width of 5 μs. The mixed phase sample shows a switched polarization of ~220 $\mu C/cm^2$, which is consistent with the quasistatic measurements. In contrast, the R-phase sample above shows a switched polarization of ~110 $\mu C/cm^2$, also consistent with the quasistatic measurements as well as previous reports on rhombohedral BFO films. Note that in the measurements above the R-phase film was only characterized in one polarization direction.

In this figure, the mixed phase sample shows a higher switched polarization of ~220 $\mu C/cm^2$, which is consistent with the quasistatic measurements in **Figure 36**. In contrast, the R-phase sample shows a switched polarization of ~110 $\mu C/cm^2$, also consistent with the quasistatic measurements as well as previous reports on rhombohedral BFO films.

5.4.3 Piezoelectric Hysteresis Measurements

Averaged piezoelectric response under the 24 μm diameter platinum contacts was probed by recording hysteresis loop measurements carried out using a scanning probe system equipped with a metalized AFM cantilever. For these measurements, a quartz plate reference sample and a standard 70 nm thick tetragonal PZT sample with a $Pb(Zr_{0.2}Ti_{0.8})O_3$ composition were used for calibration. Measurements were made on predominantly T-phase films with thicknesses of ~15 nm, mixed phase films with

thicknesses of ~80 nm, and predominantly R-phase films with thicknesses in excess of 250 nm. Representative results from these measurements are shown in **Figure 38**.

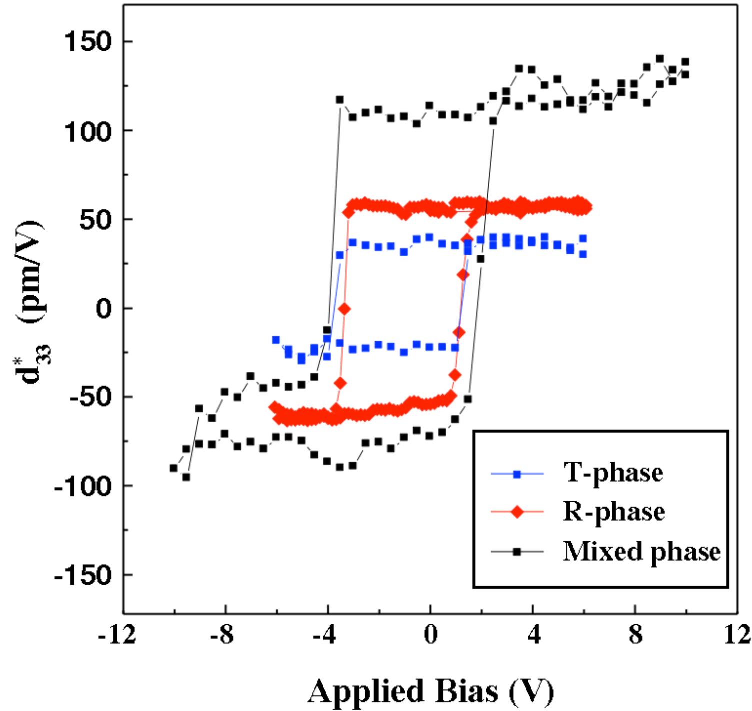

Figure 38. Representative plots of d^*_{33} vs. applied bias for predominantly T-phase, mixed phase, and predominantly R-phase BFO films (blue, black and red lines, respectively) grown on a LSCO bottom electrode with 24 μm diameter Pt/LSCO top electrode contacts. The BFO film thicknesses are approximately 15 nm, 80 nm and 250 nm respectively. The thin predominantly T-phase film shows the lowest out-of-plane piezoresponse of ~30-35 pm/V, while the mixed-phase film shows the highest at ~115-120 pm/V. The predominantly R-phase sample has a measured piezoresponse of ~50-60 pm/V, which is consistent with widely reported results on rhombohedral BFO films. The apparent asymmetry for positive and negative applied potential is primarily a consequence of the asymmetric mechanical boundary conditions that the piezoelectric layer is experiencing, namely the LAO substrate on one side and a free surface on the other.

The y-axis in this figure is the out-of-plane piezoresponse (d^*_{33}) as a function of the applied DC field on the microcapacitor. The piezoresponse of the pure R-phase sample is measured to be ~50-60 pm/V, which is consistent with previously reported results on rhombohedral BFO films.[66,68,73,74] It can be seen from the figure that the pure T-phase sample shows the lowest value of ~30-35 pm/V, while the mixed phase sample shows the highest value of ~115-120 pm/V. This apparent enhancement of the piezoelectric response is consistent with the mixed phase samples being the closest to the morphotropic phase boundary and the piezoelectric properties greatly enhanced compared to the two other films with strains that are farther from the phase boundary.

These results have since been corroborated through subsequent experiments on mixed-phase films with 32 μm diameter Pt top electrode contacts.[114]

In an effort to minimize clamping effects from the top contacts and measure a local electromechanical response of the mixed-phase BFO films relative to a known reference material system, characterization was conducted by measuring piezoresponse hysteresis loops on films with only a bottom electrode layer.[114] In place of the Pt/LSCO top electrodes used in the above studies, a conductive AFM tip was directly used as the top electrode. The same experiment was carried out on a PZT film with a $Pb(Zr_{0.2}Ti_{0.8})O_3$ composition under identical conditions as a reference d_{33}^* value of 65 pm/V. Representative results of these studies are shown in **Figure 39**.

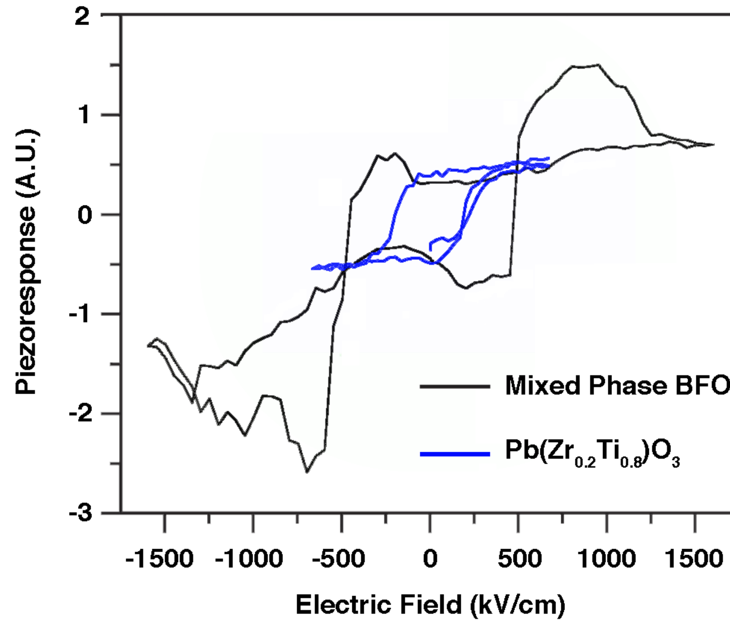

Figure 39. Local piezoresponse measurements of mixed phase BFO compared to a known reference sample of PZT. These measurements were taken using a conductive AFM tip at the top electrode. The black curve represents the data from a mixed phase BFO/LSCO/LAO film and the blue curve represents data from a reference sample of PZT with a measured d_{33}^* value of 65 pm/V. The results suggest the local d_{33}^* value for mixed phase BFO is ~520 pm/V.

The expression relating the converse piezoelectric coefficient, dielectric constant, tip–sample interaction and piezoresponse amplitude in this kind of measurement is:[129]

$$d_{33}^* = \frac{\Delta Z \int_0^{r_0} r \partial r}{\varepsilon_r \int_0^{r_0} \int_0^t E r \partial t \partial r} \tag{31}$$

where d_{33}^* is the converse piezoelectric coefficient out of the plane of the film, ΔZ is proportional to the piezoresponse amplitude, r is the radius of curvature for the PFM tip, ε_r is the dielectric constant of the material, and t is the film thickness. If one assumes the superposition of the probe with respect to the surface of the film and the geometry of the probe tip to be constant, d_{33}^* can be estimated using the values of ε_r and ΔZ under the applied electric field. The values of ε_r for BFO and PZT are reported to be approximately 200 and 100, respectively.[130,131] The measured result in **Figure 39** indicates that the maximum piezoresponse amplitude of the mixed-phase BFO films is almost four times higher than that from the PZT film, thus the d_{33}^* value for the mixed-phase BFO films can be estimated to be eight times higher, or ~520 pm/V.

6 Summary of Findings

In Section 1 of this manuscript, the goal of this research is proposed to demonstrate that epitaxial strain could be used to engineer a morphotropic phase boundary (MPB) in a lead-free ferroelectric perovskite oxide, and to confirm that doing so will greatly enhance the piezoelectric propertied of the material. In Section 2, after an overview on the theory of high-performing piezoelectrics like PZT and an examination of the role of lead in these materials, it is proposed that a perovskite oxide with bismuth on the A-site should be a selection criterion for any candidate material. Furthermore, a material with structural similarities to PZT is preferable, i.e. one that has rhombohedral ground-state symmetry, shows evidence for a monoclinic distortion, shows evidence for the existence of a tetragonal phase, and ideally has an environmentally friendly and abundant B-site atom. Bismuth ferrite (BFO) was selected as a candidate material, and the general experimental approach to the proposed research goals is presented. In Section 3, the growth of BFO thin films on a variety of perovskite substrates with different in-plane lattice parameters, including DSO, STO, LSAT, LAO and YAO, is detailed.

In Section 4 these films are structurally characterized and the results presented with analysis. They are demonstrated to be single phase and very smooth, as verified by x-ray diffraction (XRD) and atomic force microscopy (AFM). The XRD and AFM results provide evidence that the films under the most compressive strain, on LAO and YAO substrates, adopt a monoclinically distorted tetragonal structure (the T-phase) with a high *c*/*a* ratio of ~1.26, with excellent agreement with the predicted parameters from theoretical results on strained BFO. The films grown under less compressive strain on the other three substrates used adopt the familiar monoclinically distorted rhombohedral structure (the R-phase) seen previously in BFO films, with different degrees of in-plane and out-of-plane lattice distortion due to the varying applied strains from the substrates. The results from the preliminary XRD analysis suggest that a phase change occurs in BFO films between the strains imposed by LSAT and LAO substrates. To probe this further and examine how the film morphology evolves with applied in-plane stress, a thickness series of films is grown on LAO to examine the structural and topographical changes that occur as the strain is gradually diminished in thicker and thicker films as they relax.

In films grown on LAO, with a compressive strain of -4.31% relative to the bulk phase, a mixed-phase morphology is seen to emerge in all but the thinnest of films. The thinnest films are predominantly T-phase with no detectable R-phase via XRD and AFM analysis. The mixed-phase films are characterized via AFM as having a mostly T-phase matrix with a striped-pattern of R-phase emerging, with the R-phase stripes becoming larger and more numerous with increasing film thickness. XRD spectra on thick BFO films confirm the emergence of the R-phase with increasing film thickness. Additional characterization on a thickness series with optical second harmonic generation (SHG) confirm the presence of only the T-phase in the thinnest (~17 nm) of films but both the T-phase and an increasing amount of R-phase in thicker films with increasing thickness.

The evidence from the structural characterization measurements strongly suggests that the mixed phase films represent a delicate energetic balance between the monoclinically distorted R-phase and the newly confirmed monoclinically distorted T-phase. The in-plane compressive strain due to underlying LAO substrate energetically favors the T-phase in the thinnest films, and as the films increase in thickness the strain field gradually decreases and lowers the energy of the R-phase until the two phases are energetically degenerate in the film resulting in a mixed phase morphology. To confirm this beyond doubt, transmission electron microscopy is used to further characterize the mixed phase films, in particular the constituent phases present in a striped region of the film as well as the phase boundary between them. Cross-sectional bright field imaging results show the striped pattern going through the thickness of the film, with the R-phase forming wedge shapes that are thicker at the film surface and the T-phase forming wedge shapes that are thicker at the substrate. These observations are consistent with the topographical AFM scans on the film thickness series, and demonstrate that the higher strain state near the film-substrate interface energetically favors the T-phase, while the R-phase becomes more stable as the strain decreases through the thickness of the film. Z-contrast images are taken from a phase boundary between two of the striped phases and the results indicate a coherent interface with no dislocations or stacking faults found between the T-phase and the R-phase, indicating that the change in unit cell volume across the phase boundary is accommodated purely by strain effects. Z-contrast images and selected area electron diffraction patterns are obtained from individual T-phase and R-phase areas in a striped region of the film, and lattice constant measurements are consistent with previous XRD results. The Z-contrast images also suggest the T-phase has a higher spontaneous ferroelectric polarization than the R-phase, based on the relative Fe and Bi cation displacement, and that its ferroelectric polarization is nearly out of plane.

Having stabilized a delicate balance between at least two nearly degenerate crystallographic phases in the same film via epitaxial strain, the films are then subjected to a dynamically changing applied strain field to see how the phase morphology is affected by mechanical perturbation. This is conducted using a nanoindenter physically incident upon the surface of a mixed phase film while *in situ* in a TEM. Cross-sectional bright field images of a striped region show the mixed-phase morphology changing to nearly all R-phase under an applied ~30 mN mechanical force from the nanoindenter tip. This phase change is verified via selected area diffraction of the area beneath the nanoindenter tip, and is shown to be reversible upon the retraction of the nanoindenter.

Up to this point in the presented research summary, it has been confirmed that a new monoclinically distorted tetragonal phase has been stabilized in BFO and in all but the thinnest of films it is nearly degenerate with the more familiar monoclinically distorted rhombohedral phase. This is demonstrated by perturbing the relative energy of the phases in the films via strain relaxation in a film thickness series, and by nano-mechanical indentation dynamically affecting the volume fraction of the phases present under the nanoindenter tip. It is clear that a MPB has been stabilized in a (lead-free) material via epitaxial strain for the first time. This is confirmation that the first half of the research objectives laid out for this study have been achieved. The second half involves the electric characterization of these mixed phase films to determine if their

piezoelectric properties have been enhanced compared to pure rhombohedral phase BFO films.

In Section 5 the BFO films are grown *in situ* on a bottom electrode of LSCO between the film and substrate. Topographic PFM scans confirm that the mixed phase morphology remains, demonstrating that the LSCO is imposing the strain of the substrate on to the BFO films. The PFM scans also show in-plane and out-of-plane contrast consistent with the mixed phase morphology of the films and the monoclinic distortion of the T-phase. By poling the film in a square area of the film from a downward polarization to an upward one and back again, it is qualitatively confirmed that the films are ferroelectric and their polarization can be reversibly switched. Furthermore, it is observed that poling the film in the same area up and down repeatedly results in a repeatable topographical morphology change in the poled area as a result of a field induced phase change. The T-phase is energetically favored at high fields due to its spontaneous polarization vector being more parallel to the applied field than that of the R-phase. At intermediate fields, the relative energies of the two phases are nearly degenerate and a mixed phase morphology results in the poled area. The phase evolution process is reversible, with the morphology changing again with the applied field resulting in a T-phase dominant morphology at high fields and a mixed-phase morphology at intermediate fields, regardless of the field direction normal to the surface of the film. This again demonstrates the delicate energetic balance between the two phases in the mixed phase films, with an applied E-field being enough to perturb the films from a mixed phase state to a predominantly T-phase state and back again during ferroelectric poling.

To demonstrate this effect more clearly, localized E-field induced phase change experiments are conducted with a TEM equipped with an *in situ* nanoprobe capable of applying a localized bias. Bright field images of a striped region of film are recorded under the nanoprobe tip. Under no bias, the familiar striped mixed phase morphology is evident. Under an applied bias of +20 V, the T-phase is favored energetically due to its spontaneous polarization vector being nearly parallel with the applied field and the morphology under the nanoprobe tip changes from mixed-phase to nearly all T-phase. The effect is reversed when the applied bias is removed. Selected area diffraction patterns taken from the poled area confirm the phase change under an applied electric field.

After detailing the process used for forming micron-scale top electrodes on the film, the second half of Section 5 is dedicated to quantitative electrical measurements on the mixed phase films to determine if its properties have been enhanced. Quasistatic ferroelectric polarization measurements on mixed-phase and pure R-phase films show a dramatic improvement in ferroelectric polarization in the mixed phase films, with a measured polarization of ~125 $\mu C/cm^2$ for the mixed phase compared to ~60 $\mu C/cm^2$ for the R-phase films. These results are consistent with previously reported measured polarizations for rhombohedral BFO films, and the polarization measurement for the mixed phase films is quite close to the predicted polarization of ~150 $\mu C/cm^2$ for the theoretical *P4mm* phase of BFO. To minimize the effects of resistive leakage in the

ferroelectric measurements, pulsed measurement techniques (PUND) were also carried out using 5 μs, square pulses. The results from these measurements show a higher switched polarization of ~220 $\mu C/cm^2$ for the mixed phase samples compared to ~110 $\mu C/cm^2$ for the R-phase sample, consistent with the quasistatic measurements and reports on rhombohedral BFO films.

The last part of Section 5 details piezoelectric hysteresis measurements on mixed phase films. First, spatially averaged piezoelectric response under the platinum contacts is probed by recording hysteresis loop measurements using a scanning probe system equipped with a metalized AFM cantilever tip. For these measurements, a quartz plate reference sample and a standard PZT reference sample are used for calibration. Measurements are made on predominantly T-phase films, mixed phase films, and predominantly R-phase films and the results compared. The T-phase films show the lowest out-of-plane piezoresponse of ~30-35 pm/V, while the mixed-phase films show the highest at ~115-120 pm/V. The predominantly pure R-phase sample has a measured piezoresponse of ~50-60 pm/V, which is consistent with widely reported results on rhombohedral BFO films. These results demonstrate a profound improvement in the piezoelectric properties of the mixed phase films compared to the R-phase films. To try and minimize clamping effects from the top contacts in the piezoresponse measurements, local electromechanical response measurements were carried out using only a bottom electrode layer and a conductive AFM tip as the top electrode. Calibration for these measurements was done using a known PZT reference sample. The preliminary results from this investigation suggest a measured piezoresponse of ~520 pm/V.

In conclusion, epitaxial films of the lead-free ferroelectric BFO deposited on LAO substrates are demonstrated to have a strain stabilized morphotropic phase boundary. The phase morphology is found to evolve with thickness and can be reversibly perturbed by dynamically applied mechanical forces and electric fields, demonstrating the near degeneracy of the constituent phases and low energy barrier for phase transformation in these films. The piezoelectric and ferroelectric properties are measured for the mixed phase with strong evidence for enhancement. The spatially averaged switched ferroelectric polarization (ΔP) and out-of-plane piezoelectric coefficient (d_{33}^{*}) values for mixed phase films measured with micron sized capacitors are ~220 μC/V and ~120 pm/V, respectively, both values on the order of twice that reported for pure rhombohedral phase BFO films. The local piezoresponse as a result of the field induce phase transition for mixed phase films is ~520 pm/V, on the order of 4 times that of a PZT(20/80) reference sample. Thus, the mixed phase films have a pronounced enhancement in their ferroelectric and piezoelectric properties due to the strain stabilization of the morphotropic phase boundary in BFO by the underlying substrate.

7 Recommendations for Future Work

7.1 Growth on Silicon Based Heterostructures

Although the potential for using strained BFO films as a lead-free replacement for PZT thin films is clearly evident, it will not be possible unless the manufacturing process can be scaled. This usually means integration into a silicon-based fabrication process – i.e. growing films on silicon substrates via a scalable deposition process like CVD. Through the course of collaboration on this research it has already been established that mixed-phase BFO films can be grown on LAO substrates via CVD. The next step would be to grow BFO on thick (relaxed) single crystal LAO films deposited on silicon substrates. It has already been established that 001 oriented LAO films can be grown via MBE on silicon substrates by growing a thin STO buffer layer in between.[132] It would be a worthwhile effort to attempt the growth of mixed phase BFO films in a BFO/LAO/STO/Si heterostructure architecture using scalable methods. One potential complication, or perhaps interesting intersection of research, is that a 2-dimensional electron gas (2DEG) forms at the interface between LAO and STO crystalline layers.[133-136] It is interesting to note that it has also been demonstrated that the resultant 2DEG can be tailored by epitaxially straining the STO layer.[137]

7.2 Tensile Strain and the Orthorhombic Phase

As can be seen in the strain phase diagram calculated for BFO in **Figure 28**, the calculations suggest there is a rhombohedral-orthorhombic phase boundary on the tensile strain side of the diagram. Preliminary research by collaborators on this work has already begun with films grown epitaxially on $NdGaO_3$ and PrScO3, which impose a 1.26% and 1.5% tensile strain on BFO, respectively.[138,139] The results so far are inconclusive and one reason may be that the imposed strains are not large enough to reach the phase boundary on the tensile strain side of the phase diagram at room temperature. These substrates were chosen based on the phase field model shown in **Figure 28**. However, as stated earlier, recent preliminary refinements to the thermodynamic calculations that produced this figure have been conducted using more recently derived elastic constants, new electrostrictive coefficients derived from the *c/a* ratio and polarization measurements from the experimental data in this work, and a 6th order potential.[140,141] The new potential shows the phase boundary on the tensile side to be much farther to the right and thus will require much higher strains at reasonable temperatures. There are few known oxide substrates with large enough in-plane lattice parameters to attain these kinds of strains. PMN-PT is one notable exception with a rather large in-plane lattice parameter that depends on the specific stoichiometry of the material.[7] If commercial-grade PMN-PT substrates with high orientation tolerances can be obtained, perhaps mixed phase rhombohedral-orthorhombic or purely orthorhombic thin films can be grown and their properties measured for comparison to compressively strained BFO films.

7.3 The Coherent Phase Boundary

One of the most intriguing results of this investigation is the seemingly defect-free phase boundary between the T-phase and R-phase in mixed phase films. No dislocations appear in the HAADF images obtained for the phase boundaries and the ease of the crystallographic domain wall movement under mechanical and electrical perturbation supports the hypothesis of a defect free and coherent phase boundary. Although PZT has similarly been shown to exhibit coherent 2-phase polydomain heterostructures at compositions at or near the MPB, the tetragonal phase in PZT has a much smaller *c/a* ratio than BFO and the difference in out-of-plane lattice parameters between the tetragonal and rhombohedral (or monoclinic) phases is relatively small compared to that of BFO.[142] It is interesting to point out that in PZT the *c/a* ratio of the tetragonal phase diminishes with decreasing Ti content as the composition gets closer to the MPB, which in turn decreases the domain wall energy between different orientations (*c* and *a*) of the tetragonal phase as well as between the tetragonal phase and the rhombohedral or monoclinic phases.[143] In BFO, we see only a slight reduction in the *c/a* ratio for the T-phase as we approach the strain induced MPB from the T-phase side (see **Figure 12**) and with such a high *c/a* ratio it is not energetically favorable to form *a*-oriented T-phase domains as in PZT.

An open question that remains is what are the potential contributing factors allowing BFO to form these coherent yet highly strained phase boundaries? One possibility is that the elastic compliances of BFO increase dramatically near the phase boundary. It has been demonstrated that in PZT there is a softening of the dynamic Young's modulus associated with the phase transition between the tetragonal phase and the monoclinic phase.[144,145] The peak in the elastic compliance is at a composition in the middle of the MPB and is associated with the transverse instability of the polarization. It is conceivable that BFO exhibits similar behavior.

Another contributing factor may simply be the extreme flattening of the energy surface between the T-phase and the R-phase, allowing the energy of the coherent domain walls to be smaller than the energy required for dislocation formation. The existence of multiple, nearly-degenerate monoclinic phases in the vicinity of the MPB would contribute to this as slightly higher energy bridging phases between the T-phase and R-phase. It has already been suggested in recent reports that the structural transition across the MPBs is likely more complex than the simple coexistence between the T-phase and the R-phase, and that there may be multiple intermediate-bridging phases with monoclinic symmetry.[146,147] Multiple bridging phases could contribute to the flattening of the energy surface between the T-phase and the R-phase and allow for low-energy coherent phase boundaries between the two relative to the energy requirements for the formation of dislocations. More detailed unit cell by unit cell examination of the boundaries between the T-phase and R-phase via STEM and HAADF imaging could shed light on the phase evolution between the two. Careful CBED analysis along the phase boundary in a thickness series of mixed phase films would definitively determine the symmetry evolution between the phases and compliment the theoretical work already

done. Similar work has already been done on PZT for a series of compositions through the MPB in that material.[148]

A third potential contributing factor in the accommodation of high strains across the phase boundary is the tilts and rotations of the oxygen octahedra. The DFT results discussed in Section 4.3.6.1 suggest that the oxygen octahedra tilt about different crystallographic directions in the T-phase and R-phase (the [110] and [111] directions, respectively), which implies a rotational or tilt transition along the phase boundary.[118] This is corroborated somewhat in the electron diffraction patterns shown in **Figure 21** whereby superlattice reflections appear in the pattern for the T-phase but not in that of the R-phase from the same zone axis, which may be evidence for antiphase octahedral tilting along different directions for the two phases. More patterns from different zone axes are required to definitively determine this. The comprehensive simulation of all the distinct tilt systems for oxygen octahedra in perovskite oxides allows for experimental researchers to determine the tilt system of a given sample by obtaining selected area diffraction patterns from the 111 zone axis and the three surrounding 110, 101 and 011 zone axes.[149] This could be done for the mixed phase BFO films, although the constraints on sample preparation for TEM may complicate these kinds of studies due to the highly strained nature of the films and their tendency to curl up when thinned to electron transparency in plan-view.

7.4 Closing remarks

There are many new avenues for rewarding research involving interesting science and challenging engineering that stem from the work detailed in this report. The above discussion and suggestions for future work are only a small subset of the potential areas of focus. It is the author's hope that this work will serve as an important source of information for future graduate students and researchers specifically interested in exploring the use of BFO thin films as a practical lead-free piezoelectric material, as well as those generally interested in a better understanding of morphotropic phase boundaries in complex oxides and their associated material properties and behavior.

References

[1] T. Abraham, *et al.*, *Piezoelectric Ceramic and Ceramic/polymer composite Devices -*
[2] S.-E. Park, *et al.*, J. Appl. Phys. **82**, 1804 (1997).
[3] EU-Directive 2002/95/EC on the restriction of the use of certain hazardous substances in electrical and electronic equipment, Off. J. Eur. Union **L37**, 19 (2003).
[4] EU-Directive 2002/96/EC on waste electrical and electronic equipment (WEEE), Off. J. Eur. Union **L37,** 24 (2003).
[5] California Health and Safety Code Section 25214.9-25214.10.2.
[6] J. Rödel, *et al.*, J. Eur. Ceram. Soc. **29**, 1549 (2009).
[7] D. B. Schlom, *et al.*, Annu. Rev. Mater. Res. **37**, 589 (2007).
[8] M. D. Maeder, *et al.*, J. Electroceram. **13**, 385 (2004).
[9] T. R. Shrout, *et al.*, J. Electroceram. **19**, 113 (2007).
[10] T. Takenaka, *et al.*, Jpn. J. Appl. Phys. **47**, 3787 (2008).
[11] M. E. Lines, *et al.*, *Principles and Applications of Ferroelectrics and Related Materials*, (Oxford University Press: Oxford, 1977).
[12] T. Ikeda, Fundamentals of Piezoelectricity, (Oxford University Press: New York, NY, 1990).
[13] J. F. Nye, *Physical Properties of Crystals: Their Representation by Tensors and Matrices*, (Oxford University Press: Oxford, 1985).
[14] B. Jaffe, *et al.*, *Piezoelectric Ceramics*, (Academic Press: London, 1971).
[15] B. Noheda, *et al.*, Appl. Phys. Lett. **74**, 2059 (1999).
[16] R. Guo, *et al.*, Phys. Rev. Lett. **84**, 5423 (2000).
[17] H. Fu, *et al.*, Nature **403**, 281 (2000).
[18] D. E. Cox, *et al.*, Appl. Phys. Lett. **79**, 400 (2001).
[19] B. Noheda, Curr. Opin. Solid State Mater. Sci. **6**, 27 (2002).
[20] R. E. Cohen, *et al.*, Nature **441**, 941 (2006).
[21] J. Frantti, *et al.*, J. Phys.: Condens. Matter **20**, 472203 (2008).
[22] Y. M. Jin, *et al.*, J. Appl. Phys. **94**, 3629 (2003).
[23] Y. M. Jin, *et al.*, Phys. Rev. Lett **91**, 197601 (2003).
[24] Y. U. Wang, Phys. Rev. B **74**, 104109 (2006).
[25] Y. U. Wang, Phys. Rev. B **76**, 024108 (2007).
[26] M. Davis, *et al.*, J. Appl. Phys. **101**, 054112 (2007).
[27] S.-E. Park, *et al.*, J. Appl. Phys. **86**, 2746 (1999).
[28] D. Damjanovic, *et al.*, Appl. Phys. Lett. **80**, 652 (2002).
[29] S. E. Cummings, *et al.*, J. Appl. Phys. **39**, 2268 (1968).
[30] A. Fouskova, *et al.*, J. Appl. Phys. **41**, 2834 (1970).
[31] A. Shrinagar, *et al.*, Acta Cryst. A **64**, 368 (2008).
[32] K. Carl, *et al.*, Phys. Status Solidi **8**, 87 (1971).
[33] R. E. Newnham, *Properties of Materials: Anisotropy, Symmetry, Structure*, (Oxford University Press, Oxford, 2005).
[34] M. Budimir, *et al.*, J. Appl. Phys. **94**, 6753 (2003).
[35] Z. Wu, *et al.*, Phys. Rev. Lett. **95**, 037601 (2005).
[36] Y. Ishibashi, *et al.*, Jpn. J. Appl. Phys. 1 **38,** 800 (1999).

[37] H. Fu, *et al*., Nature **403,** 281 (2000).
[38] D. Damjanovic, J. Am. Ceram. Soc. **88,** 2663 (2005).
[39] M. Iwata, *et al*., Jpn. J. Appl. Phys. 1 **44,** 3095 (2005).
[40] M. Budimir, *et al*., Phys. Rev. B **73,** 174106 (2006).
[41] Z. Wu, *et al*., Phys. Rev. Lett. **95**, 037601 (2005).
[42] P. Ganesh, *et al*., J. Phys.: Condens. Matter **21**, 064225 (2009).
[43] M. Ahart, *et al*., Nature **451**, 545 (2008).
[44] N. A Pertsev, *et al*., Phys. Rev. B **67**, 054107 (2003).
[45] T. Matsunaga, *et al*., Phys. Rev. B **66,** 064102 (2002).
[46] S. H. Oh, *et al*., Phys. Rev. B **63,** 132101 (2001).
[47] S. H. Oh, *et al*., Phys. Rev. B **62,** 14757 (2000).
[48] Y. L. Li, *et al*., Appl. Phys. Lett. **83**, 1608 (2003).
[49] Shannon, R., Acta Cryst. A **32** , 751 (1976).
[50] W. Zhong, *et al*., Phys. Rev. Lett. **74**, 2587 (1995).
[51] D. J. Singh, *et al*., J. Phys. IV France **128**, 47 (2005).
[52] R. E. Cohen, Nature **358**, 136 (1992).
[53] A. Saddique, *et al*., Vet Hum Toxicol. **25,** 16 (1983).
[54] J. P. Mulkey, *et al*., Vet. Hum. Toxicol. **35**, 445 (1993).
[55] R. D. Brown, ''Bismuth'', Minerals Yearbook, Vol. I, Metals & Minerals (Interior Dept., Geological Survey, Washington, DC 20401), accessed September 7, 2011. http://minerals.usgs.gov/minerals/pubs/commodity/bismuth/110496.pdf
[56] V. Rodilla, *et al*., Chem. Biol. Interact. **115**, 71 (1998).
[57] Y. Sano, *et al*., J. Occup. Health **47**, 293 (2005).
[58] J. Rodel *et al*., J. Amer. Ceram. Soc. **92**, 1153 (2009).
[59] R. E. Eitel, *et al*., Jpn. J. Appl. Phys., Part 1 **40**, 5999 (2001).
[60] C. A. Randall, *et al*., J. Appl. Phys. **95**, 3633 (2004).
[61] M. R. Suchomel, *et al*., J. Appl. Phys. **96**, 4405 (2004).
[62] I. Grinberg *et al*., J. Appl. Phys., **98**, 094111 (2005).
[63] C. Michel, *et al*., Solid State Commun. **7**, 701 (1969).
[64] J. M. Moreau, *et al*., J. Phys. Chem. Solids **32**, 1315 (1971).
[65] F. Kubel, *et al*., Acta Cryst. B **46**, 698 (1990).
[66] F. Zavaliche, *et al*., Phase Transit. **79**, 991 (2006).
[67] J. R. Teague, *et al*., Solid. State. Commun. **8**, 1073 (1970).
[68] J. Wang, *et al*., Science **299**, 1719 (2003).
[69] J. Li, *et al*., Appl. Phys. Lett. **84**, 5261 (2004).
[70] F. Bai, *et al*., Appl. Phys. Lett. **86**, 032511 (2005).
[71] J. B. Neaton, *et al*., Phys. Rev. B **71**, 014113 (2005).
[72] G. Xu, *et al*., Appl. Phys. Lett. **86**, 182905 (2005).
[73] S. Y. Yang, *et al*., Appl. Phys. Lett. **87**, 102903 (2005).
[74] Y.-H. Chu, *et al*., Adv. Mater. **19**, 2662 (2007).
[75] C. Ederer, *et al*., Phys. Rev. Lett. **95**, 257601 (2005).
[76] D. Ricinschi, *et al*., J. Phys.: Condens. Matter **18**, L97 (2006).
[77] P. Ravindran, *et al*., Phys. Rev. B **74**, 224412 (2006).
[78] R. V. Shpanchenko, *et al*., Chem. Mater. **16**, 3267 (2004).

[79] A. A. Belik, *et al*., Chem. Mater. **17**, 269 (2005).
[80] A. A. Belik, *et al*., Chem. Mater. **18**, 798 (2006).
[81] R. Wojciechowski, *et al*., Phys. Rev. B **67**, 224107 (2003).
[82] P. Baettig, *et al*., Chem. Mater. **17**, 1376 (2005).
[83] D. L. Smith, *Thin-Film Deposition Principles and Practice*, (McGraw Hill: Boston, MA, 1995).
[84] M. Ohring, *Materials Science of Thin Films*, (Academic Press: San Diego, CA, 2002).
[85] M. A. Herman, *et al*., *Epitaxy Physical Principles and Technical Implementation*, (Springer: Berlin, 2004).
[86] D. B. Chrisey, *et al*., *Pulsed Laser Deposition of Thin Films*, (John Wiley & Sons, Inc.: New York, NY, 1994).
[87] J. S. Horwitz, *et al*., J. Electroceram. **4**, 357 (2000).
[88] A.K. Pradhan, *et al*., Appl. Phys. Lett. **81**, 3597 (2002).
[89] F.A. Miranda, *et al*., J. Am. Ceram. Soc. **91**, 1864 (2008).
[90] M. Veis, *et al*., J. Phys. D: Appl. Phys. **42**, 195002 (2009).
[91] B. E. Warren, *X-Ray Diffraction*, (Dover Publications: New York, NY, 1990).
[92] A. Guinier, *X-Ray Diffraction in Crystals, Imperfect Crystals and Amorphous Bodies*, (Dover Publications: New York, NY, 1994).
[93] B. D. Cullity, *Elements of X-Ray Diffraction*, (Addison-Wesley: Reading, MA, 2001).
[94] H. Kiessig, Ann. Physik **10**, 769 (1931).
[95] J. P. Sauro, *et al*., Phys. Rev. **143**, 439 (1966).
[96] P. Batson, *et al*., Nature **418**, 617 (2002).
[97] L. Reimer, *Transmission Electron Microscopy: Physics of Image Formation and Microanalysis*, (Springer: Berlin, 1993).
[98] D. B. Williams, *et al*., *Transmission Electron Microscopy*, (Plenum Press: New York, NY, 1996).
[99] B. Fultz, *et al*, *Transmission Electron Microscopy and Diffractometry of Materials*, (Springer: Berlin, 2002).
[100] R. Erni, *et al*., Phys. Rev. Lett. **102**, 096101 (2009).
[101] A. Kirilyuk, J. Phys. D **35**, R189 (2002).
[102] M. Fiebig, *et al*., J. Opt. Soc. Am. B **22**, 96 (2005).
[103] A. Kumar, *et al*., Appl. Phys. Lett., **92**, 231915 (2008).
[104] B. Dick, *et al*., Appl. Phys. B: Photophys. Laser Chem. **38**, 107 (1985).
[105] S. A. Denov, *et al*., J. Am. Ceram. Soc. **94**, 2699 (2011).
[106] These results were corroborated experimentally by Bea, *et al*.,[107] in experimental work reported on during the same period as the preliminary work in this report.[111]
[107] H. Béa *et al*., Phys. Rev. Lett. **102**, 217603 (2009).
[108] S. H. Oh, *et al*., Phys. Rev. B **63**, 132101 (2001).
[109] M. B. Kelman, *et al*., Appl. Phys. Lett. **80**, 1258 (2002).
[110] S. Yokoyama, *et al*., J. Mater. Res. **22**, 1551 (2007).
[111] R. J. Zeches, *et al*., Science **326**, 977 (2009).
[112] C. H. Kim, *et al*., Physica B **262**, 438 (1999).
[113] A. Kumar, *et al*., Appl. Phys. Lett. **97**, 112903 (2010).
[114] J. X. Zhang, *et al*., Nat. Nanotechnol. **6**, 98 (2011).

[115] G. Kresse, *et al*., Phys. Rev. B **54**, 11169 (1996).
[116] V. I. Anisimov, *et al*., J. Phys. Condens. Matter **9**, 767 (1997).
[117] A. G. Christy, Acta Crystallogr. B **51**, 753 (1995).
[118] A. J. Hatt, *et al*., Phys. Rev. B **81**, 054109 (2010).
[119] N. A. Pertsev, *et al*., *Phys. Rev. Lett*. **80**, 1988 (1998).
[120] L. Q. Chen, *Annu. Rev. Mater. Res*. **32**, 113 (2002).
[121] Y. L. Li, *et al*., *Acta Mater*. **50**, 395 (2002).
[122] J. X. Zhang, *et al*., Appl. Phys. Lett. **95**, 122904 (2009).
[123] S. L. Shang, *et al*., Phys. Rev. B **80**, 052102 (2009).
[124] G. Sheng, J. X. Zhang and L. Q. Chen, private communications (unpublished).
[125] P. M. Raccah, *et al*., J. Appl. Phys. **39**, 1209 (1968).
[126] J. T. Cheung, *et al*., Appl. Phys. Lett. **62**, 2045 (1993).
[127] S. Madhukar, *et al*., J. Appl. Phys. **81**, 3543 (1997).
[128] K. Rabe, *et al*., *Physics of Ferroelectrics: A Modern Perspective* (Springer Press: New York, NY, 2007).
[129] C. Durkan, *et al.,* Phys. Rev. B **60**, 16198 (1999).
[130] C. M. Foster, J. Appl. Phys. **81**, 2349 (1997).
[131] V. R. Palkar, *et al*., Appl. Phys. Lett. **80**, 1628 (2002).
[132] Y. Y. Mi, *et al*., Appl. Phys. Lett. **90**, 181925 (2007).
[133] A. Ohtomo, *et al*., Nature **419**, 378 (2002).
[134] A. Ohtomo, *et al*., Nature **427,** 423 (2004).
[135] C. Cen, *et al*., Science **323**, 1026 (2009).
[136] J. W. Park, *et al*., Nat. Commun. **1**, 94 (2010).
[137] C. W. Bark, *et al*., Proc. Natl. Acad. Sci USA **108**, 4720 (2011).
[138] Y.-H. Chu, private communications.
[139] D. G. Schlom, private communications.
[140] S. L. Shang, *et al*., Phys. Rev. B **80**, 052102 (2009).
[141] G. Sheng, J. X. Zhang and L. Q. Chen, private communications (unpublished).
[142] W.-F. Rao, *et al*., Appl. Phys. Lett **91**, 052901 (2007).
[143] K. A. Schönau, *et al*., Phys. Rev. B **75**, 184117 (2007).
[144] A. Bouzid, *et al*., J. Eur. Ceram. Soc. **25**, 3213 (2005).
[145] F. Cordero, *et al*., Phys. Rev. Lett. **98**, 255701 (2007).
[146] H. M. Christen, Phys. Rev. B **83**, 144107 (2011).
[147] Z. Chen, *et al*., Adv. Funct. Mater. **21**, 133 (2011).
[148] Schierholz, *et al*., Phys. Rev. B **84**, 064122 (2011).
[149] D. I. Woodward, *et al*., Acta Cryst. B **61**, 387 (2005).